Laboratory Investigation of the Sealing Properties of the Lea Park Shale with Respect to Carbon Dioxide

A Thesis

Submitted to the College of Graduate Studies and Research

In Partial Fulfillment of the Requirements

for the

Degree of Master of Science

in the

Department of Civil and Geological Engineering

University of Saskatchewan

Saskatoon

by

Allison Larsen

PERMISSION TO USE

The author has agreed that the library, University of Saskatchewan, may make this thesis freely available for inspection. Moreover, the author has agreed that permission for extensive copying of this thesis for scholarly purposes may be granted by the professors who supervised the thesis work recorded herein or, in their absence, by the head of the Department or the Dean of the College in which the thesis work was done. It is understood that due recognition will be given to the author of this thesis and to the University of Saskatchewan in any use of the material in this thesis. Copying or publication or any other use of the thesis for financial gain without approval by the University of Saskatchewan and the author's written permission is prohibited.

Requests for permission to copy or to make any other use of material in this thesis in whole or in part should be addressed to:

Head of the Department of Civil and Geological Engineering

University of Saskatchewan

Engineering Building

57 Campus Drive

Saskatoon, Saskatchewan, Canada

S7N 5A9

Allison Larsen

January 1, 2010

ABSTRACT

The Intergovernmental Panel on Climate Change (2001) reports that increased anthropogenic greenhouse gas (GHG) emissions, of which carbon dioxide (CO_2) is the main component, have caused the Earth's temperature to rise. Therefore, it is necessary to find ways to reduce GHG emissions and to deal with the emissions that continue to be produced. Carbon capture and storage (CCS) is one method that is being considered to deal with GHG emissions, specifically CO_2 emissions. The basic idea behind CCS is that CO_2 is captured from a point source, such as a power plant, and is then transported to a storage site (e.g., an oil or gas reservoir), where it is subsequently stored.

The International Energy Agency Greenhouse Gas Programme (IEA GHG) began a CO_2 geological sequestration pilot project in 2000 in Weyburn, Saskatchewan as part of an enhanced oil recovery project operatedby Cenovus (formerly EnCana) in the Weyburn Field (White et al. 2004). The research presented in this thesis evaluates the sealing potential of the Lea Park Formation in the Weyburn Field by determining its permeability and CO_2 breakthrough pressure. In this context, breakthrough pressure describes the differential pressure between a wetting phase (e.g., formation brine) and a non-wetting phase (e.g., CO_2) that is sufficient to enable the non-wetting phase to form a connected flow system across a given volume of porous medium (e.g., a rock sample).

A new system for measuring the permeability and CO_2 breakthrough pressure of shales was developed in this research. The development effort included extensive trouble-shooting and, ultimately, the development of sample preparation and testing procedures. The new system was used to conduct permeability and CO_2 breakthrough pressure tests on shale samples from the Lea Park Formation (i.e., "Lea Park shale") and the Colorado Group (i.e., "Colorado shale"). Permeability results for samples from the Lea Park shale ranged from 14 to 35 nd ($14 \cdot 10^{-21}$ to $35 \cdot 10^{-21}$ m^2), and between eight and 46 nd ($8 \cdot 10^{-21}$ to $46 \cdot 10^{-21}$ m^2) for the Colorado shale. A CO_2 breakthrough pressure for the Lea Park shale was

determined to be 0.02 MPa, while values of 0.02 and 2.7 MPa were measured for the Colorado shale.

The CO_2 breakthrough pressure test results indicate that the Lea Park shale will not withstand large pressures before allowing CO_2 to flow through it. However, the permeabilities are extremely low; hence the rate of flow would be low. In other words, the low permeability of the Lea Park shale will be the controlling factor in terms of the rate of potential CO_2 leakage through it. Calculations based on the properties measured in this research suggest that the time required for CO_2 to flow from the base to the top of the Lea Park Formation would be on the order of ten thousand years. Based on diffusion coefficients published for other shales, calculations suggest that CO_2 leakage via chemical diffusion would be several times slower leakage via hydraulically-driven flow.

ACKNOWLEDGEMENTS

I would like to thank my supervisor, Dr. Chris Hawkes, for always being available and supportive throughout this process.

I would like to thank Zig Szczepanik and Frank Monsman for all of their help in the Rock Mechanics Lab.

I would like to thank my committee members, Dr. Doug Milne, Dr. Jit Sharma, and Dr. Lisa Feldman, for their time and guidance.

I would like to thank the Department of Civil and Geological Engineering for the scholarship that I received during the first two years of my program.

This study was funded in part by the IEA GHG Weyburn-Midale CO_2 Monitoring and Storage Project, via the Petroleum Technology Research Centre, and the Natural Science and Engineering Research Council of Canada.

TABLE OF CONTENTS

LIST OF VARIABLES AND ABBREVIATIONS

VARIABLES:

A – cross-sectional area

a – slope of ln(ΔP) vs. time graph

A, B – Skempton pore water pressure coefficients

C_b – bulk compressibility of porous medium

C_{fl} – pore fluid compressibility

d – effective pore diameter

d_{crit} – critical pore diameter

D – chemical diffusion coefficient

D_h – hydraulic diffusion coefficient

E_d – dynamic Young's modulus

E_s – static Young's modulus

g – gravitational acceleration

k – permeability

L – length

M – parameter related to compressive storage of a porous medium;
$= \{nC_{fl} + [\alpha(1+n) - n]C_b\}^{-1}$

n – porosity

P_0 – compressional wave zero time

P_c – confining pressure

P_{cap} – capillary pressure

P_n – pressure in non-wetting phase

P – pore pressure

P_w – pressure in wetting phase

Q – flow rate

r – effective pore radius

R_1 – upstream reservoir

R_2 – downstream reservoir

S_0 – shear wave zero time

S_d – compressive storage of downstream reservoir

S_u – compressive storage of upstream reservoir

t – time

t_{90} – time required for transient flow rate to approach (i.e., to be within 90% of) the steady-state flow rate

t_{outlet} – time required for a fluid phase or component reach the top of a laterally infinite aquitard under transient diffusion (or flow) conditions

t_p – compressional wave arrival time

$t_{p,corr}$ – corrected compressional wave arrival time

t_s – shear wave arrival time

$t_{s,corr}$ – corrected shear wave arrival time

V_1 – volume of upstream reservoir

V_2 – volume of downstream reservoir

V_p – compressional wave velocity

V_p – pore volume

V_s – shear wave velocity

l – thickness of laterally infinite layer through which diffusion (or flow) is occurring

z – depth

ρ – density

ρ_b – bulk density

μ - fluid viscosity

α – Biot's coefficient

ΔP – pressure increment

ΔP_1 – pressure increment in reservoir 1 at time 0

$\Delta\sigma_1$ – change in total major principal stress

$\Delta\sigma_3$ – change in total minor principal stress

θ – contact angle of the fluid interface where it meets the pore surface

υ_d – dynamic Poisson's ratio

σ – interfacial tension

σ_v – vertical stress

ABBREVIATIONS:

BTP – breakthrough pressure

CCS – carbon capture and storage

CO_2 – carbon dioxide

EOR – enhanced oil recovery

GHG – greenhouse gas

IEA GHG – International Energy Agency Greenhouse Gas Programme

IFT – interfacial tension

Panel – GCTS HPCP-70 Pressure Control Panel

PTRC – Petroleum Technology Research Centre

SEM – scanning electron microscope analysis

Syringe pumps – Teledyne-Isco 260D syringe pumps

Triaxial – GCTS RTX-1000 Servo-Controlled Triaxial Rock Testing System

UPS – uninterruptible power supply

XRD – x-ray diffraction

NON-SI UNITS USED IN THIS WORK:

nd – nanodarcy, a measure of permeability (~10^{-21} m^2)

md – millidarcy, a measure of permeability (~10^{-15} m^2)

Mt – megatonne, a measure of mass (= 10^9 kg)

1. INTRODUCTION

1.1 Background

The Intergovernmental Panel on Climate Change (2001) reports that increased anthropogenic greenhouse gas (GHG) emissions, of which carbon dioxide (CO_2) is the main component, have caused the Earth's temperature to rise. This increase in GHG emissions is mainly due to the use of fossil fuels, which play a crucial role in bringing power to both developed and developing countries (Bachu and Stewart 2002; Dones et al. 2008). It is believed that the time required to transition from today's dependence on fossil fuels to alternative energy sources will be at least many decades, if not longer (Hepple and Benson 2005; Dones et al. 2008). As such, it is necessary to find ways to reduce GHG emissions and to deal with the emissions that continue to be produced.

Carbon capture and storage (CCS) is one method that is being considered to deal with GHG emissions, specifically CO_2 emissions. The basic idea behind CCS is that CO_2 is captured from a point source, such as a power plant, and is then transported to a site where it is subsequently stored.

There are three basic types of storage: deep in the ocean, in terrestrial biomass, and in geological formations (Hepple and Benson 2005). Sequestration (i.e., storage in geological formations) includes storing the CO_2 in depleted or depleting oil and gas reservoirs, in saline aquifers, or within unmineable coal seams (Holloway 2001; Bachu and Stewart 2002; Ennis-King and Paterson 2002; Hepple and Benson 2005).

Technology associated with sequestration is the most well-understood of the various options. Saline aquifers are believed to have the largest potential for storage. However, economically, this type of storage is not presently feasible (Li et al. 2005a and 2005b).

Sequestration within oil and gas reservoirs is the most attractive option at present. These reservoirs have been extensively studied and the geological and physical properties associated with them have been characterized, making them ideal candidates for CO_2 storage (Benson and Cook 2005). Also, much of the infrastructure necessary to inject and store CO_2 is already in place (Li et al. 2005a and 2005b). It is believed that these reservoirs have the potential to store 40% of the CO_2 that needs to be removed from the atmosphere (Flin 2004).

CCS associated with depleting oil reservoirs can be used in conjunction with enhanced oil recovery (EOR). In this case, CO_2 is injected into the depleting oil reservoir which, in turn, increases the oil recovery. The profits generated from the additional oil production can be used to offset the costs associated with CCS (Bossie-Codreanu 2008).

1.2 Aquitards and Caprocks

Aquitards overlie aquifers and serve as seals which prevent the upward migration of fluid from the aquifer into overlying layers. Caprocks overlie hydrocarbon reservoirs and generally serve the same purpose as aquitards. Caprocks (like aquitards) are generally shales, mudstones, siltstones, evaporites, or fine-grained carbonates that have low permeabilities (Zweigel et al. 2005). In the context of fluids such as hydrocarbons and CO_2, which are generally regarded as non-wetting fluids in most rocks, another term used to refer to the fine-grained rock immediately overlying a reservoir or aquifer is primary seal; the term seal often, either explicitly or implicitly, being used to imply that capillary forces act to prevent the penetration of non-wetting fluids into these fine-grained rocks (see Section 1.2.1 for further discussion on this topic). In the case of the IEA GHG Weyburn-Midale Project (to be presented in the following section), the caprock (i.e., primary seal) is an anhydrite, whose properties have been investigated previously (Li et al. 2005a and 2005b). The Lea Park Formation, which is the primary focus of the research presented in this thesis, is an aquitard which serves as a secondary seal.

When considering a location for long-term CO_2 storage, one of the main considerations is to minimize the risk to humans and the environment. Therefore, in order for long-term CO_2 storage to be feasible, it must be shown that once injected, the CO_2 will not leak out of the aquifer or reservoir over the long term (Chiquet et al. 2007). As such, it is important to know if the caprock and/or aquitards that overlie the storage unit will allow leakage through them to overlying formations, and possibly into groundwater sources or to the surface, which could have significant impacts on humans and wildlife (Flin 2004; Bennion and Bachu 2007). For example, Flin (2004) warns that a large-scale release of CO_2 could lead to human and livestock deaths by suffocation. Holloway (2007) states that in most cases, CO_2 releases are not that hazardous but that they can be dangerous locally.

1.2.1 Sealing Capacity of Caprocks

Traditionally, a caprock's sealing ability has been regarded as stemming from its high capillary entry pressure, which is related to the size of the pore throats that connect the pores within the caprock (Holloway 2001). The capillary entry pressure acts to exclude hydrocarbons from its pore system and to ultimately stop the flow of hydrocarbons (AL-Bazali et al. 2005).

Capillary entry pressure may also prevent CO_2 from entering the brine-filled pores of a sealing formation, depending on its wettability with respect to CO_2. As the amount of CO_2 being injected into the reservoir increases, the pressure that the CO_2 exerts onto the caprock will also increase. As this pressure increases, the CO_2 will be able to invade smaller and smaller pores in the caprock and may eventually be able to flow through the caprock (Espie 2005). The pressure at which this occurs is known as the gas breakthrough pressure, which is the differential pressure across a pore network at which a non-wetting phase (such as CO_2) begins to displace a wetting phase (such as formation brine) and form a continuous Darcy flow system across that pore network (Hildenbrand et al. 2004; Li et al. 2005).

In terms of long-term CO_2 storage, there are several paths through which leakage may occur, hence a range of rates at which leakage through the caprock may occur. Potentially high leakage rates may be associated with leakage through well casings (e.g., Wells et al. 2007), along hydraulically-conductive discontinuities (e.g., Shipton et al. 2004) or by mechanical

failure of the caprock (e.g., Soltanzadeh and Hawkes 2008). Assuming that storage sites are selected, remediated (as required) and operated so as to mitigate the potential for leakage through such features, a key question is the leakage potential through intact caprock. In such a case, leakage can occur by overcoming the capillary entry pressure of the caprock, in which case leakage rate will be controlled by the permeability of the caprock, or by diffusion (Busch et al. 2008). As such, the gas breakthrough pressure and the permeability of the caprock are important parameters to characterize. Diffusion is also relevant; however, it will be shown later (using literature results) that diffusion-controlled leakage is generally slow compared to hydraulic-controlled leakage. Therefore, the focus in the experimental work presented in this thesis is on breakthrough pressure and permeability.

1.3 Weyburn-Midale Project

The International Energy Agency Greenhouse Gas Programme (IEA GHG) began as a CO_2 sequestration pilot project in 2000 in Weyburn, Saskatchewan (see Fig. 1.1), as part of an EOR operation at Cenovus' (formerly EnCana's) Weyburn field (White et al. 2004). The Weyburn field is located in the Williston Basin, which extends from southern Saskatchewan into the north-central United States, and covers approximately 170 km^2. Fractured carbonates of the Midale beds form the reservoir, which has a primary upper seal composed of anhydrite. The carbonate thins against a regional unconformity at the northern edge of the reservoir. The Watrous Formation, which is a thick sequence of fine-grained clastic sedimentary rocks, overlies this unconformity and provides a regional seal to any leakage that may occur from the reservoir (Preston et al. 2005). The Lea Park Formation, for which core samples were available for analysis in this research, sits within one of four secondary seals overlying the Watrous Formation. The final phase of the IEA GHG project encompasses both the Weyburn and Midale fields, which are located side-by-side, and have essentially the same geological attributes.

The CO_2 for the Weyburn and Midale fields is transported by pipeline from the Dakota Gasification Company in Beulah, North Dakota, about 325 km south of Weyburn. CO_2 injection operations in the Weyburn Field are expected to last for 20 to 25 years and to store

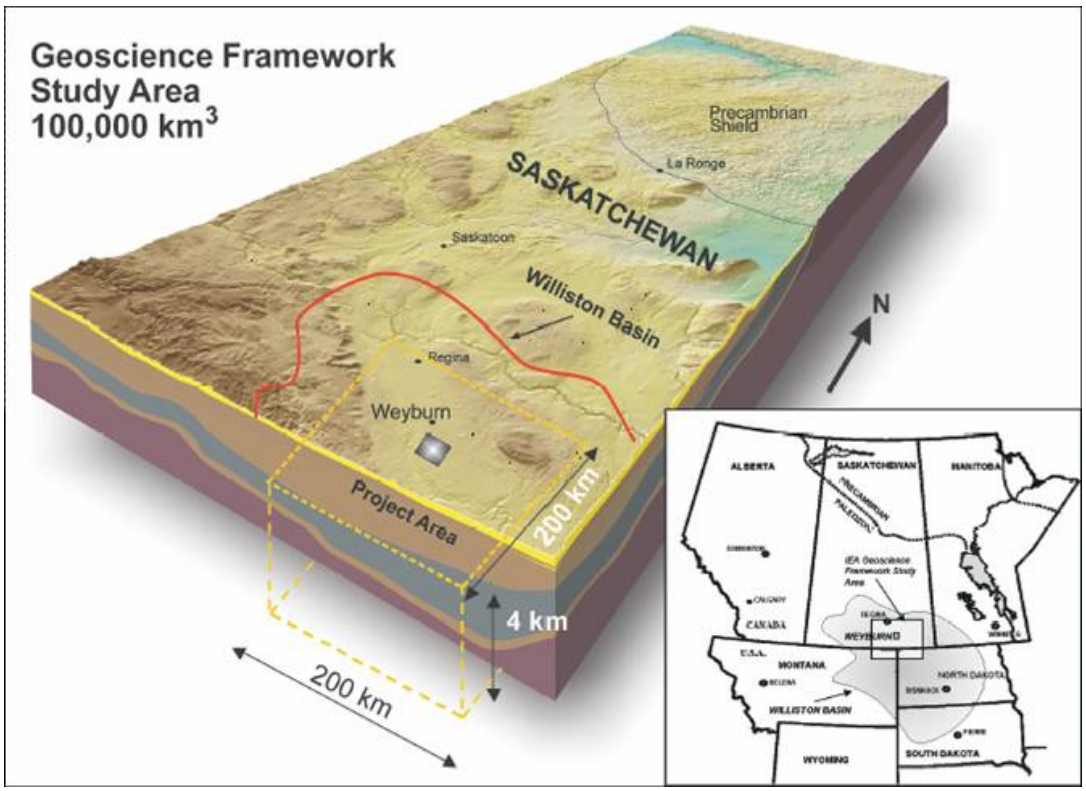

Fig. 1.1. Weyburn project area (source: http://www.ptrc.ca/weyburn_overview.php).

more than 30 million tonnes of CO_2 (Preston et al. 2005). Numbers for the Midale Field are currently not available, but they are expected to be smaller than Weyburn.

1.4 Objectives

The general objectives of this research are:

- To evaluate the sealing potential of the Lea Park Formation in the Weyburn Field.
- To assess, implement, and refine lab testing techniques for measuring the sealing properties of shales.

The specific objectives of this research are:

- To determine the permeability of shale samples from the Lea Park Formation.

- To determine the gas breakthrough pressure of shale samples from the Lea Park Formation.
- To analyze the results within the context provided by the shale characteristics determined from routine analyses (e.g., to compare the gas breakthrough pressure results with those of mercury porosimetry), and, if possible, to compare the Lea Park to other shales present in the Williston Basin and elsewhere.

1.5 Scope

Laboratory testing was performed on a fixed amount of Lea Park shale core from a Weyburn well provided by the Petroleum Technology Research Centre (PTRC) of Regina, Saskatchewan. The amount of core provided was approximately 1.0 m. The focus of this laboratory testing program was on determining permeability and gas breakthrough pressure using the core provided. Routine characterization of the core samples was done by others.

New Lea Park cores were not obtained during this testing program, and no field testing was conducted. All of the experiments were performed using an existing triaxial compression cell and syringe pumps available in the Rock Mechanics Laboratory; valves, tubing, temperature-control equipment were acquired as needed to implement permeability and breakthrough-pressure testing with the cell and pumps provided. Determination of the Lea Park pore brine composition had been conducted previously by another graduate student; these results were used for the experiments presented in this thesis.

Permeability and gas breakthrough pressure testing were also conducted on Colorado Group shale cores from the Rocanville area (eastern SK) provided by Potash Corporation of Saskatchewan. These cores became available during the course of this project, and were deemed relevant because they are from the same aquitard unit as the Lea Park (i.e., the Colorado Group aquitard), and from a site reasonably close to – and with near-equivalent stratigraphy to – the Weyburn Field. No geophysical logs were available for the borehole from which these cores were taken, and no additional logging or field testing was conducted as part of this research.

Laboratory investigation of diffusional processes were not considered in this work, nor were the geochemical effects of long-term CO_2 exposure on the properties of the Lea Park Formation and Colorado Group shales.

The study of leakage through wellbores and faults is being conducted by other researchers, and flows through such features were not considered in this work.

1.6 Organization of Thesis

Chapter 2 contains a review of relevant literature associated with this thesis. Chapter 3 describes the characterization of the Lea Park and Colorado shale samples, including routine analyses. Chapter 4 describes the experimental design and procedures that were used for permeability and breakthrough pressure testing in this research. Chapter 5 presents the results obtained from the tests described in Chapter 4. Chapter 6 provides a discussion of the results, and Chapter 7 presents conclusions and recommendations.

2. REVIEW OF MECHANISMS AND MEASUREMENT OF FLUID TRANSPORT IN LOW-PERMEABILITY ROCKS

In this chapter, fluid transport processes relevant to CO_2 containment are reviewed, with an emphasis on methods for measuring the properties that govern these processes. A review of literature presenting the results of permeability and breakthrough pressure measurements on fine-grained rocks is included in Chapter 6 of this thesis.

2.1 Permeability Measurement

According to Darcy's Law, the permeability of a porous medium governs the rate of fluid flow occurring in response to a given pressure gradient. As such, an assessment of potential CO_2 leakage rates through caprocks and aquitards requires the measurement of the permeabilities of these rocks. The traditional method of determining permeability in porous media – which involves injecting fluid at a constant flow rate or a constant pressure until steady-state conditions are reached – is impractical for most fine-grained samples (Narahara et al. 1988). To obtain a pressure differential across the sample, the flow rates must be very small and are difficult to measure accurately (Narahara et al. 1988). Also, the time required to reach equilibrium can be prohibitively long and the data is not always reliable (Brace et al. 1968; Haskett et al. 1988; Dicker and Smits 1988).

In order to determine the permeability of fine-grained rocks, such as shale, Brace et al. (1968) developed a pressure-pulse decay method. The basic premise behind the pressure-pulse decay method is to observe the decay of a small change in pressure, which is applied to one end of a sample, as it traverses across the sample (Brace et al. 1968). This method is applicable for determining effective permeability to gas in the presence of a

liquid, and for determining absolute permeability to liquid or gas in single-fluid-phase saturation scenarios (Dicker and Smits 1988).

A precisely ground, right-cylindrical sample with pore volume V_p is placed between two reservoirs, one upstream (R_1) and one downstream (R_2), with volumes V_1 and V_2, respectively (Brace et al. 1968) (see Fig. 2.1). R_1 and R_2 are simply functions of the testing equipment. The reservoir on each end of the sample consists of the porous plate that sits flush with the end of the sample, as well as the tubing, pressure transducer(s), and valve(s) that are connected to it. R_1 and R_2 are filled with the test fluid at some initial pressure. A confining pressure, P_c, is applied to the sample. This confining pressure must be greater than the pressures in R_1 and R_2 (Brace et al. 1968; Jones 1997).

At time $t=t_0$, the pressure in R_1 and R_2 are equal (Brace et al. 1968; Jones 1997). The pressure in R_1 is then increased by a small amount, ΔP_1. As the test fluid flows from R_1 into the sample, the pressure in R_1 decreases, and the pressure in R_2 eventually increases, after staying approximately constant initially (see Fig. 2.2).

To analyse the experimental results, for test set-ups in which the pore volume within the sample is small relative to the volumes of R_1 and R_2, the measured pressure difference between R_1 and R_2 is plotted versus time on semi-logarithmic paper (Brace et al. 1968; Dicker and Smits 1988) (Fig. 2.3).

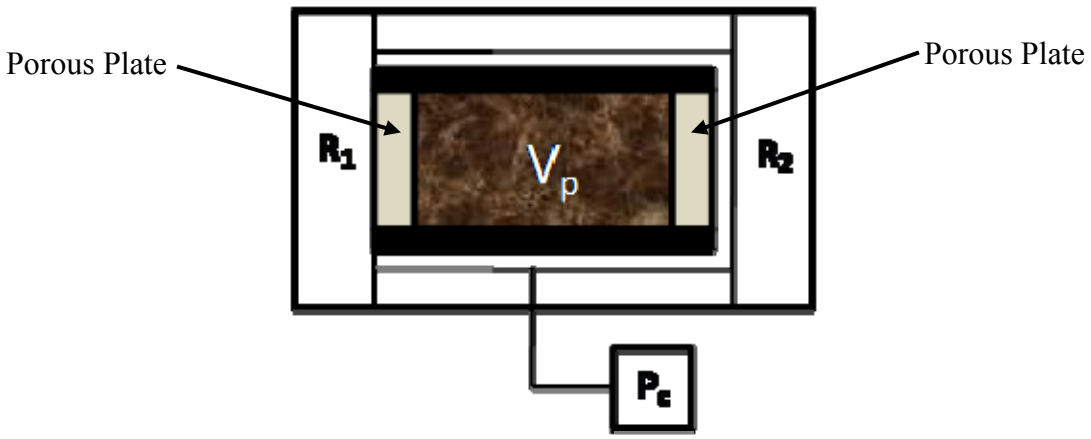

Fig. 2.1. Experimental apparatus for pressure-pulse decay permeability testing.

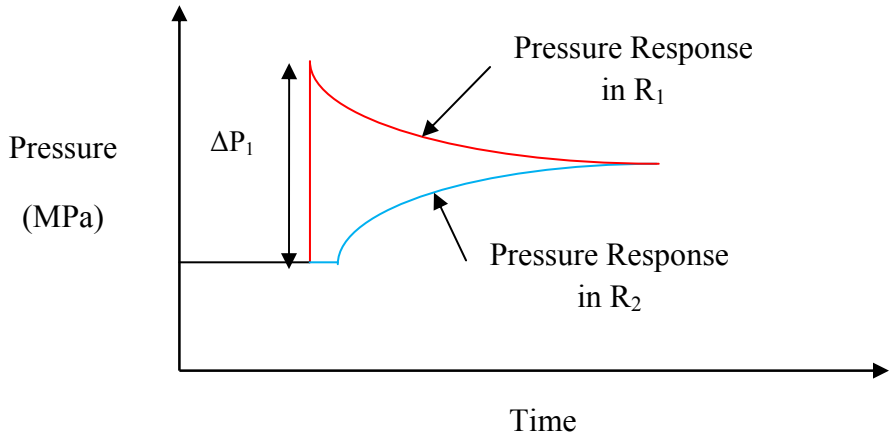

Fig. 2.2. Illustration of typical experimental results for a pressure-pulse decay permeability test.

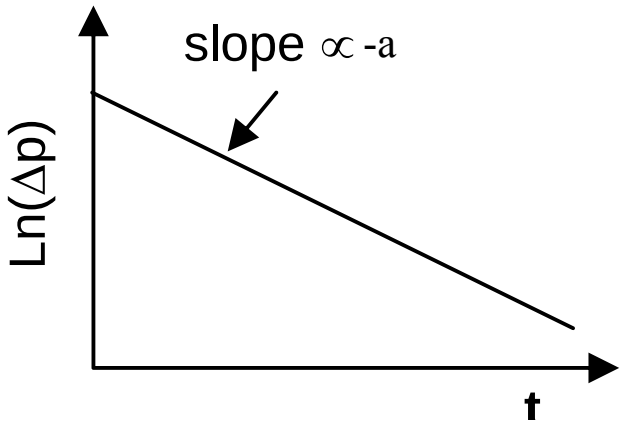

Fig. 2.3. Typical plot of permeability test results.

The slope of the straight-line portion of this graph is designated as a (s^{-1}). Permeability, k, is calculated from

$$k = \frac{-a\mu L S_u S_d}{A(S_u + S_d)} \tag{2.1}$$

where μ is the fluid viscosity [Pa·s], L is the length of the sample [m], S_u is compressive storage of the upstream reservoir [$m^3 \cdot Pa^{-1}$], S_d is the compressive storage of the downstream reservoir [$m^3 \cdot Pa^{-1}$], and A is the cross-sectional area of the sample [m^2].

Trimmer (1981) found that the error associated with using equation 2.1 was dependent only on the ratio of the effective sample pore volume and the reservoir volume (R_1 and R_2). If this ratio is greater than one (i.e., if the sample pore volume is greater than the reservoir volume), the semi-log plot is not linear and the slope of the plot is difficult to determine. However, if the ratio is less than 0.25, the error associated with using equation 2.1 is 10% or less.

Though conceptually simple, the pulse-decay permeability test is a difficult test to implement. For example, pressure change in the testing system is extremely sensitive to temperature change and small leaks (e.g., through valves or fittings).

2.2 Gas Breakthrough Pressure Measurement

As mentioned in Chapter 1, a traditional view on fluid containment beneath caprocks has emphasized capillary processes. More specifically, within a caprock, there is a system of small, wetting-phase-filled pores (i.e., brine-filled pores), and these pores can generate large capillary pressures that do not allow non-wetting phases, such as CO_2, to enter into the pores (AL-Bazali et al. 2005).

In Fig. 2.4, it can be seen that the pressure in the wetting phase, P_w, and the capillary pressure, P_{cap}, act against the pressure in the non-wetting phase, P_n. As long as the differential pressure between P_w and P_n is less than P_{cap}, the non-wetting phase will not be able to move into the caprock. However, if the differential pressure between P_w and P_n exceeds P_{cap} within a certain pore throat, the non-wetting phase will be able to advance along

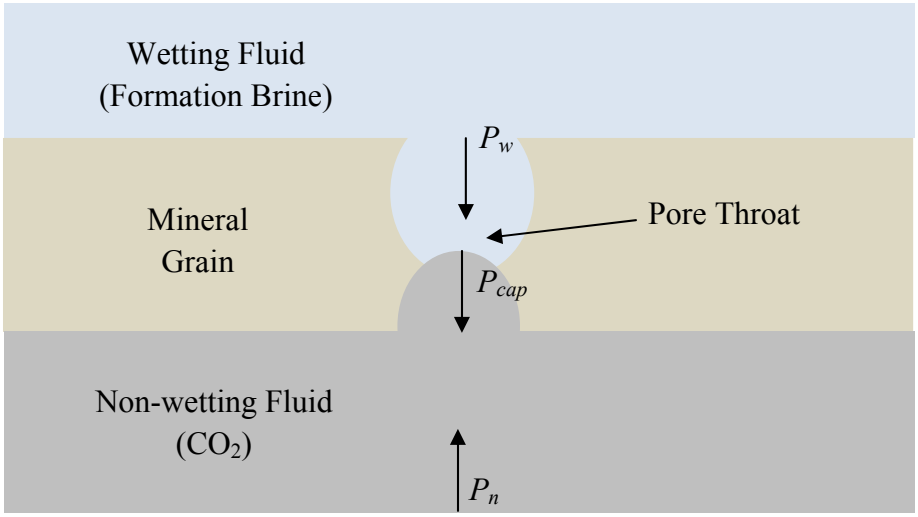

Fig. 2.4. Depiction of capillary sealing capacity in a pore throat of a rock.

that pore throat until it reaches a point where it narrows sufficiently to prevent further ingress (or, otherwise, until the pore body downstream of the throat is fully invaded (Li et al. 2005)). If the differential pressure between P_w and P_n exceeds P_{cap} at a sufficient number of pore throats to form a connected flow system from one side of a sample to the other, the non-wetting phase will be able to flow through the sample, at a rate governed by its effective permeability (Li et al. 2005a and 2005b). Once this flow is established, breakthrough has occurred. In practice, at such a pressure the caprock would no longer provide a perfect seal against leakage from the non-wetting fluid(s) in the underlying formation.

2.2.1 Experimental Setup

The basic idea behind determining gas breakthrough pressure is to force gas through one end of a brine-saturated sample until the gas reaches the other end of the sample. There are two ways of doing this: (i) approach the gas breakthrough pressure from below using small pressure increments (e.g., Li et al. 2005a and 2005b); or (ii) surpass the gas breakthrough pressure by applying an instantaneously high pressure gradient across the sample and waiting for the pressure difference to decay to some finite value (e.g., Hildenbrand et al.

2002; Hildenbrand et al. 2004). The latter method is conservative, in that it generally leads to a lower value of breakthrough pressure.

Prior to running a gas breakthrough pressure experiment, the sample must initially be saturated with formation brine. The sample is placed between two porous disks and is then sealed (Hildenbrand et al. 2002). It has been recommended by some researchers that either lead sleeves or lead foil with aluminum or copper sleeves should be used to seal the samples rather than the commonly used rubber sleeves (Hildenbrand et al. 2002; Hildenbrand et al. 2004; Li et al. 2005). This is done to prevent leaks that may occur since the CO_2 can be absorbed into the rubber sleeve.

These methods make use of a triaxial apparatus whereby the sealed sample is placed between two reservoirs, one upstream, which transmits pressurized gas through the sample, and one downstream. A confining pressure and axial stress representative of in situ conditions is applied to the sample during the experiments.

2.2.1.1 Small Incremental Pressure Increase Procedure

To perform a gas breakthrough pressure experiment using small incremental pressure increases, the gas is injected at the inlet end at a low pressure (Li et al. 2005a and 2005b). A low initial pressure is used so that the gas breakthrough pressure is not unintentionally exceeded. In published test procedures, a meniscus of displaced fluid is observed in a scaled capillary tube at the outlet end of the sample. Once this meniscus has been stationary for at least 4 hours, the next pressure increment is applied. Pressure increments of approximately 0.5 MPa to 1.0 MPa are used (Li et al. 2005a and 2005b). The limitation of this approach is that the downstream end of the sample is at atmospheric pressure.

These steps are repeated until a continuous slow liquid flow occurs, followed by liquid flow containing gas bubbles, which indicates that breakthrough has occurred. The gas breakthrough pressure is then defined as the displacing pressure of the last pressure increment (Li et al. 2005a and 2005b). An illustration of the type of results obtained from this method are presented in Fig. 2.5.

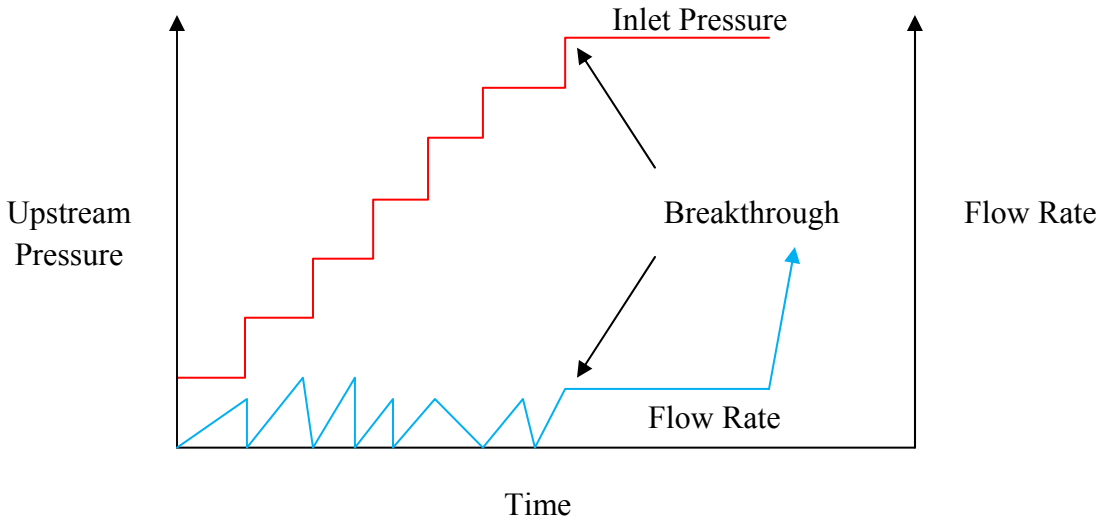

Fig. 2.5. Example experimental results for a gas breakthrough pressure experiment using small incremental pressure increases.

2.2.1.2 Large Instantaneous Pressure Increase Procedure

To perform a gas breakthrough pressure experiment using a large instantaneous pressure increase, the instantaneously high pressure gradient is applied across the sample by increasing the pressure in the upstream reservoir (Hildenbrand et al. 2002; Hildenbrand et al. 2004). There are two ways of doing this. The first method, Method A (see Fig. 2.6), involves keeping the upstream reservoir at a constant, high pressure. The second method, Method B, involves filling the upstream reservoir with high-pressure gas and then sealing the reservoir (Hildenbrand et al. 2002).

Once the pressure gradient is applied to the sample, the pressure in the downstream reservoir increases (see Fig. 2.6). Assuming that the gas is non-wetting, the pressures in each reservoir will never become equal; rather a residual pressure difference will remain, which is defined as the gas breakthrough pressure (Hildenbrand et al. 2002).

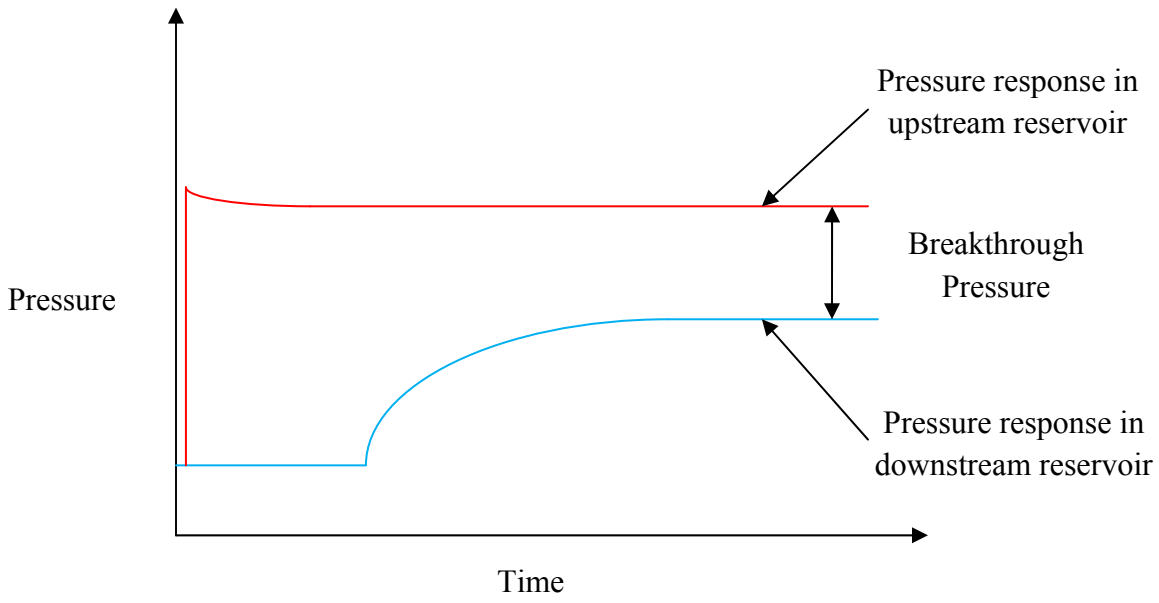

Fig. 2.6. Example experimental results for a gas breakthrough pressure experiment using instantaneously high pressure increase (Method A).

2.2.3 Comparison of Methods

Results of Li et al. (2005) indicate that a CO_2 breakthrough pressure experiment performed on anhydrite samples from the Weyburn caprock took about 4 to 5 days, with a CO_2 breakthrough pressure of about 10 MPa. Hildenbrand et al. (2002) report CO_2 breakthrough pressures ranging between 0.1 MPa to 0.5 MPa for claystone and siltstone samples. These tests took approximately 30 hours. It can be seen that experiments using small incremental pressure increases take more time than those using instantaneously high pressure gradients. Also, the former method has been known to measure gas breakthrough pressures that are lower than values determined by the latter method by factors ranging from 2 to 5 (Zweigel et al. 2005).

2.3 In-Situ Methods

Ostrowski and Ulker (2008) used an in-situ method to determine gas threshold pressure. Wellbore isolation tools were used to isolate a portion of the rock within the wellbore. The

liquid within that isolated section was replaced with gas at the same hydrostatic pressure that existed within the well. Then, a constant-rate injection of the gas was used to determine the gas threshold pressure.

The results obtained using this in-situ method give gas threshold pressures under real in-situ conditions of temperature, overburden, and pressure. However, the results of this method are affected by both the undamaged caprock as well as the part that has been damaged from drilling. Therefore, this method should be used in conjunction with laboratory techniques. Moreover, this method is expensive and requires downhole access.

Neuzil (1980) reported results of in-situ hydraulic conductivity tests conducted on the Pierre Shale using a modified slug test. He concluded that only a small area surrounding the borehole affected the test, and that this small area is most likely the area that was affected by drilling. Therefore, this method is not representative of the entire formation.

2.4 Factors Affecting Gas Breakthrough Pressure

2.4.1 Capillary Pressure

One of the key factors affecting caprock seal effectiveness, in conventional hydrocarbon reservoirs at least, is capillarity. That is, the large capillary pressures generated within the small, brine-filled pores of these rocks (AL-Bazali et al. 2005). The capillary pressure, P_{cap}, is expressed as

$$P_{cap} = \frac{2\sigma}{r} cos\theta = \frac{4\sigma}{d} cos\theta \tag{2.2}$$

where σ is the interfacial tension (IFT) between the non-wetting phase and the wetting phase. The term interfacial tension is used to refer to the amount of work that must be performed in order to separate a unit area of one fluid from another (e.g., Bear 1972). IFT therefore has units of work (*force* x *length*) per unit area ($length^2$); i.e., *force* x $length^{-1}$. The SI unit for IFT is N/m. r and d are the effective pore radius and diameter, respectively, along the pore throat [m], and θ is the contact angle of the fluid interface where it meets the pore surface, as measured within the denser of the two fluid phases (Fig. 2.7).

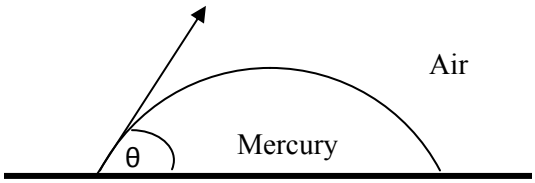

Fig. 2.7. Illustration showing contact angle for air-mercury system.

From equation 2.2, it can be seen that there is a linear relationship between the capillary pressure and both the IFT and the contact angle. Therefore, the ability of a caprock to effectively provide a seal in regards to CO_2 storage will depend on the IFT between CO_2 and the reservoir brine as well as on the contact angle in the presence of CO_2.

Chiquet et al. (2007) found that at higher CO_2 pressures within the reservoir, water wettability decreased and the repulsive forces between the CO_2 and reservoir brine were less effective compared with a system consisting of hydrocarbon and brine. In other words, the caprock provides a less effective seal in the CO_2/brine system than it does in the hydrocarbon/brine system. Therefore, the CO_2 has the potential to break through the caprock at a lower pressure than the hydrocarbon would. As a result, it is erroneous to assume that a given caprock which has been effectively sealing a hydrocarbon reservoir over geological time will provide the same capillary sealing capacity to a reservoir containing CO_2. As such, the effectiveness of a caprock (or aquitard) for containing CO_2 may be predominantly controlled by its fluid transport properties. These include volume flow properties (i.e., permeability) and diffusive flow properties. Permeability will be discussed at length later in this thesis.

2.4.2 Diffusion

Chiquet et al. (2007) stated that CO_2 diffusion through a brine-saturated caprock is so slow that it is only significant over geological time scales. Busch et al. (2008) did a series of diffusion experiments on the Muderong Shale of Australia. They concluded that, for a 100-metre-thick shale, CO_2 breakthrough would occur after approximately 0.3 million years. This is considered reasonable for geological storage of CO_2 (Busch et al. 2008).

Li et al. (2005) also concluded that diffusion is negligible when compared with volume for testing the Weyburn Midale caprock; i.e., anhydrite. It is possible that diffusion could have more significant impacts over the long term due to the mineralogical and geochemical interactions that occur as CO_2 interacts with the formation fluid and the host rock (Busch et al. 2008). For example, porosity and/or permeability may increase if minerals are dissolved. However, Gunter et al. (2004) stated that, for a carbonate reservoir in a closed system, the integrity of the rock is not significantly affected due to these geochemical interactions. Although the implications of geochemical interactions on caprocks have been less studied, it seems reasonable to expect that any such processes would occur very slowly, and only near the base of the caprock, for any caprock that serves as an effective flow barrier in the first place.

Further to the aforementioned potential for very slow leakage rates through a caprock due to diffusion, there are also local diffusional processes that may affect capillary breakthrough. Diffusion of CO_2 into a caprock occurs once the CO_2 dissolves into the caprock's saturated pore spaces (Busch et al. 2008). If the CO_2 dissolves into the pore water, the IFT between the pore water and the CO_2 will decrease. From equation 2.2, this will result in a decrease in the caprock's capillary pressure which will ultimately lead to a decrease in the breakthrough pressure.

2.4.3 Brine/CO_2/Rock Interactions

The containment of injected CO_2 can be enhanced by geochemical interactions that occur between the injected CO_2, formation brine, and the host rock (Gunter et al. 2004). Once the CO_2 dissolves into the formation brine, the pH of the formation brine will decrease (i.e., acidification) and this will lead to the dissolution of the caprock. As ions are released from the rock, the pH will increase which can lead to the precipitation of new minerals (Gunter et al. 2004). The dissolving of CO_2 into the formation brine is known as solubility trapping, the release of ions is known as ionic trapping, and the formation of new minerals is known as mineral trapping (Gunter et al. 2004).

Once solubility trapping has occurred, the CO_2 will no longer rise through the storage rock as a separate phase but will travel with the in-situ fluids. Gunter et al. (2004) report that these fluids can take millions of years to reach the surface.

After the CO_2 has dissolved in the formation brine, a weak acid is formed and will dissolve the minerals of the host rock. This weak acid reacts with silicate (e.g., feldspars, clay minerals) and carbonate minerals (e.g., feldspars, clay minerals, olivines) within the host rock (Gunter et al. 2004; Busch et al. 2008). As these reactions occur, the weak acid is eventually neutralized by forming carbonate or bicarbonate ions (Gunter et al. 2004).

These ions react with the rock matrix to form new carbonates (Gunter et al. 2004). The reactions occur between such minerals as clay minerals, micas, feldspars and chlorites (Gunter et al. 2004). This is the safest form of geochemical trapping (Gunter et al. 2004; Thibeau et al. 2007).

Fig. 2.7 (from Gunter et al. 2004) highlights the changes in mineral amounts that would occur in a siliciclastic aquifer after being exposed to a CO_2-charged environment.

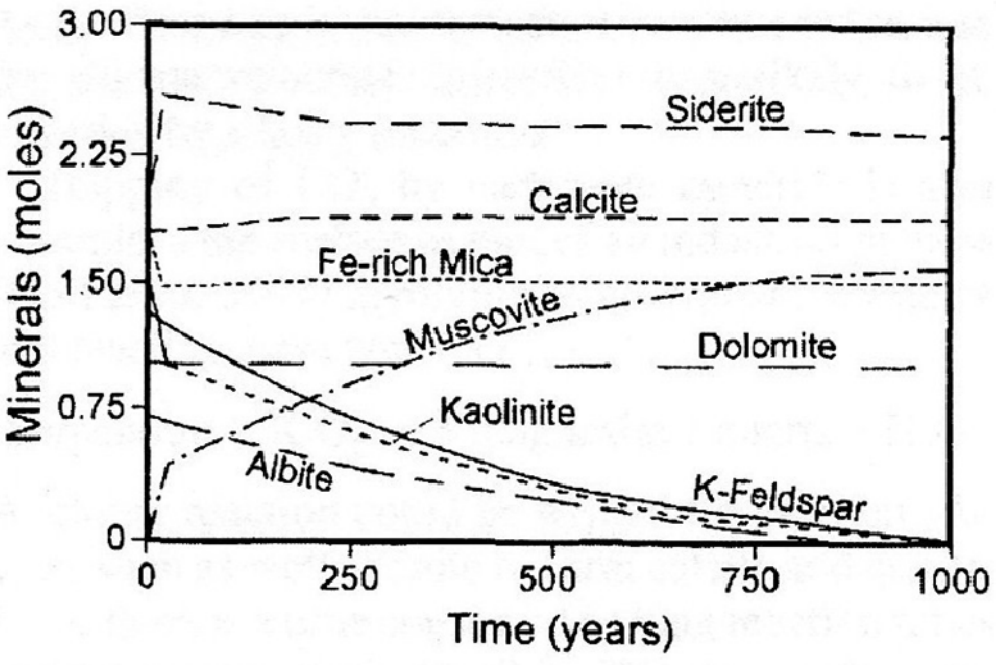

Fig. 2.7. Mineral changes that would occur in a typical siliciclastic aquifer when exposed to a CO_2-charged environment (from Gunter et al. 2004).

Busch et al. (2008) suggest that more detailed studies are necessary in order to get a better understanding of, and additional information on, mineral trapping and its effects on porosity and/or permeability in reservoir/aquifer rocks. Although geochemical effects were out of scope for this work, it is suggested that more detailed studies of CO_2-caprock interaction would also provide useful information.

2.5 Summary

Traditional methods of determining permeability do not work for fine-grained samples such as shale. As a result, the pressure pulse decay method developed by Brace et al (1968) must be used. In order for this method to be used accurately, the sample pore volume must be small relative to the reservoir volume used of the test equipment (Trimmer 1981). Determining permeability using Brace et al.'s method is conceptually simple, but is difficult to implement due to the fact that pressure change in the testing system is extremely sensitive to temperature change and small leaks.

In a formation brine/CO_2/rock system, the formation brine is considered the wetting phase and the CO_2 is considered the non-wetting phase. If the pressure differential between these two phases exceeds the capillary pressure of the rock at a sufficient number of pore throats to form a connected flow system from one side of a sample to the other, the CO_2 will be able to flow through the sample, at a rate governed by its effective permeability. Once this flow has been established, CO_2 breakthrough has occurred.

There is a lack of published information regarding what type of material is best for use as a seal. Lead foil and copper sleeves have been suggested; however, there have been no studies done to determine which material is most appropriate (copper sleeves vs. rubber membranes).

Recent research has shown that caprocks provide a less effective seal in a CO_2/brine system than they do in a hydrocarbon/brine system. Therefore, a given caprock which has been effectively sealing hydrocarbons over geological time will not necessarily do so for CO_2.

CO_2 diffusion through a brine-saturated caprock is only significant over geological time, and is negligible when compared with volume flow (Li et al. 2005; Chiquet et al. 2007).

Geochemical interactions on caprocks have not been studied extensively, but it is expected that these interactions would occur at the base of the caprock, and would occur very slowly. More studies are necessary to determine how geochemical interactions affect the porosity and permeability of caprocks.

3. SAMPLE CHARACTERIZATION AND ROUTINE ANALYSES

3.1 Introduction

Shale samples from the Lea Park Formation, taken from a well located near Weyburn, SK, and from the Colorado Group, taken from a well located near Rocanville, SK, were analyzed in this work (Fig. 3.1). The Lea Park Formation is stratigraphically located above the Colorado Group (Fig. 3.2). In the hydrostratigraphic section interpreted for the Weyburn area (Preston et al. 2005), the Lea Park Formation and the Colorado Group are grouped together and collectively referred to as the Colorado Aquitard, as shown in Fig. 3.3. The Lea Park Formation samples from well 121/06-08-006-13W2 were provided by the Petroleum Technology Research Centre in Regina, SK, and the Colorado Group samples from a borehole located at 04-34-016-33W1 were provided by Potashcorp of Saskatchewan (PCS). These samples are referred to as Lea Park shale and Colorado shale throughout this thesis.

Routine petrographic and petrophysical analyses of the Lea Park and Colorado shales were performed by a service laboratory in order to gain insight into the characteristics of these shales. Ideally, these characteristics would be known ahead of any additional testing that is to be done, in order to make informed choices regarding sample location as well as to have a better understanding of how the sample will behave. In this work, however, due to time and logistical constraints, the petrographic and routine petrophysical analyses were conducted in parallel with much of the specialized testing described in Chapters 4 and 5; regardless, the routine analyses were still valuable in that they provided context and insights for the interpretation of the specialized testing results.

Mercury injection porosimetry, x-ray diffraction (XRD), scanning electron microscope (SEM) analysis, and optical microscopy were performed for both the Lea Park shale and the Colorado shale. Table 3.1 lists the sample names and depths, as well as the tests that were performed on them.

All samples were taken from cores that had been wrapped in cellophane and aluminum foil and dipped in wax by service company personnel immediately after being cut out of their coring tubes in order to preserve the original moisture content as much as possible.

Table 3.1. Information on samples used for petrophysical characterization.

Formation	Sample Name	Depth (m)	Test Performed	
			Routine	Specialized[3]
Lea Park shale	CHRS-005	611.2*	Mercury Porosimetry[1]	
	CHRS-006	611.2*	Mercury Porosimetry[1]	
	LP1	602.3**	XRD[2], SEM[2], Optical Microscopy[2]	Permeability, CO_2 breakthrough pressure testing
	LP2	610.9		Permeability, CO_2 breakthrough pressure testing
	LP3	611.0	Velocity[3]	
Colorado shale	CS1	427.3		Permeability, CO_2 breakthrough pressure testing
	CS2	428.5	Mercury Porosimetry[1], XRD[2], SEM[2], Optical Microscopy[2]	Permeability, CO_2 breakthrough pressure testing

Remarks:

*: One sample was taken at this depth and then split into two pieces for mercury porosimetry testing.

**: One sample was taken at this depth and was subsequently divided for each of the tests.

1: Conducted by University of Alberta, Department of Physics

2: Conducted by GR Petrology Consultants Inc., Calgary

3: Conducted by the author of this thesis

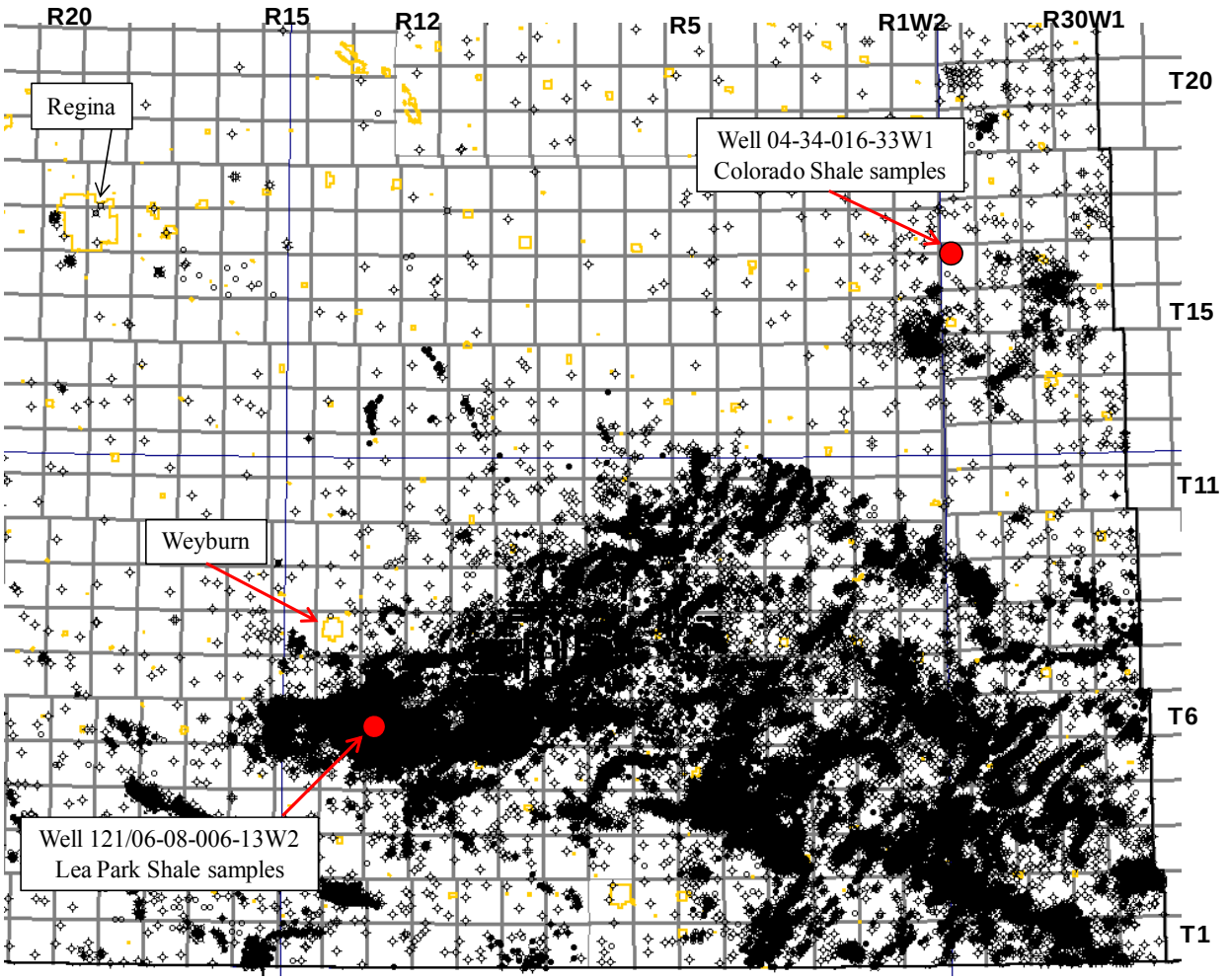

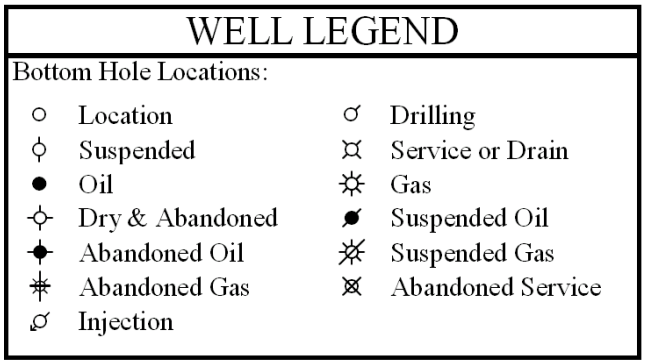

Fig. 3.1. Sample location map. Each square on the map grid shown has a width of 10 km.

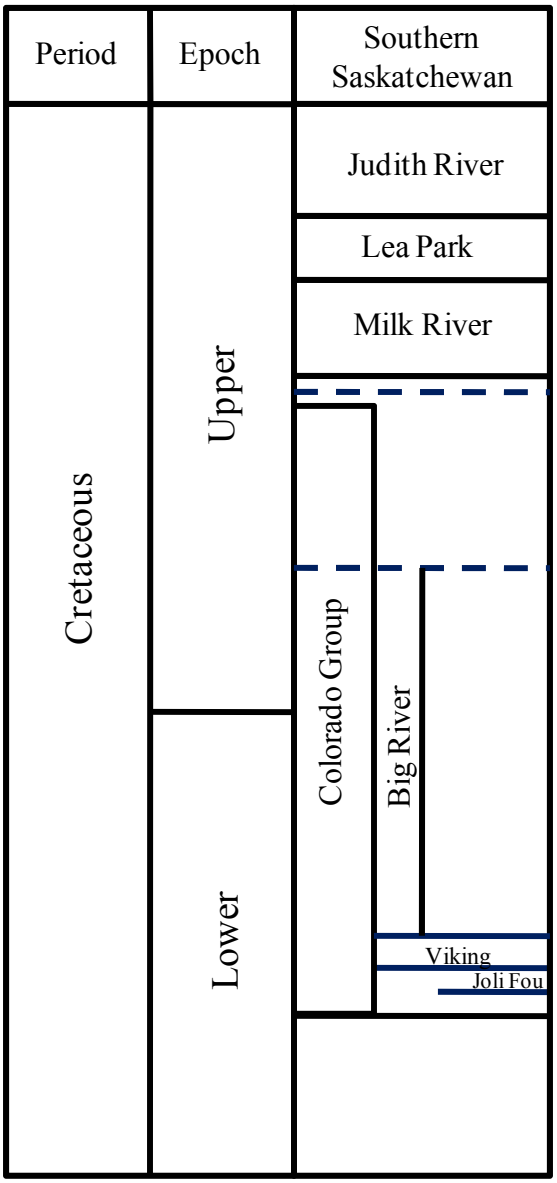

Fig. 3.2. Stratigraphic table for southern Saskatchewan showing the Lea Park and Colorado shale (after Leckie et al. 1994).

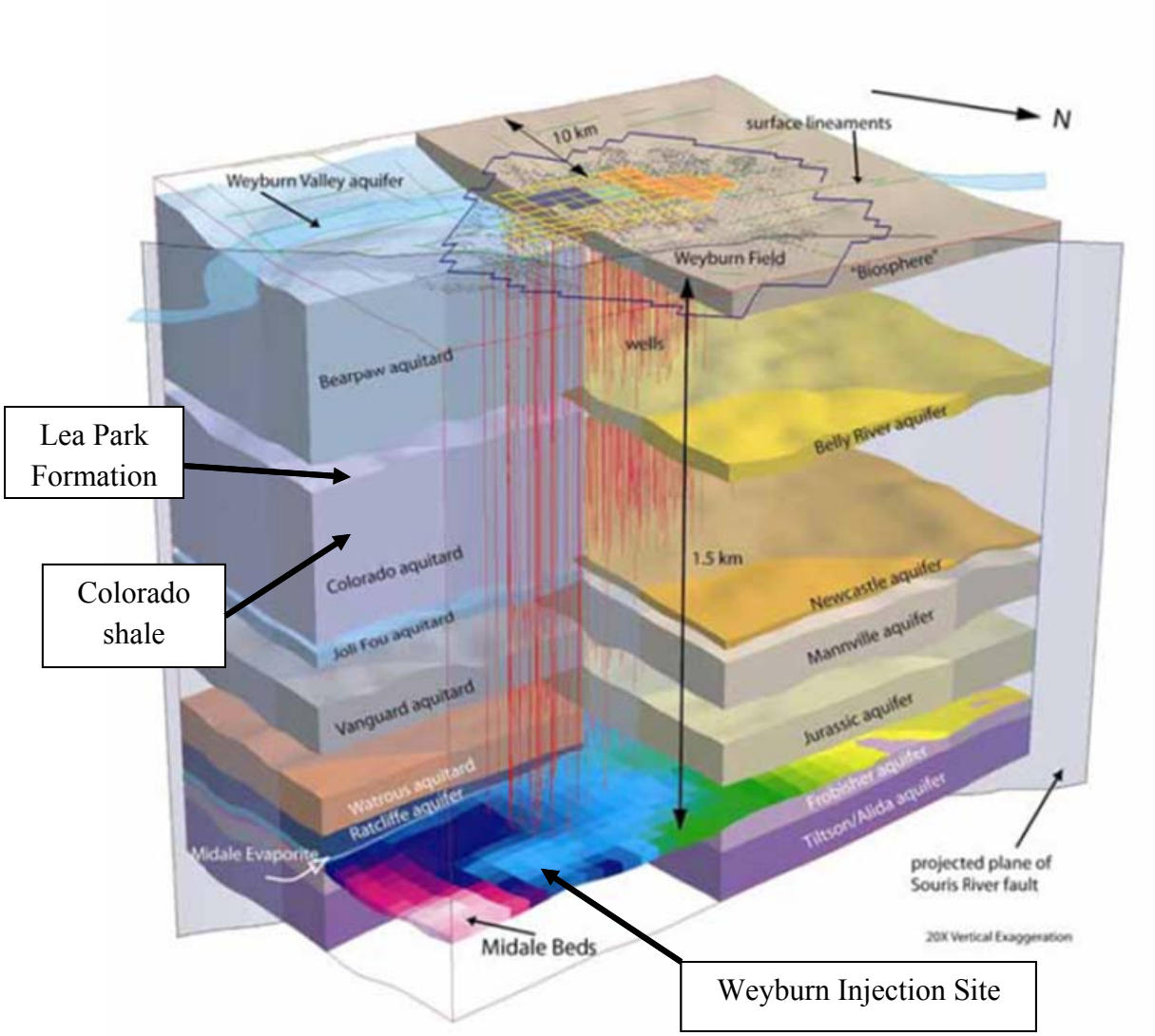

Fig. 3.3. Hyrdostratigraphic cross-section showing the Weyburn injection site and the Lea Park Formation (after Preston et al. 2005).

3.2 Lea Park shale

3.2.1 Geological Description

The Lea Park Formation consists predominantly of dark grey shale of upper Cretaceous age and lies immediately above the Colorado Group (Meijer Drees and Myhr 1981) (see Fig. 3.3). The Lea Park Formation is located at a depth of approximately 600 m in the Weyburn area and its thickness ranges between 120 m and 170 m (Christopher and Yurkowski 2003). The Lea Park Formation is laterally extensive, covering more than the 200 km by 200 km area considered in the Weyburn project migration models conducted to date. As part of the Colorado Aquitard, the Lea Park Formation provides one of the regional barriers to the upward migration of CO_2 from the Weyburn injection site. It is the second-to-last barrier against leakage to shallow aquifers and/or to the surface.

See Fig. 3.4 (a) and (b) for photos of Lea Park shale samples used in this research.

(a) (b)

Fig. 3.4. (a) Sample LP1 (pre-testing); and (b) Sample LP2 (pre-testing).

3.2.2 Geophysical Well Logs

Geophysical well logs for the Weyburn well from which the cores used in this research were obtained (i.e., 121/06-08-006-13W2) are presented in Fig. 3.5. The Lea Park shale occurs at depths from approximately 481.1 m to 614.7 m in this well.

Gamma ray logs (Fig. 3.5 (a)) are used as a lithology indicator. Shales and clays are naturally radioactive so they can be identified by high values on such logs.

Caliper logs (Fig. 3.5 (b)) are used to measure the diameter of the borehole and to indicate the quality of the borehole; e.g., if washouts or breakouts are present.

Resistivity logs (Fig. 3.5 (c)) are used to provide indirect indicators of pore fluid composition. In petroleum engineering applications, they are mostly used because they are sensitive to differences between water (less resistive) and hydrocarbon (more resisitive). In water-saturated formations, they can also indicate changes in groundwater salinity (because resistivity decreases with increasing salt content).

Photoelectric factor logs (Fig. 3.5 (d)) are used as lithology indicators. They are effective, for example, for distinguishing sandstone units from other lithological units.

Density logs (Fig. 3.5 (e)) are used to determine the bulk density of the formations being logged.

Sonic logs (Fig. 3.5 (f)), which measure the interval transit time (i.e., reciprocal of velocity) of acoustic waves, are used as an indirect indicator of porosity (i.e., all else being equal, higher transit time indicates higher porosity – which may be a consequence of higher matrix porosity or higher secondary porosity due to fractures or vugs). These logs are also useful for estimating rock mechanical properties. For example, dynamic Young's modulus and Poisson's ratio can be calculated directly from these logs, when both compressional and shear wave transit times are measured. Empirical correlations may then be used to estimate static elastic properties and strength properties as a function of these dynamic properties.

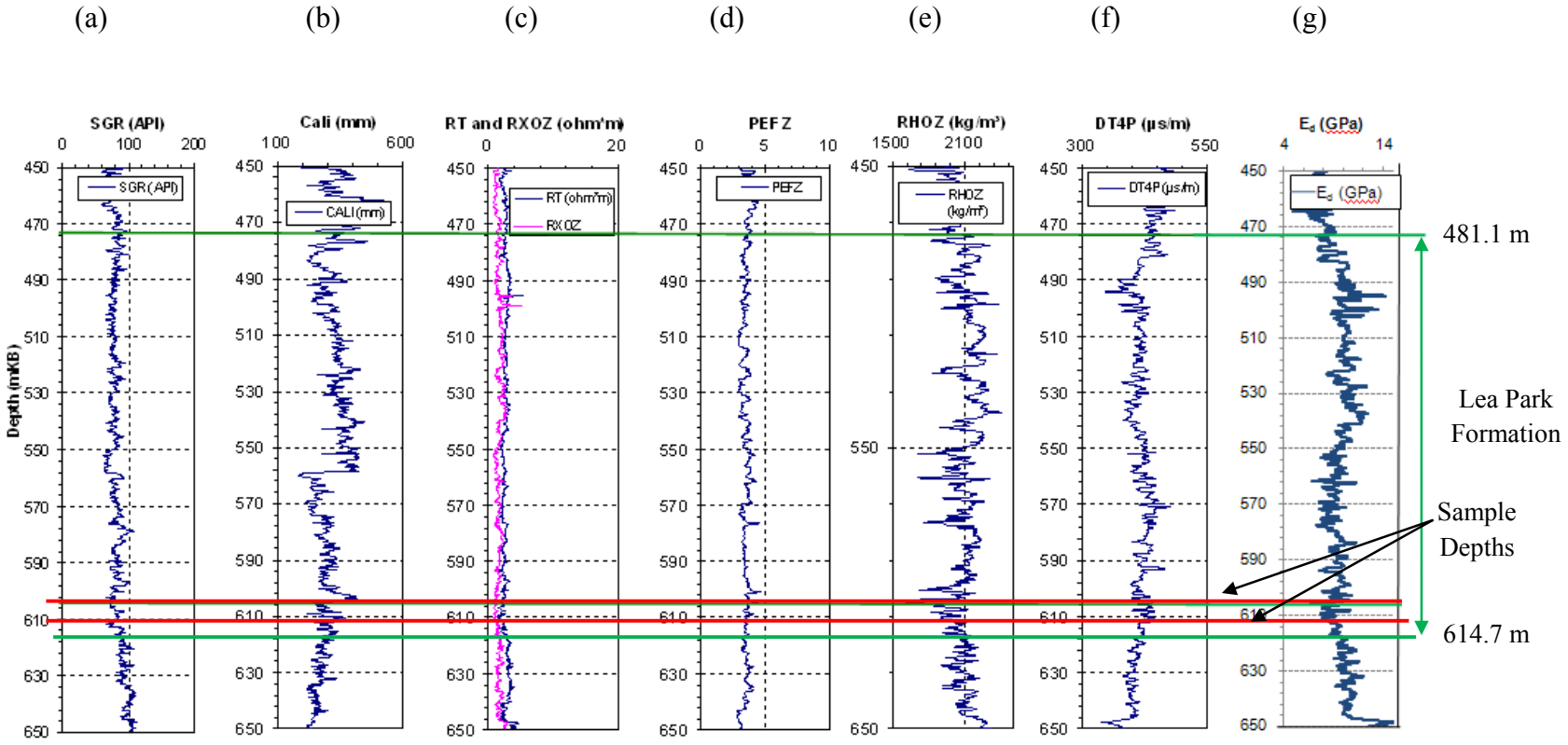

Fig. 3.5. Composite well logs for well 121/06-08-006-13W2: (a) gamma ray log; (b) caliper log; (c) resistivity log; (d) photoelectric factor log; (e) density log; (f) sonic log; and (g) calculated dynamic Young's modulus (E_d). [Note: Since no shear wave data were collected in the logging program for this well, E_d was calculated using the bulk density and compressional sonic data collected by geophysical logs, in combination with the Vp/Vs ratio determined by lab testing presented in Section 3.2.8]

Analysis of these logs indicates that the Lea Park shale is quite consistent in terms of lithology and pore fluid composition. The sonic log (Fig. 3.5 (f)) is also relatively uniform; notably, no thick zones with anomalously high transit times – of a nature that might suggest extensive natural fracturing - are present.

3.2.3 Optical Microscopy

A 60-mm thin-section was taken from a 75-mm diameter sample, LP1, perpendicular to bedding. The thin-section was prepared by GR Petrology in Calgary, AB. Jenapol and Leica polarizing microscopes were used in the thin-section analysis.

Thin section analysis indicated that the Lea Park shale is "notably fissile, very well sorted, argillaceous quartzose siltstone" (GR Petrology 2009). The framework is dominated by silt size monocrystalline quartz grains (38.3%). The matrix is "composed of carbonate fines, clay, carbonaceous material, phosphatic material, and silicate fines" (GR Petrology 2009).

Mineralogy determined by thin section analysis is presented in Table 3.2. Selected images are presented in Figs. 3.6 and 3.7.

Table 3.2. Thin section analysis results for sample LP1.

Component	Percentage
Quartz	41.9
Feldspar	4.7
Dolomite	5.3
Calcite	2.7
Pyrite	2.7
Clay	23.7
Glauconite	0.3
Phosphate	12.4
Organic Material	5.0
Sulphate	1.3

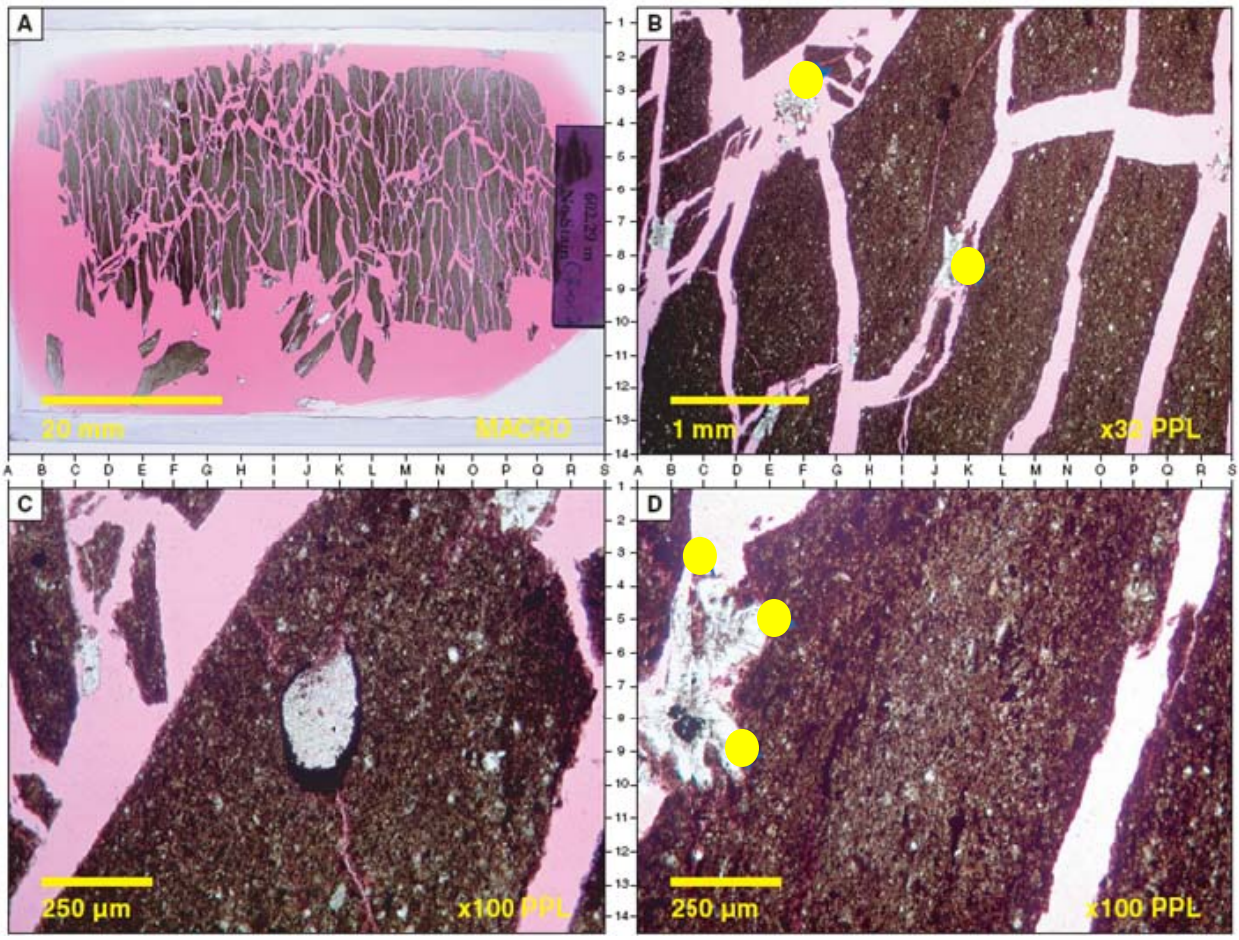

Fig. 3.6. Optical microscopy images for sample LP1. (A) indicates fissile nature of Lea Park shale; (B) and (D) yellow dots indicate minor anhydrite cement present along weakened and presently split sections of sample.

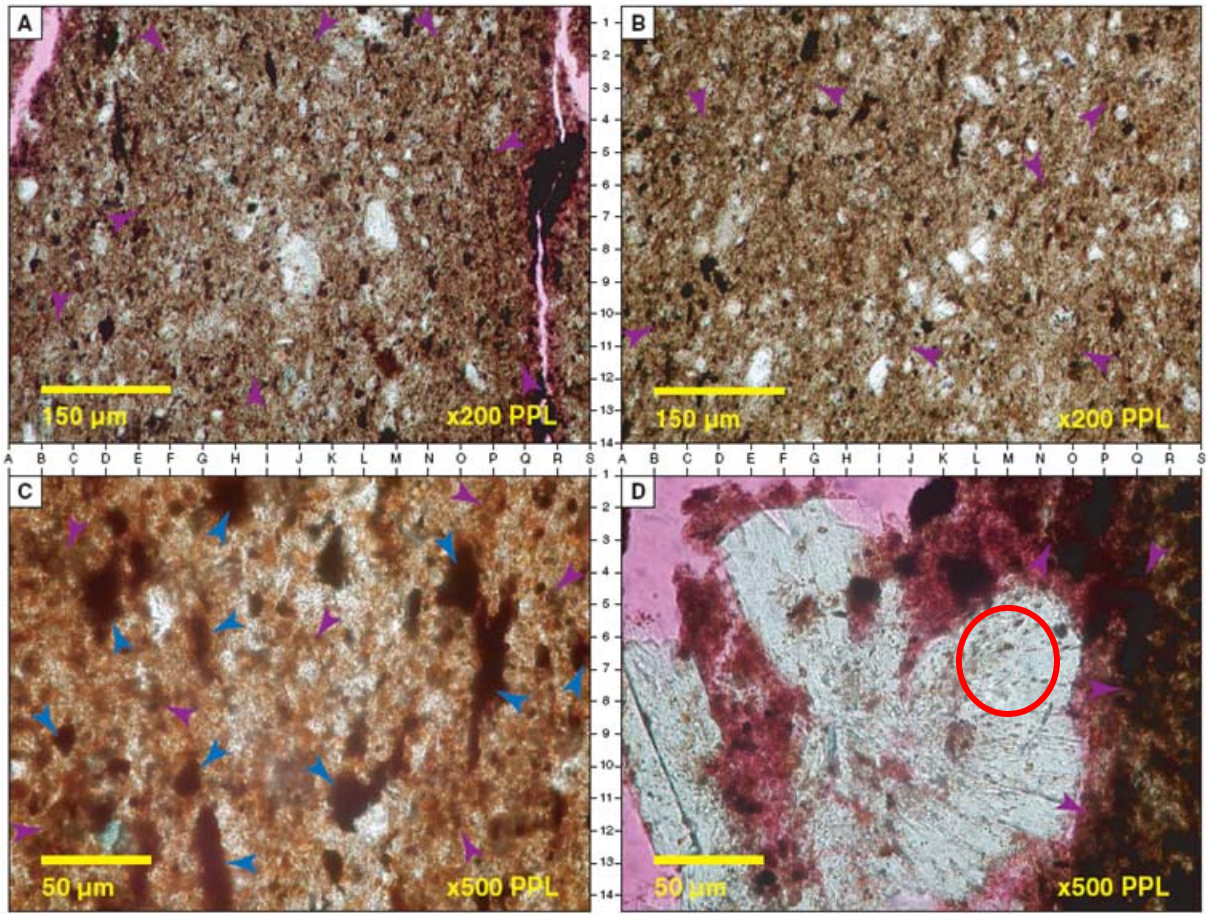

Fig. 3.7. Optical microscopy images for sample LP1. (C) phosphatic fragments and peloids are indicated by blue arrows; (D) red circle highlights anhydrite cement; (A) to (C) monocrystalline quartz grains can be seen (white grains).

3.2.4 X-Ray Diffraction

X-ray diffraction (XRD) analysis was conducted on sample LP1 to assess mineralogy which may affect wettability, hence capillary pressure. This analysis was performed by GR Petrology in Calgary, AB, using a Phillips XRG-3100 x-ray diffraction system along with MD Jade software.

XRD analysis determined that the matrix is composed largely of compacted and variably bitumen-impregnated admixed clay, carbonaceous and phosphatic material, and silicate fines (32.3%). The clay fraction is composed of kaolinite, illite, chlorite, and smectite. The results of the bulk XRD analysis are presented in Table 3.3.

The clay fraction was further studied using glycolated clay fraction XRD analysis in order to better distinguish the amounts of each specific clay component within the total clay fraction. This process is described in detail in the GR Petrology Consultants report (2009). These results are presented in Table 3.4.

Table 3.3. Bulk XRD results for sample LP1.

Component	Percentage
Quartz	59.8
Plagioclase	6.3
Potassium Feldspar	4.1
Anhydrite	1.4
Pyrite	2.0
Calcite	2.8
Dolomite	3.0
Kaolinite	10.0
Illite	9.2
Chlorite	1.4
Smectite	Present

Table 3.4. Glycolated clay fraction XRD results for the clay fraction for sample LP1.

Component	Percentage
Kaolinite	32.8
Illite	30.4
Chlorite	11.0
Smectite	25.8

Discrepancies exist between the mineralogy determined from XRD analysis and thin section analysis. XRD analysis does not detect non-crystalline phosphatic material or organic material, which was detected in the thin section analysis. Also, differences between the two could be due to localized variations in the mineralogy of the locations from where the samples were taken. The thin section analysis is likely more representative of the bulk composition of the sample since it samples a larger portion of the sample than XRD analysis does.

3.2.5 Scanning Electron Microscopy

Scanning electron microscope (SEM) analysis was performed in sample LP1 by GR Petrology in Calgary, AB. The SEM analysis was performed using a JEOL 5800 SEM.

SEM analysis indicates that the fabric of the Lea Park shale is significantly argillaceous and that the matrix is composed of compacted clays. Also, micropores were visible throughout the fabrics of these clays. Images from the SEM analysis are presented in Figs. 3.8 and 3.9.

3.2.6 Mercury Injection Porosimetry

Mercury injection porosimetry is used to determine the pore volume and pore size distribution of a soil or rock in terms of the apparent diameters of the entrances of its pores (ASTM-D4404 2004). Initially, the sample is placed under vacuum to evacuate any air that may be present in the pore spaces. During a mercury intrusion porosimetry test, mercury – which is a non-wetting fluid for most rocks – is injected into the sample at increasing pressures. These pressures are then converted to apparent pore diameters using eq. 2.2, where P_{cap} represents the pressure of the intruding mercury. When analyzing mercury injection porosimetry results, it is assumed that the pores within the sample being tested are cylindrical with one constant diameter. Only the pores that are in hydraulic communication with the outside of the soil or rock sample can be intruded by the mercury; pores that are completely enclosed will not be intruded.

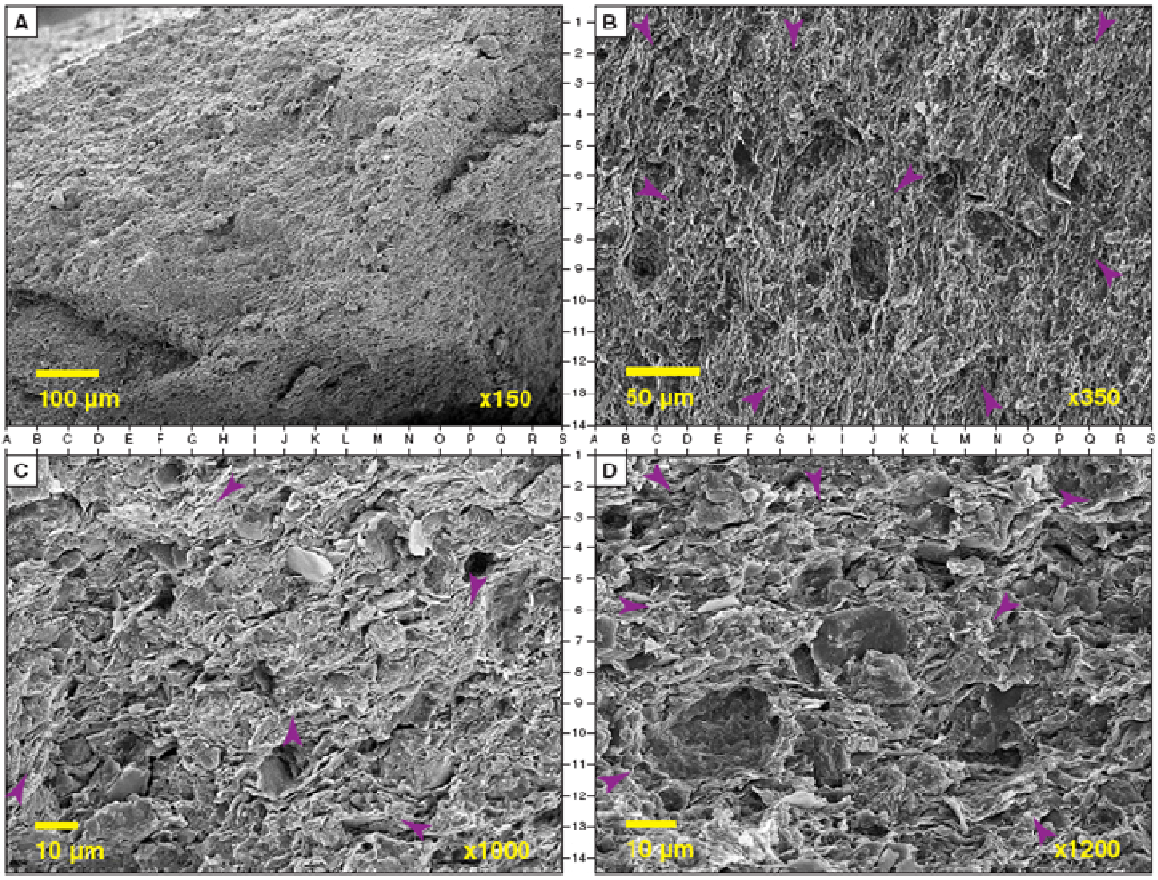

Fig. 3.8. SEM images for sample LP1. (B) to (D) purple arrows highlight matrix and pseudomatrix.

Mercury injection porosimetry was performed by a technician in the Department of Physics at the University of Alberta. These experiments were performed using an AutoPore IV 9500 porosimeter on two samples, CHRS-005 and CHRS-006, from the Lea Park shale. A surface tension of 0.485 N/m and a contact angle of 130° were assumed for these experiments based on values given in ASTM-D4404 (2004).

The critical pore diameter, d_{crit}, (i.e., the pore diameter that is deemed to control fluid migration throughout a rock's pore system, according the percolation theory-based analysis of flow in porous media presented by Thompson et al. 1987) can be interpreted using a plot of applied pressure versus the fraction of pore volume that has been invaded as a result of the applied pressure. The pressure at which the first sharp rise occurs is used to calculate the critical pore diameter from eq. 2.2.

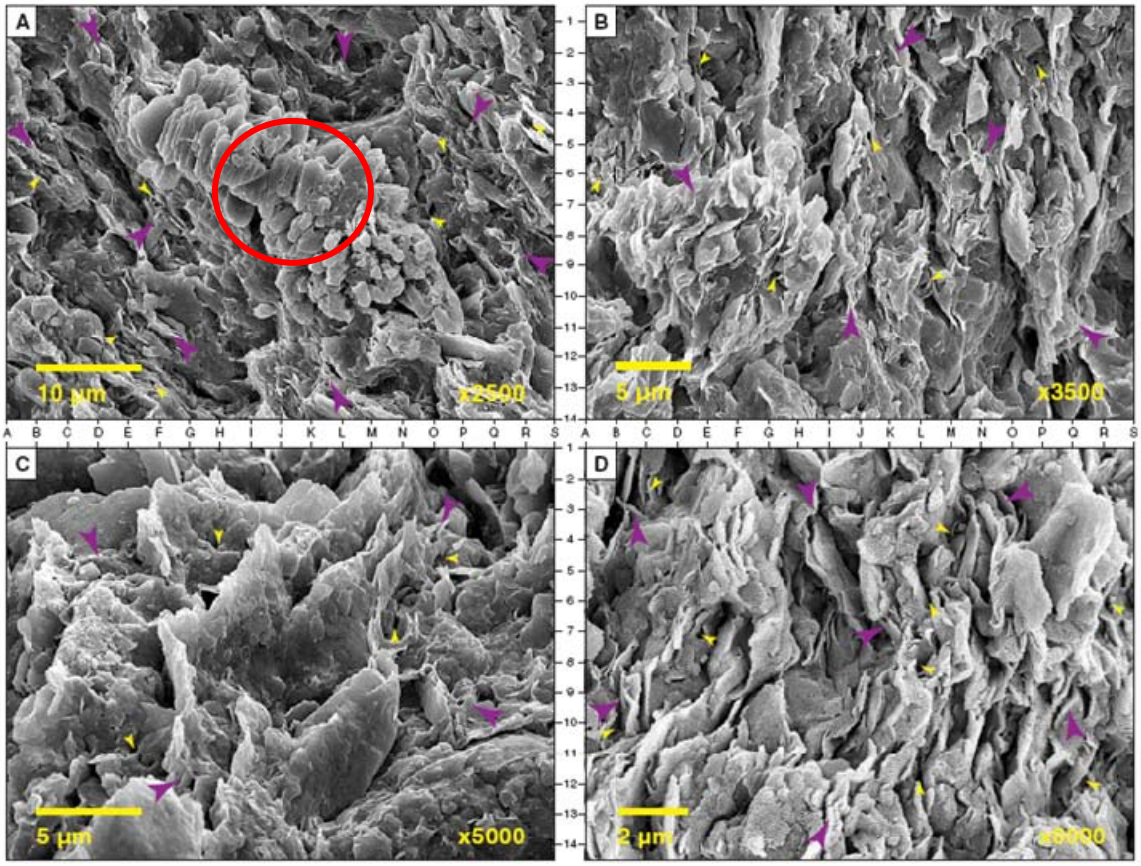

Fig. 3.9. SEM images for sample LP1, viewed at higher magnification than the images shown in Fig. 3.8. (A) to (D) micropores indicated by small yellow arrows; (A) red circle indicates poorly attached, admixed calcite and silicate fines.

The critical pressure for CHRS-05 was interpreted by taking the intersection point of tangent lines drawn on the volume-pressure curve for this sample. As shown in Fig. 3.10(b), a value of approximately 30 MPa was obtained. Using this pressure, and rearranging eq. 2.2, the critical diameter is obtained as follows:

$$d_{crit} = \left(\frac{4\sigma \mid cos\theta \mid}{P}\right)$$

$$d_{crit} = \left(\frac{4 \cdot 0.485\, {}^{N}/_{m} \mid cos130° \mid}{30 \cdot 10^{6} Pa} \right)$$

$$d_{crit} = 2.4 \cdot 10^{-8} m$$

$$d_{crit} = 0.02 \mu m$$

[Note: Using the absolute value of $cos\ \theta$ is a modification required for eq. 2.2 in order to avoid the calculation of negative capillary pressures in cases where the denser fluid phase (e.g., mercury, in a mercury-air system) is the non-wetting phase. This issue stems from the convention of measuring the contact angle within the denser fluid phase.]

Similarly, the critical pore diameter for CHRS-006 was determined to be 0.03 μm. This was calculated using a critical pressure of 25 MPa, interpreted as shown in Fig. 3.11(b). Summaries of the results for each sample are presented in Table 3.5.

From Figs. 3.10(a) and 3.11(a), it can be seen that perhaps not all of the pore volume was intruded during the tests. If all of the pore space had been intruded, the differential intrusion graphs would have returned to zero at the smallest pore size (i.e., highest intrusion pressure); however, they did not. The mercury porosimeter has a maximum pressure that it can apply and once that pressure is reached, additional small-diameter pores, if present, cannot be intruded. Therefore, pores with diameters requiring higher intrusion pressures may exist within these samples. Porosity results obtained by using the water saturation method (e.g., Fetter 1994) on a sample of Lea Park shale indicate that the porosity of this sample is approximately 22%, which falls in between the porosities of 18% and 25% determined from the mercury injection porosimetry. Therefore, it seems reasonable to conclude that the total volume of uninvaded pores is relatively small.

The critical pore diameters obtained from the mercury injection porosimetry will later be used, along with results from CO_2 breakthrough pressure testing, to back-calculate a contact angle between CO_2 and brine (Section 6.2.3). One potentially useful outcome of this type of analysis is the ability to predict CO_2 breakthrough pressure using mercury porosimetry results for other Lea Park shale samples (and to provide rough estimates for other formations with similar lithologies).

(a)

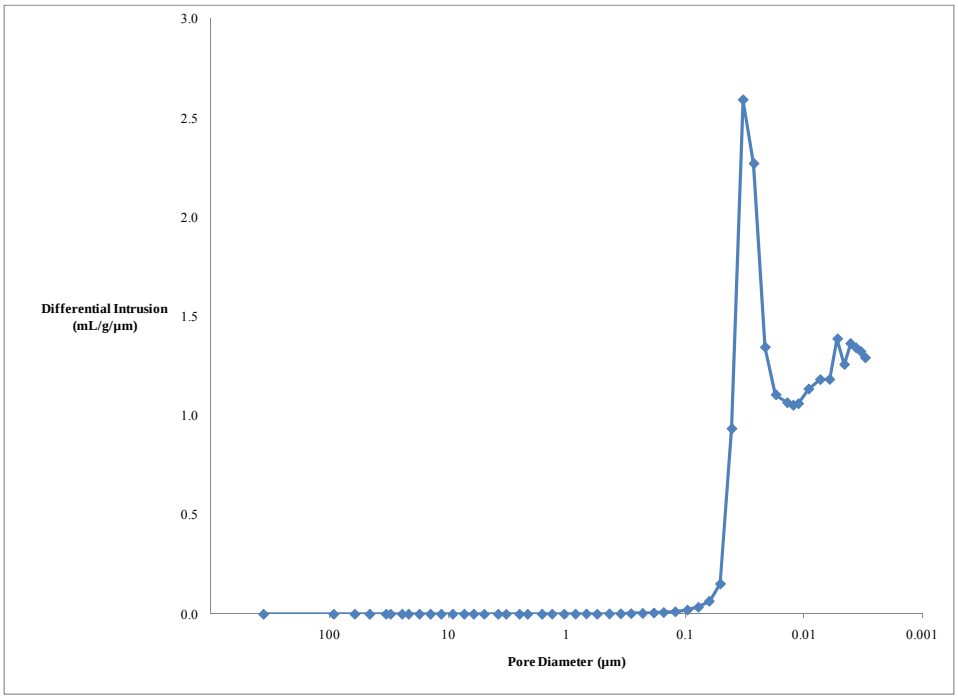

(b)

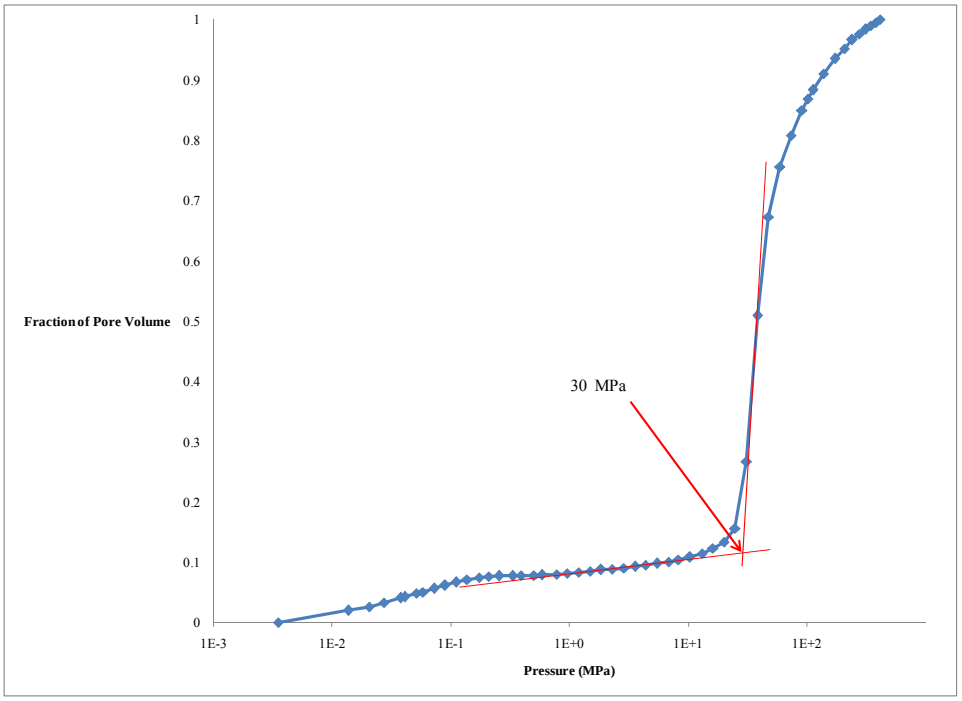

Fig. 3.10. Results of mercury injection porosimetry for sample CHRS-005: (a) differential intrusion; and (b) fraction of pore volume.

(a)

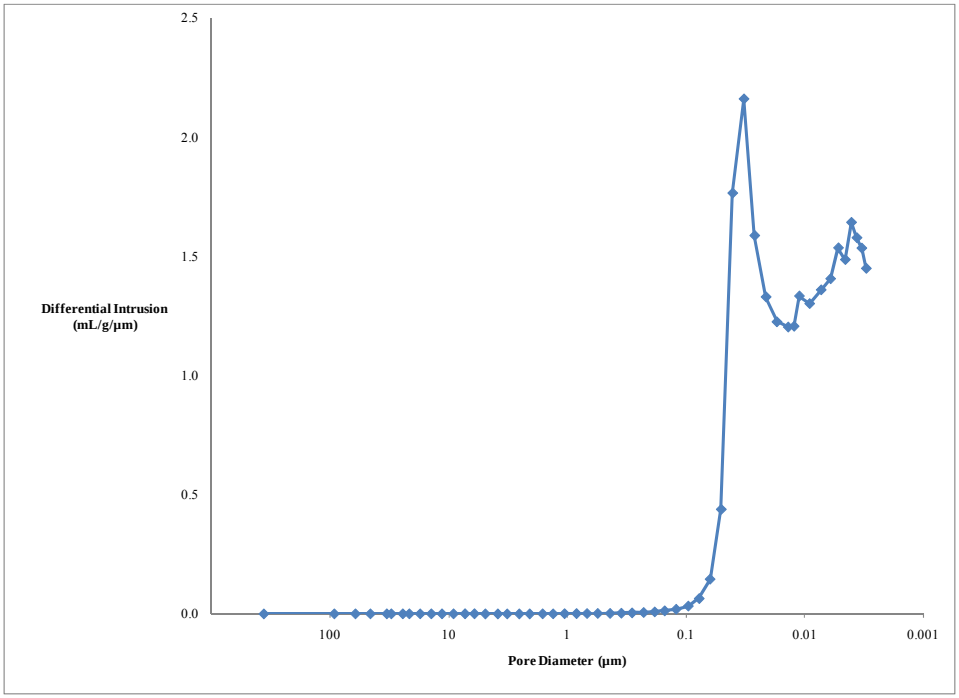

(b)

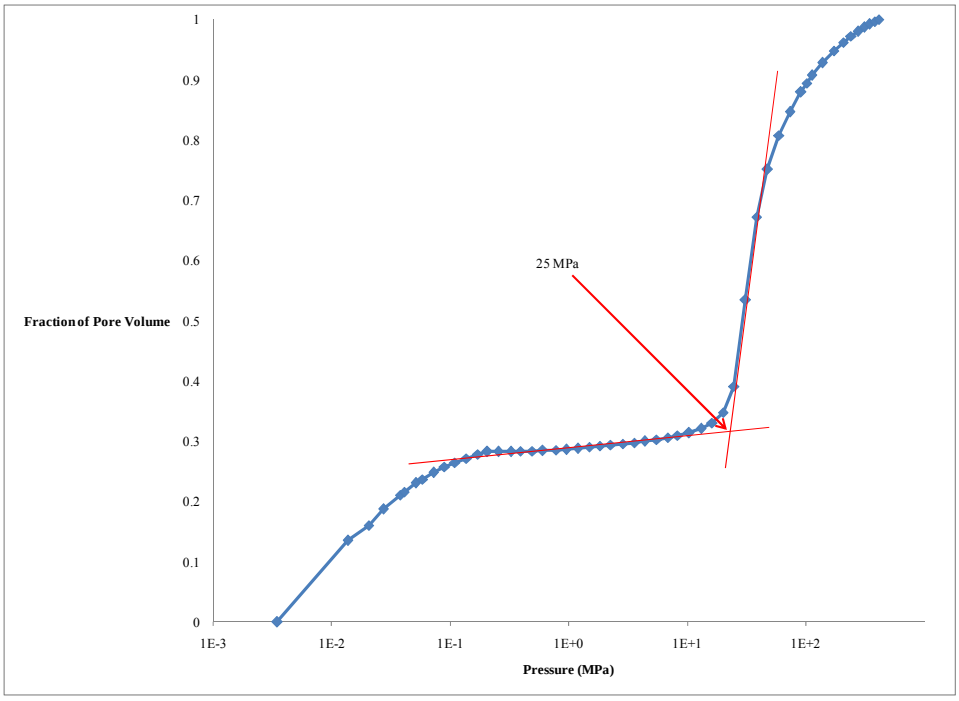

Fig. 3.11. Results of mercury injection porosimetry for sample CHRS-006: (a) differential intrusion; and (b) fraction of pore volume.

Table 3.5. Results of mercury intrusion porosimetry
for samples CHRS-005 and CHRS-006.

	CHRS-005	**CHRS-006**
Critical Pore Diameter (μm)	0.02	0.03
Range of Diameters (μm)	0.003 – 91	0.003 – 91
Mean Diameter (μm)	8	8
D_{10} (μm)	0.02	0.02
D_{50} (μm)	0.003	0.003
D_{90} (μm)	0.002	0.002
Porosity	18%	25%

3.2.7 Work Previously Completed on the Lea Park shale

From 2003 to 2005, largely unpublished work on the Lea Park shale was completed by Ting-Kai Chan, who was a graduate student in the Environmental Engineering Division of the University of Saskatchewan at the time. This work made use of cores for the same 121/06-08-006-13W2 well that was used in this thesis, and included the determination of geotechnical index properties, mineralogical and petrographical properties, and pore fluid composition, as well as oedometer swelling tests, permeability measurements and CO_2 breakthrough tests. Sample depths and testing types conducted are summarized in Fig. 3.12. Results of this work, some of which were presented in Chan and Hawkes (2005), are summarized in this section.

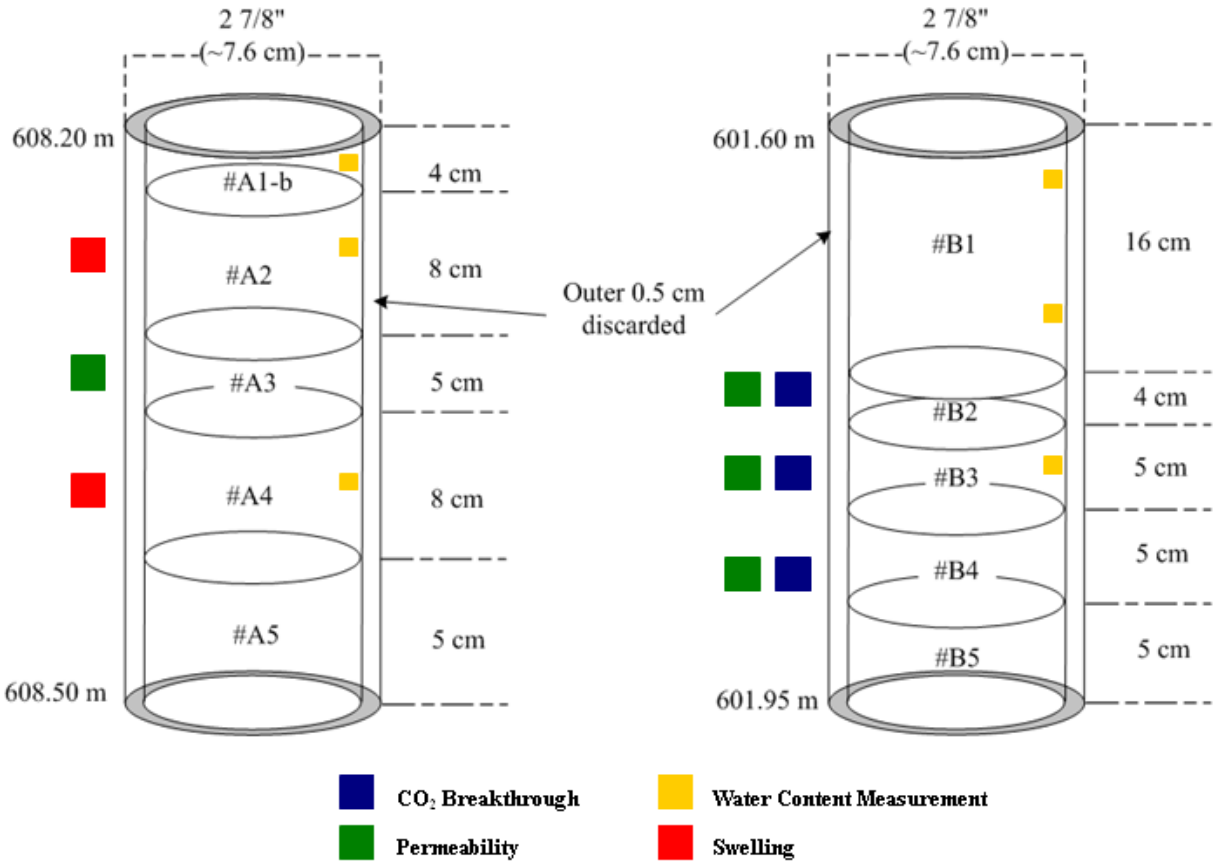

Fig. 3.12. Sampling depths and test types for work previously conducted on Lea Park shale samples from well 121/06-08-006-13W2 (unpublished figure, courtesy of Ting-Kai Chan).

3.2.7.1 Geotechnical Index Properties

Water content and Atterberg limits were determined for 6 samples. The water contents ranged between 16.1% and 18.5%, with a mean water content of 17.0%. The plastic limit was found to be 22.5% and the liquid limit was found to be 94.7%.

3.2.7.2 Mineralogy and Petrography

XRD and SEM analyses were conducted on samples from the Lea Park shale. Results of the XRD analysis indicated that there are significant proportions of quartz (24.8%), illite (16.7%), and illite-montmorillonite (33%). These earlier results are different from the ones obtained by this author. This could be due to variability in rock properties between

sampling depths, and – to some extent – differences in the equipment used, testing procedures followed, analytical software used, operator proficiency, etc.. Results of the SEM analysis indicated that bedding was well-defined with local crenulations and splays leading to the conclusion that the Lea Park shale would be anisotropic. SEM images are presented in Fig. 3.13 (a) to (d).

(a) (b)

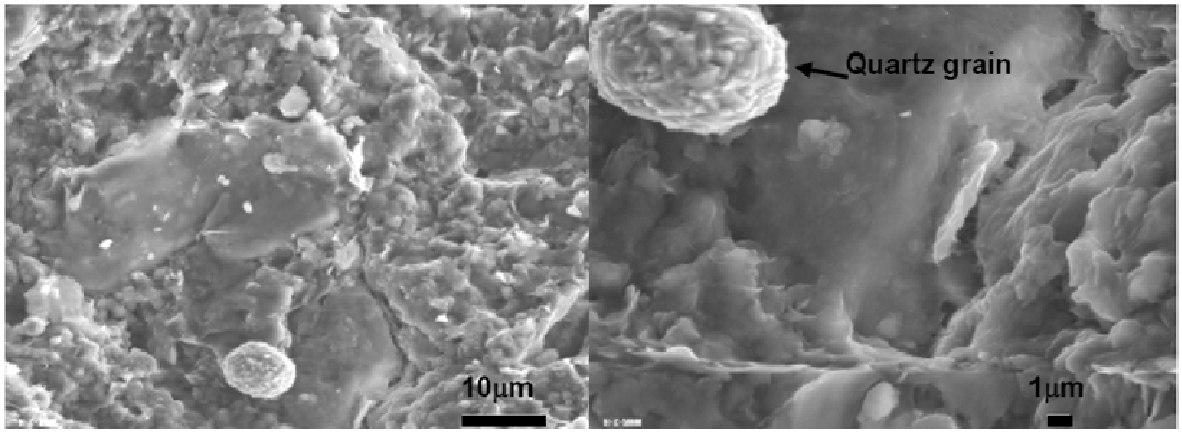

(c) (d)

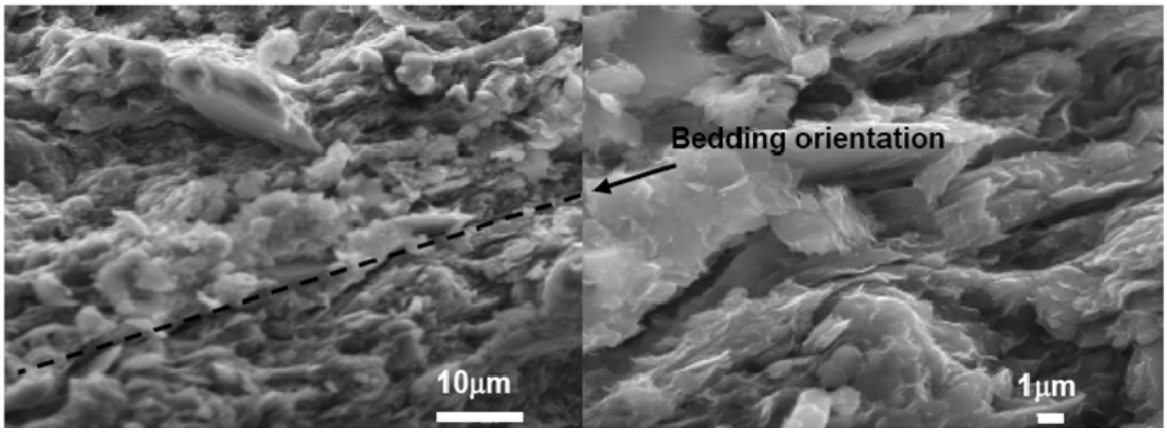

Fig. 3.13. SEM images for a sample of Lea Park shale from a depth of 608.20 m.

3.2.7.3 Pore Fluid Analysis

A pore fluid sample was obtained by squeezing a sample of the Lea Park shale at 70 MPa in a triaxial cell, and was analyzed by technical staff in the University of Saskatchewan's Department of Geological Sciences. Results of the pore fluid analysis are presented in Table 3.6.

The total dissolved solids of the tested pore fluid was determined to be 7.57 g/L (7570 ppm), the pH was determined to be 8.5, and the electrical conductivity was determined to be 12.75 mS/cm. This pore fluid's anion content is dominated by sulfate and chloride, and the cation content by sodium.

3.2.8 Ultrasonic Velocities and Dynamic Elastic Properties

Ultrasonic velocity testing was performed on one sample of Lea Park shale, Sample LP3. Only one test was performed due to the lack of sufficient, competent core sample remaining at the conclusion of all the characterization tests and petrophysical property measurements presented elsewhere in this thesis. Testing was performed using a Carver Laboratory Press and a Tektronix TDS5104B Digital Phosphor Oscilloscope (oscilloscope). See Figs. 3.13 and 3.14, respectively.

Table 3.6. Results of pore fluid analysis (after Chan and Hawkes 2005).

Anions	**F^-**	**Cl^-**	**NO_2^-**	**Br^-**	**NO_3^-**	**PO_4^{---}**	**SO_4^{--}**	**HCO_3^-**
(mg/L)	-	1821	-	-	-	-	2646	157

Cations	**Li^+**	**Na^+**	**NH_4^+**	**K^+**	**Mg^{++}**	**Ca^{++}**
(mg/L)	-	2889	-	9	6	44

Fig. 3.13. Carver Laboratory Press with Sample LP3.

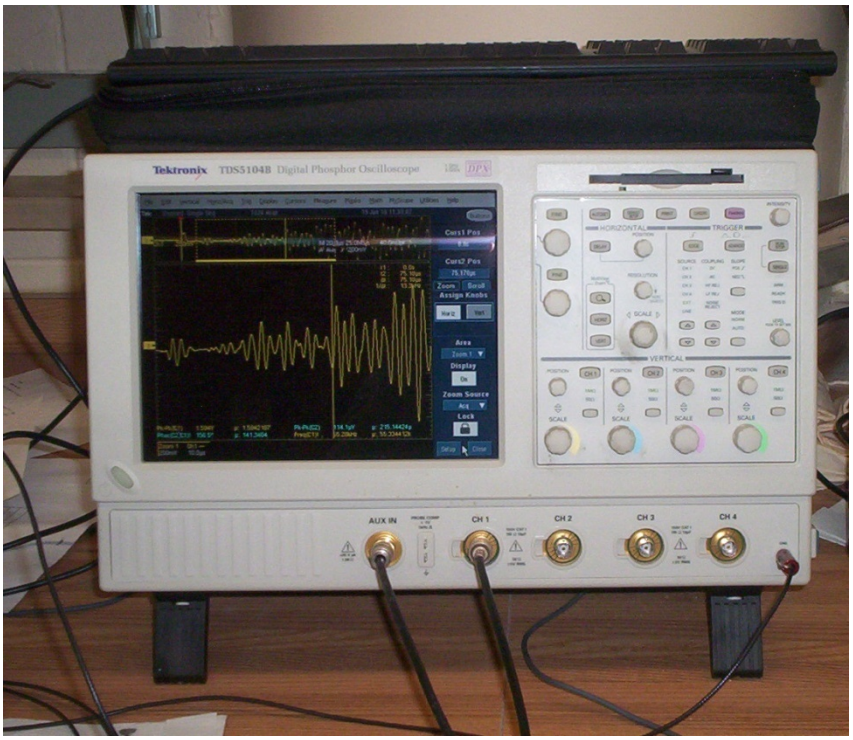

Fig. 3.14. Tektronix TDS5104B Digital Phosphor Oscilloscope.

The sample was loaded into the Carver Laboratory Press with its ends cut flat and covered with a layer of lead foil, but with the wax seal still around its perimeter in order to ensure that the sample remained intact and wet for testing purposes. Ideally, a modest load (one to two metric tonnes) would have been applied to the sample to ensure the ultrasonic wave pulse passing through the sample could be easily and cleanly detected by the receiver platen. However, Sample LP3 was very weak, and even under a very small load, the wax began to deform and water was being squeezed out of the sample. Therefore, a larger load could not be applied. A small load (~0.1 tonne) was applied to the sample, and a pulse was sent from the transmitter and through the sample; fortunately, even at the lower axial load that was used for this test, the signal was detectable by the receiver. The arrival times were interpreted from the waveforms plotted on the oscilloscope. The observed compressional wave arrival time, t_p, was $43.178 \cdot 10^{-6}$ s, and the observed shear wave arrival time, t_s, was $75.178 \cdot 10^{-6}$ s. Results are presented in Table 3.7.

In order to determine the travel times within the sample itself (rather than the travel time through the entire testing system), the system's "zero times" for P and S waves were determined by transmitting and receiving wave pulses with no sample present (i.e., platens separated only by two layers of lead foil). The compressional wave zero time, P_0, was $8.956 \cdot 10^{-6}$ s, and the shear wave zero time, S_0, was $13.996 \cdot 10^{-6}$ s. Results are presented in Table 3.7.

The corrected compressional wave arrival time was calculated as follows:

$$t_{p,corr} = t_p - P_0$$

Similarly, the corrected shear wave arrival time was calculated as follows:

$$t_{s,corr} = t_s - S_0$$

Table 3.7. Measured properties for velocity testing for Sample LP3.

Mass (kg)	$5.335 \cdot 10^{-1}$
Length (m)	$5.7 \cdot 10^{-2}$
Diameter (m)	$7.6 \cdot 10^{-2}$
Volume (m^3)	$2.6 \cdot 10^{-4}$
$\boldsymbol{\rho_b}$ **(kg m^{-3})** *	2059
$\boldsymbol{P_0}$ **(s)**	$8.956 \cdot 10^{-6}$
$\boldsymbol{S_0}$ **(s)**	$13.996 \cdot 10^{-6}$
$\boldsymbol{t_p}$ **(s)**	$43.178 \cdot 10^{-6}$
$\boldsymbol{t_s}$ **(s)**	$75.178 \cdot 10^{-6}$

Remarks:
* ρ_b is the bulk density

Velocities were calculated by dividing the sample length by the corrected arrival times, as follows:

$$V_p = \frac{Sample\ Length}{t_{p,corr}}$$

$$V_s = \frac{Sample\ Length}{t_{s,corr}}$$

Using the compressional wave data as an example, the test parameters used for this calculation are:

Sample Length: $5.7 \cdot 10^{-2}$ m

$$t_{p,corr} = 43.178 \cdot 10^{-6}s - 8.956 \cdot 10^{-6}s$$

$$t_{p,corr} = 34.222 \cdot 10^{-6}s$$

From this, the compressional wave velocity can be calculated as follows:

$$V_p = \frac{5.7 \cdot 10^{-2}m}{34.222 \cdot 10^{-6}s}$$

$$V_p = 1665.6\ {}^{m}/_{s}$$

Analogous results for shear wave arrival time and velocity are included in Table 3.8.

Dynamic Poisson's ratio, υ_d, is calculated from compressional (V_p) and shear (V_s) wave velocities as follows:

$$\upsilon_d = \frac{0.5\left(\frac{V_p}{V_s}\right)^2 - 1}{\left(\frac{V_p}{V_s}\right)^2 - 1}$$

Using the measured and corrected data (see Table 3.8), the dynamic value of Poisson's ratio is:

$$\upsilon_d = \frac{0.50\left(\frac{1665.6}{931.65}\right)^2 - 1.0}{\left(\frac{1665.6}{931.65}\right)^2 - 1.0}$$

$$\upsilon_d = 0.27$$

Dynamic Young's modulus, E_d, is calculated as follows:

$$E_d = {V_p}^2 \rho_b \frac{(1 - 2\upsilon_d)(1 + \upsilon_d)}{(1 - \upsilon_d)}$$

Using the measured and calculated data, the dynamic Young's modulus is:

$$E_d = (1665.6\ {}^{m}/_{s})^2 \left(2059\ {}^{kg}/_{m^3}\right) \frac{(1.0 - 2.0 * 0.27)(1.0 + 0.27)}{(1 - 0.27)}$$

$$E_d = 4.6 \cdot 10^9 Pascals = 4.6\ GPa$$

3.2.9 Comparison between Lab-Measured and Downhole-Measured Velocities

Sample LP3 was taken from a depth of 611.14 m – 611.20 m. The compressional wave interval transit time at this depth, as shown in Fig. 3.5 (f), is approximately 450 μs/m, or $4.5 \cdot 10^{-4}$ s/m. The compressional wave velocity of 1665.6 m/s that was measured in the laboratory ultrasonic tests reported in Table 3.8 corresponds to an interval transit time of $6.00601 \cdot 10^{-4}$ s/m. This is ~33% higher than the values measured in the well log. The difference is likely due to the lack of confining pressure and the low, uniaxial stress condition applied to the sample during the lab test.

Table 3.8. Calculated properties for velocity testing for Sample LP3.

$t_{p,corr}$ (s)	$34.222 \cdot 10^{-6}$
$t_{s,corr}$ (s)	$61.182 \cdot 10^{-5}$
V_p (m/s)	1665.6
V_s (m/s)	931.65
υ_d	0.27
E_d (GPa)	4.6

3.3 Colorado shale from Rocanville, Saskatchewan

3.3.1 Geological Description

The Colorado Group is composed of marine sediments, which consist predominantly of mudstone and claystone (Bloch et al. 1993), and is referred to as the Colorado shale in this thesis. There are also minor amounts of siltstone and fine-grained sandstone (Leckie et al. 2008). The Colorado shale extends from the Rocky Mountains in the west to the Manitoba Escarpment in the east and is up to 1200 m thick in places (Bloch et al. 1993). There is an unconformity between the Colorado shale and the underlying Mannville Group (Bloch et al. 1993). The Milk River and Lea Park formations conformably to disconformably overlie the Colorado shale (Bloch et al. 1993).

See Fig. 3.15(a) and (b) for photos of Colorado shale samples used in this research.

(a) (b)

Fig. 3.15. Sample photos: (a) Sample CS1 (post-testing); (b) Sample CS2 (post-testing).

3.3.2 Optical Microscopy

A 60-mm thin-section was taken from a 75-mm-diameter sample, CS2, perpendicular to bedding. The thin-section was prepared by GR Petrology in Calgary, AB. Jenapol and Leica polarizing microscopes were used in the thin-section analysis.

Thin section analysis indicated that the Colorado shale is "notably laminated, poorly sorted, mid very fine grained argillaceous calclithite" (GR Petrology 2009). The framework is dominated by recrystallized bioclasts (25.0%) and carbonate rock fragments (14.7%). Higher magnification thin section analysis indicated that distinctive plant debris is present in the sample, as well as various carbonate rock fragments.

Results of the thin section analysis are presented in Table 3.9. Selected images are presented in Figs. 3.16 and 3.17.

Table 3.9. Thin section analysis results for sample CS2.

Component	Percentage
Quartz	0.3
Calcite	48.3
Pyrite	2.3
Clay	4.2
Phosphate	9.2
Organic Material	35.6

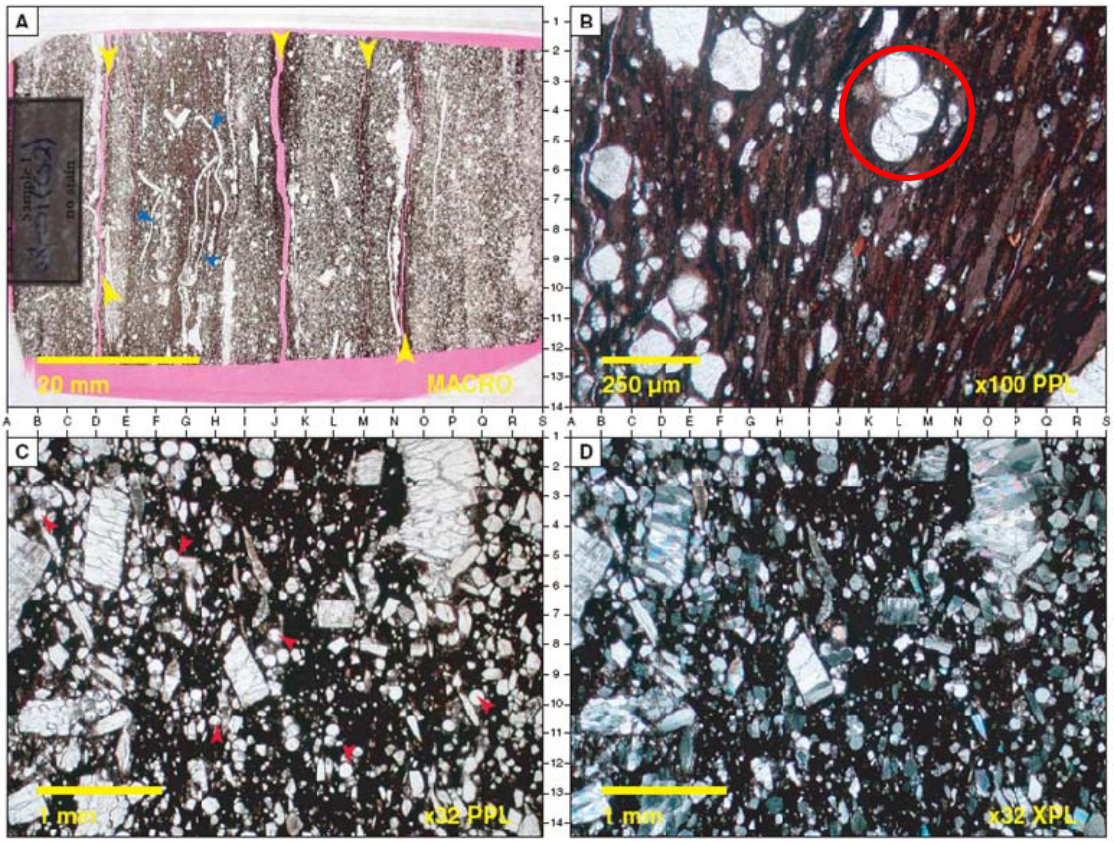

Fig. 3.16. Optical microscopy images for sample CS2. (A) coccoliths and bivalve shell fragments indicated by small blue arrows, and yellow arrows indicate lamina-parallel parting as a result of sample preparation; (B) red circle highlights recrystallized uniserial and triserial forams, and laminated fabric is visible; (C) calcispheres indicated by small red arrows.

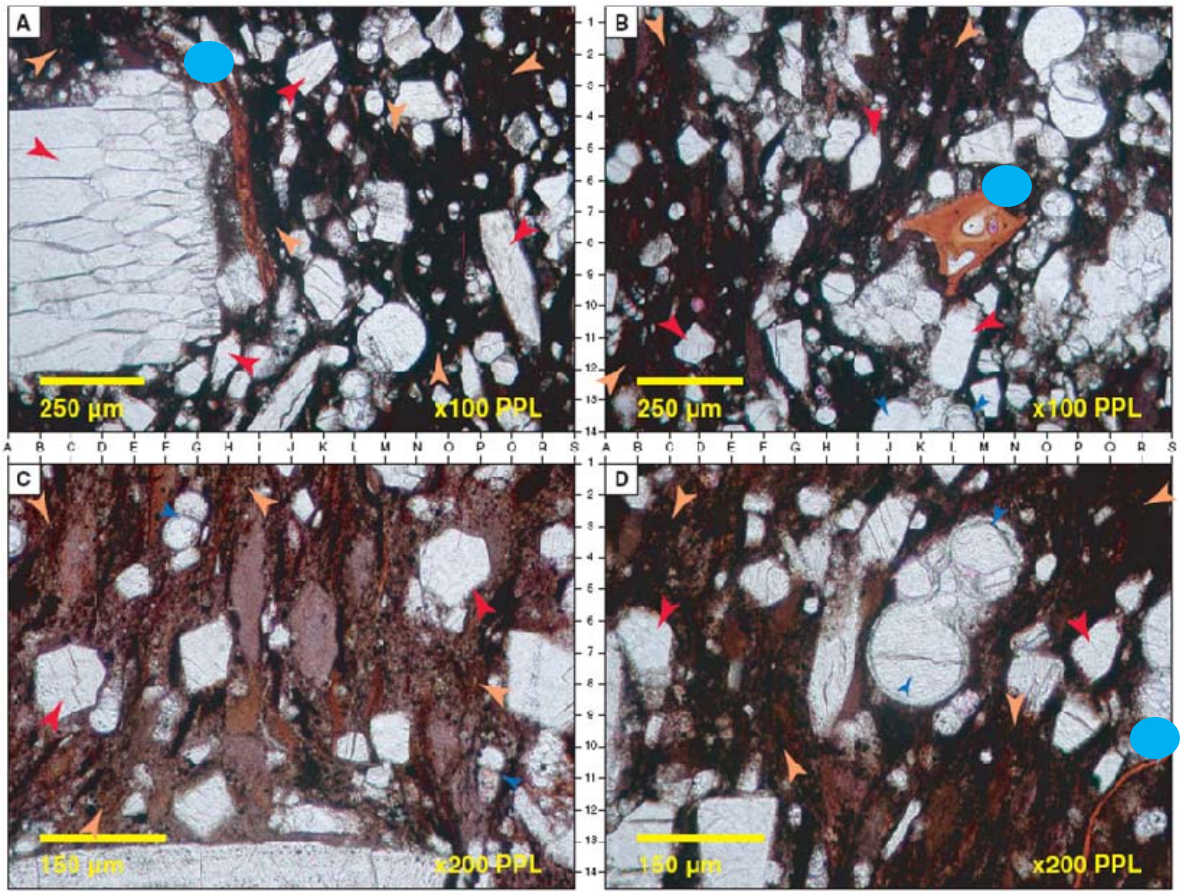

Fig. 3.17. Optical microscopy images for sample CS2, viewed at higher magnification than Fig. 3.18. (A), (B), and (D) plant debris indicated by blue dots; (A) to (D) unidentifiable carbonate rock fragments and recrystallized bioclasts, as well as matrix and pseudomatrix; (B), (C), and (D) small blue arrows indicate chambers of uniserial and triserial forams.

3.3.3 X-Ray Diffraction

X-ray diffraction (XRD) analysis was performed on one sample, CS2, by GR Petrology in Calgary, AB using the same equipment and procedures as described in Section 3.2.3.

XRD analysis determined that calcite makes up the bulk of the sample (89.7%). The clay fraction of the matrix is composed of kaolinite, illite, and smectite.

The results of the XRD analysis are presented in Table 3.10.

The clay fraction was further studied using glycolated clay fraction analysis in order to better distinguish the amounts of each specific clay component within the total clay fraction. This process is described in detail by GR Petrology Consultants Inc. (2009). These results are presented in Table 3.11.

Discrepancies exist between the mineralogy determined from XRD analysis and thin section analysis. XRD analysis does not detect non-crystalline phosphatic material or organic material, which was detected in the thin section analysis. Also, differences between the two could be due to localized variations in the mineralogy of the locations at which the samples were taken. The thin section analysis is likely more representative of the bulk composition of the sample since it samples a larger portion of the sample.

Table 3.10. Bulk XRD results for sample CS2.

Component	Percentage
Quartz	3.4
Plagioclase	0.9
Potassium Feldspar	0.9
Pyrite	1.4
Calcite	89.7
Ankerite	1.3
Kaolinite	1.1
Illite	1.3
Smectite	Present

Table 3.11. Glycolated clay fraction XRD results for the clay fraction for sample CS2.

Component	Percentage
Kaolinite	43.4
Illite	45.9
Smectite	10.7

3.3.4 Scanning Electron Microscopy

Scanning electron microscope (SEM) analyses were performed on sample CS2 by GR Petrology in Calgary, AB using the same procedures and equipment as described for the Lea Park shale in Section 3.2.5. The results indicate that the fabric of the Colorado shale is largely argillaceous. "Variably bitumen-coated clay intermittently admixed with calcimicrite and other fines" are visible (GR Petrology, 2009).

Images from the SEM analysis are presented in Figs. 3.18 and 3.19.

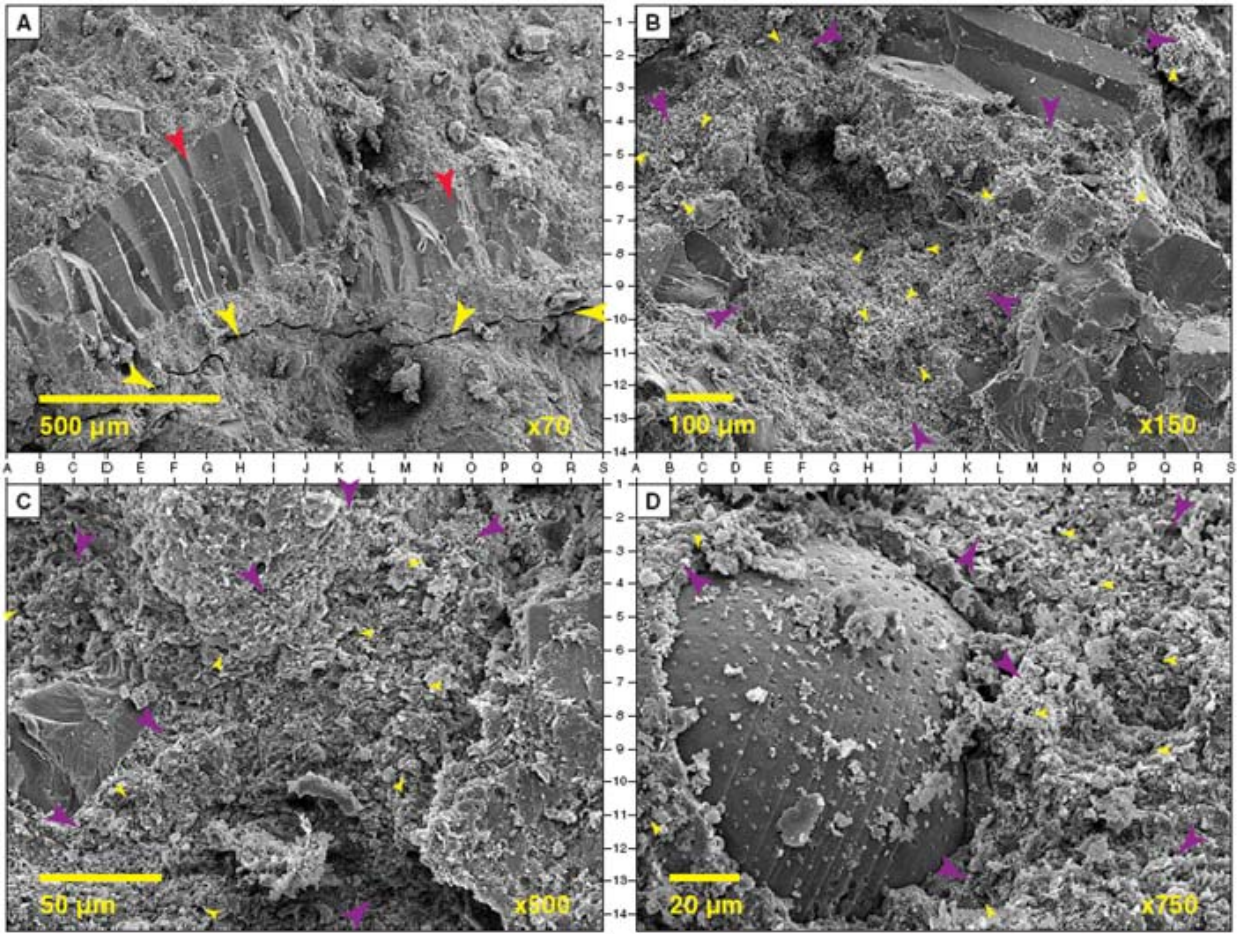

Fig. 3.18. SEM images for sample CS2. (A) red arrows indicate recrystallized carbonate rock fragments, and yellow arrows indicate a microfracture caused by sample preparation; (B), (C), and (D) purple arrows indicate compacted and admixed calcimicrite, clay and other fines, and small yellow arrows indicate microporosity.

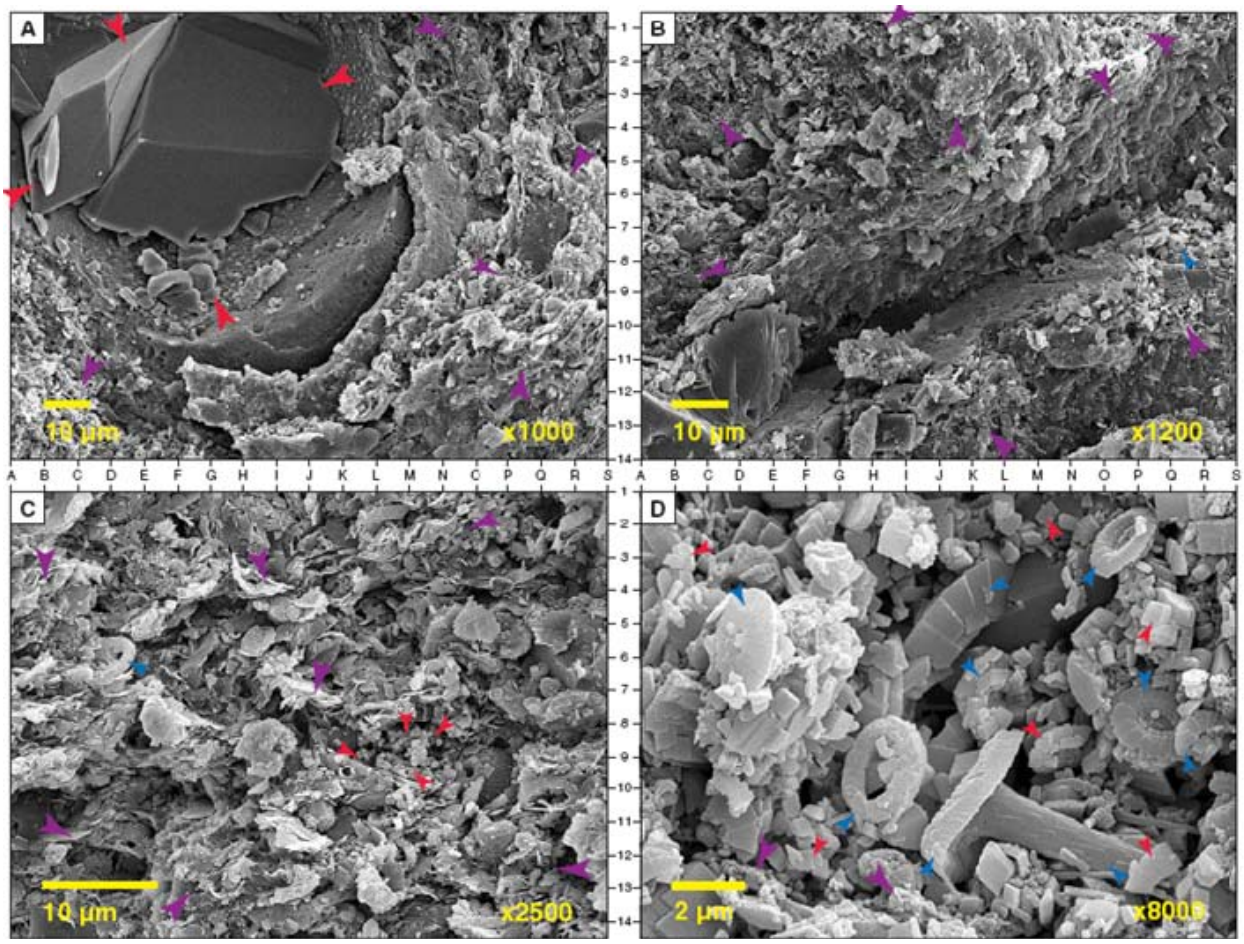

Fig. 3.19. SEM images for sample CS2. (A) red arrows indicate coarser crystalline fabric-replacing calcite, and purple arrow indicate variably bitumen-coated clay intermittently admixed with calcimicrite and other fines; (B) to (D) blue arrows indicate fragments of coccoliths.

3.3.5 Mercury Injection Porosimetry

Mercury injection porosimetry was performed on one sample, CS2, from the Colorado shale, taken from a depth of approximately 429 m, by technical staff at the Department of Physics at the University of Alberta using the same equipment and procedures as described in Section 3.2.6.

Using the results presented in Fig. 3.20 (b) and the same graphical interpretation technique described in Section 3.2.6, the critical pore diameter for Sample CS2 was

calculated to be $1 \cdot 10^{-7}$ m, or 0.1 μm. A summary of the results for this sample is presented in Table 3.12.

Results obtained using the water saturation method (e.g., Fetter 1994) on a sample taken adjacent to sample CS2 indicate that the porosity of these shales is approximately 16%, which is reasonably close to the 14% obtained using mercury porosimetry.

3.3.6 Pore Fluid Analysis

Pore fluid analysis was performed on a 3 mL sample collected from the Colorado shale. The pore fluid was collected by applying a "squeezing" pressure of approximately 55 MPa to several mm^3 of shale in a core holder in the Rock Mechanics Lab at the University of Saskatchewan. The pore fluid was then sent to Isobrine Solutions Inc. in Edmonton, Alberta, where it was analyzed by inductively-coupled plasma mass spectrometry (ICP-MS). ICP-MS is a type of mass spectrometry that is capable of measuring metals and non-metals concentrations below one part in 10^{12}.

The pore fluid results are presented in Table 3.13. The predominant anion is chloride, and the predominant cation is sodium.

(a)

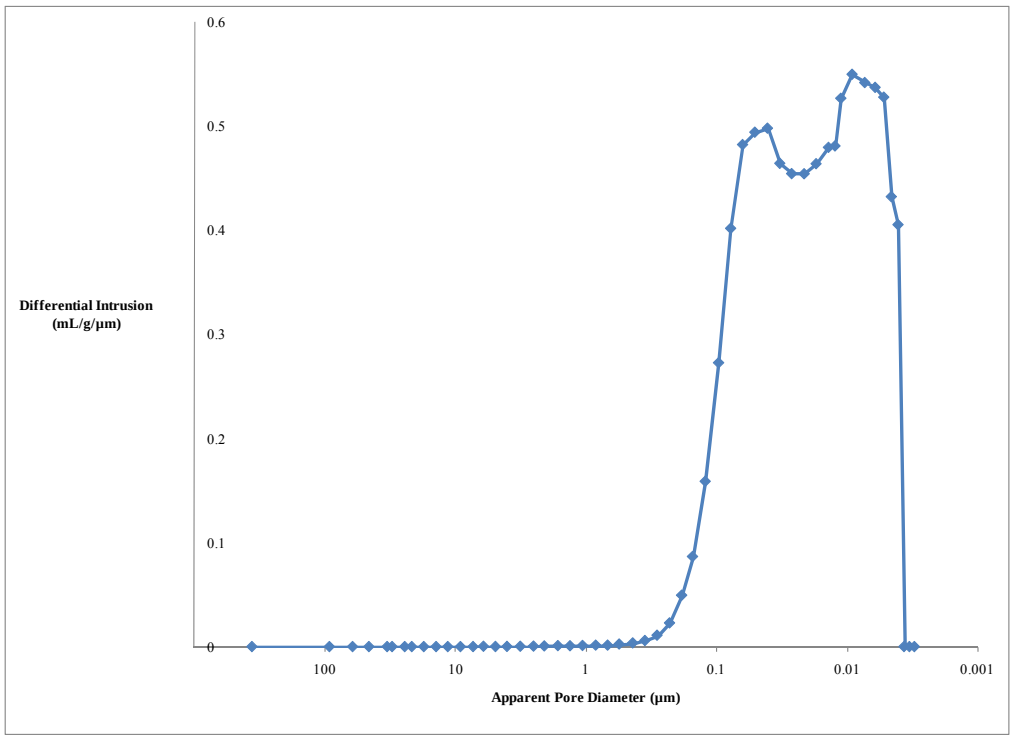

(b)

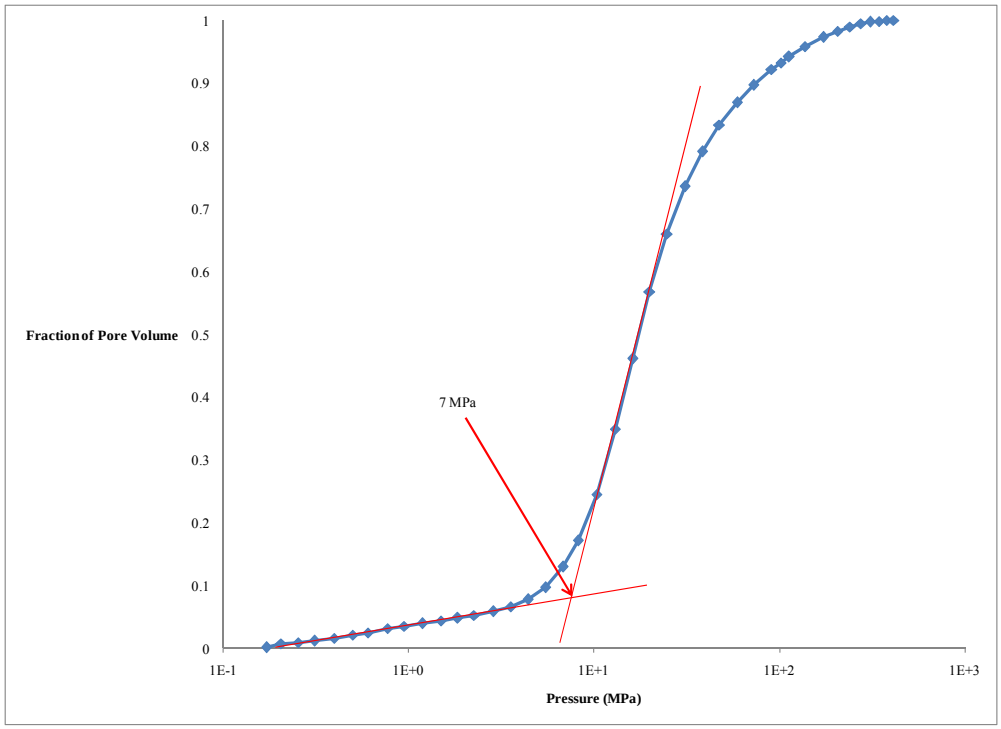

Fig. 3.20. Results of mercury injection porosimetry for sample CS2: (a) differential intrusion; and (b) fraction of pore volume.

Table 3.12. Results of mercury intrusion porosimetry for sample CS2.

	CS2
Critical Pore Diameter (μm)	0.1
Range of Diameters (μm)	0.004 – 7.25
Mean Diameter (μm)	1.005
D_{10} (μm)	0.2
D_{50} (μm)	0.04
D_{90} (μm)	0.01
Porosity	14%

Table 3.13. Pore fluid analysis results for a sample collected from the Colorado shale.

Anions	**F^-**	**Cl^-**	**NO_2^-**	**Br^-**	**NO_3^-**	**PO_4^{---}**	**SO_4^{--}**	**HCO_3^-**
(mg/L)	-	52800	-	95.3	-	-	2807	-

Cations	**Li^+**	**Na^+**	**NH_4^+**	**K^+**	**Mg^{++}**	**Ca^{++}**
(mg/L)	3	27934	-	762	1556	2746

4. EXPERIMENTAL DESIGN AND PROCEDURES

4.1 Overview of Testing System and System Components

This chapter presents the testing system and procedures developed in this research for specialized tests used to assess the sealing properties of aquitards with respect to CO_2. The objective was to conduct the experiments with two-phase pore fluid saturations at pressures of several MPa under applied stresses of the order of tens of MPa, in order to replicate in situ conditions for the Lea Park shale in the Weyburn field. A GCTS RTX-1000 Servo-Controlled Triaxial Rock Testing System (referred to as the "triaxial" throughout this chapter) along with two (initially, and ultimately three) Teledyne-Isco 260D syringe pumps (referred to as "syringe pumps") were used for this purpose (see Figs. 4.1(a) and 4.1(b), respectively). The syringe pumps were connected to the triaxial cell using high-pressure, 1/8" outer-diameter stainless steel tubing, rated for a pressure of 68.9 MPa.

(a) (b)

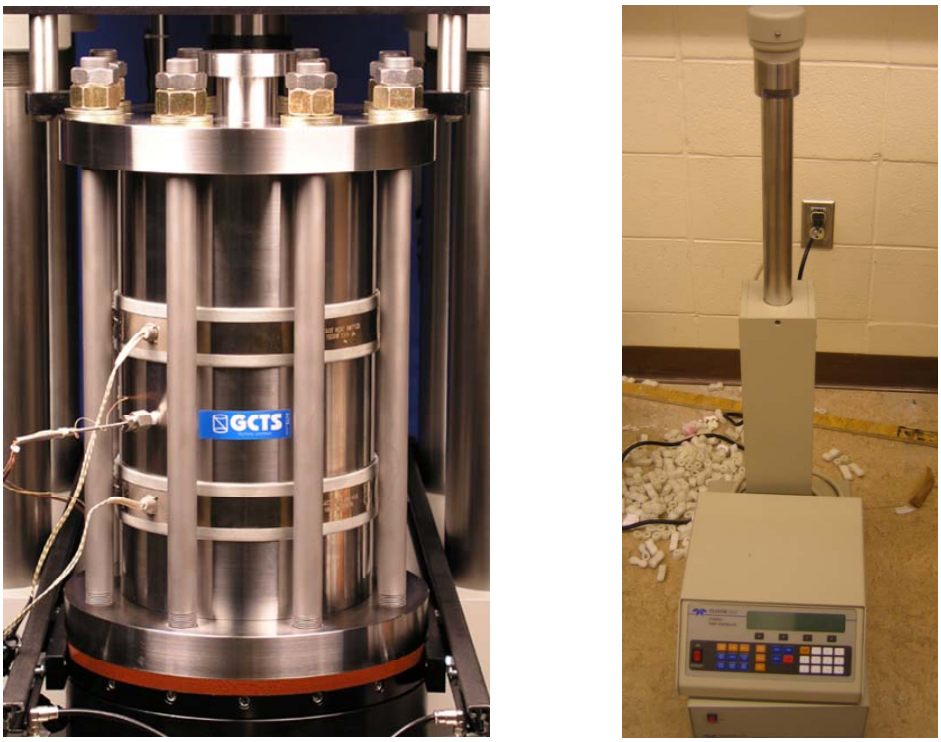

Fig. 4.1. (a) GCTS triaxial apparatus; and (b) Teledyne-Isco syringe pump.

After the sample had been cut to the desired length and the ends ground smooth, it was positioned in the triaxial with a porous disc at each end, and the disc-sample-disc combination was then placed between two platens (an upper and a lower) through which axial load was applied to the sample (Fig. 4.2). In order to apply a lateral confining pressure to the sample, the triaxial cell was filled with hydraulic oil which was then pressurized. A key aspect of the experimental system was the selection of a jacket that would surround the sample, porous discs and platens, and provide a seal that prevented the penetration of the oil into the sample and leakage of pore fluid from one end to the other along the sample-jacket interface.

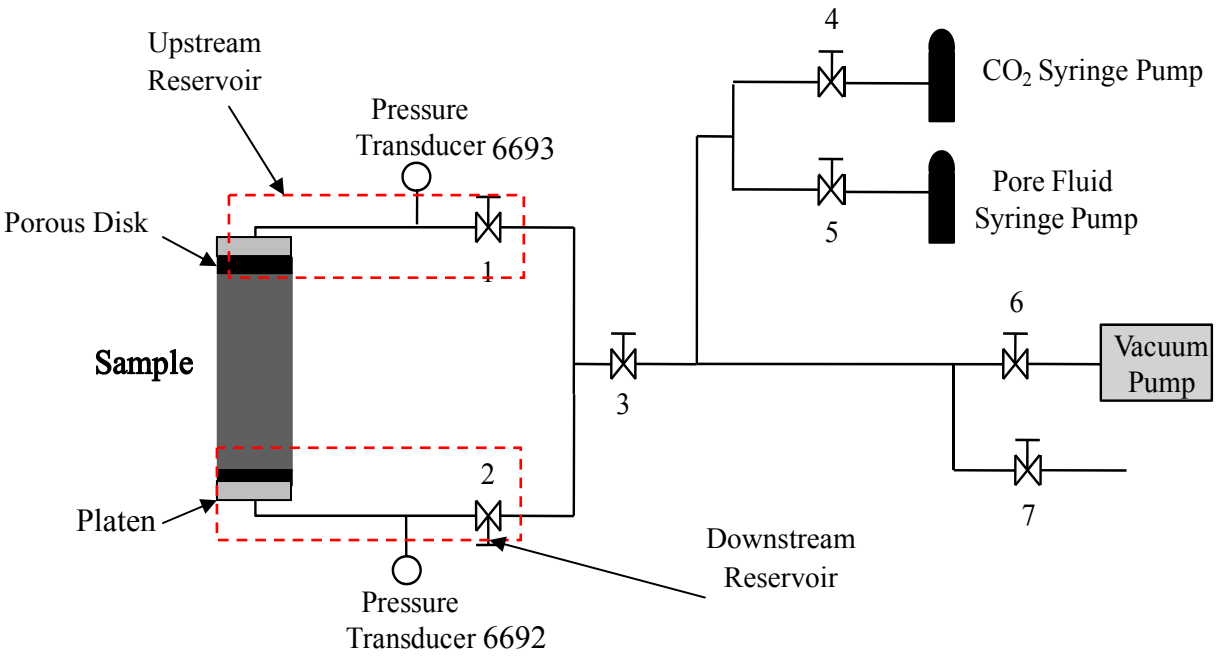

Fig. 4.2. Schematic diagram of the testing apparatus that was ultimately used in this research. [Note: Early tests were conducted in parallel with the troubleshooting described in the following section, during which the equipment configuration and testing procedures underwent a number of changes.]

Options for jacketing the sample include elastomer (e.g., rubber) membranes, or lead foil in combination with copper sleeves. It is thought by some that, in long-term testing, CO_2 can dissolve into elastomer membranes, degrading the membrane and potentially causing it to fail. However, when using lead foil and copper sleeves, one concern is the quality of the seal (e.g., increased potential for leakage of confining oil into the sample, and/or leakage of pore fluid from the upstream reservoir to the downstream reservoir along the sample-jacket interface). Hildenbrand et al. (2004) and Li et al. (2005) recommend using lead foil and copper sleeves, rather than an elastomer membrane, to jacket the sample. Hildenbrand et al. (2004) maintained confining pressures of 10 MPa (or higher) in excess of pore pressures, and Li et al. (2005) maintained confining pressures of 10 MPa, to try to ensure that leakage did not occur.

Based on the experience of the lab technician in the Rock Mechanics Laboratory, a lack of published data demonstrating any problems with SkinFlex III (a transparent urethane elastomer) as a membrane material, and due to acute concerns about the effects of leakage on permeability (and breakthrough pressure) test results on low-permeability samples, SkinFlex III was used in this research. SkinFlex III has two parts, SkinFlex III A and SkinFlex III B. One part of A was mixed with two parts of B, placed in a vacuum chamber to remove air bubbles, and then poured into a mold containing the sample, porous plates, and platens (see Fig. 4.3 (a) and (b)). The SkinFlex III was left to set for approximately 24 hours.

It was decided to use SkinFlex III for the first trial experiment and to make note of any signs of seal degradation. This first experiment lasted approximately three months, the final month of which involved exposure to CO_2. At the end of this experiment, there were no signs of seal degradation upon removal of the sample from the triaxial cell (Fig. 4.4). There was no discolouration, no observable change in texture, and no visible development of flaws. Based on this, SkinFlex III was deemed to be an effective sealing material and was used for the remainder of the experimental program.

(a) (b)

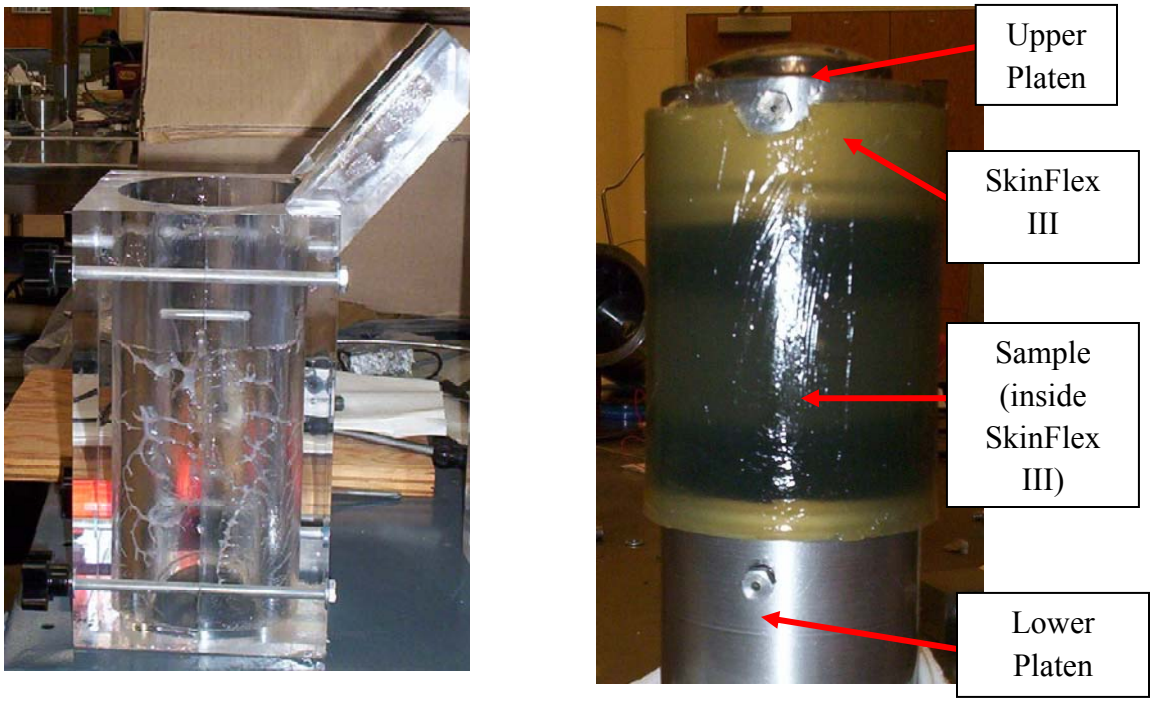

Fig. 4.3: (a) Mold used for pouring SkinFlex III jacket; and (b) sample, porous plates, and platens sealed in SkinFlex III seal.

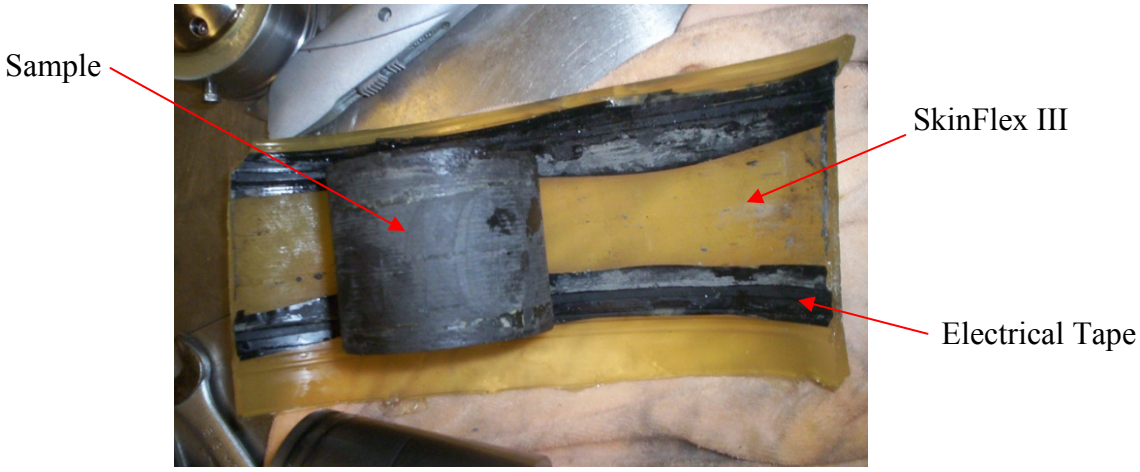

Fig. 4.4. Sample CS1 and its SkinFlex III jacket after three months of testing.

Upstream and downstream "reservoirs" were created by the connection of the stainless steel tubing and associated fittings, flow control and measurement devices to ports on the base of the triaxial, which were internally plumbed so as to allow hydraulic communication with the ends of the sample. Each reservoir consisted of the total volume of void space contained within the following system of components: a sintered stainless steel porous plate, a fluid feed-through channel drilled into a platen and through the base of the triaxial, a high-pressure valve, and the stainless steel tubing connecting the valve to the triaxial. Each reservoir also included a pressure transducer connected to it via a T-junction fitting inserted in-line with the stainless steel tubing. The smaller the total volume of each reservoir, the faster the pressure pulse decay during a permeability test. However, a downside of small reservoir volumes is an acute sensitivity to leakage. Also, as discussed elsewhere in this thesis, the volumes of the upstream and downstream reservoirs relative to the pore volume of the sample play an important role in determining the appropriate approach to interpreting the pulse decay test data.

4.2 Experimental Challenges and Outcomes

Details of the testing procedures ultimately adopted for this work are presented in Section 4.3. Given that these procedures evolved from a series of preliminary tests, during which several challenges were experienced, a review of these challenges is given first: (i) to help the reader appreciate the difficulty of implementing these tests; and (ii) to provide additional insights which should help researchers wishing to implement similar tests in the future.

4.2.1 Acquisition and Assembly of Parts

In the spring of 2008, work in the lab began. Initially, tubing, fittings, pressure transducers, and valves were connected to the GCTS triaxial apparatus and to the Teledyne-Isco syringe pumps. Most of the tubing and fittings were available in the Rock Mechanics Laboratory; however, two high-pressure valves that were required were not available and had to be ordered. Once the valves arrived, the tubing, fittings, pressure

transducers, and valves were put together and connected to the triaxial and to the syringe pumps.

4.2.2 Leak Tests – Air

Once the apparatus was set up and ready to be used, a leak test was performed using an aluminum cylinder as a "sample" to determine if everything was going to work properly. This was done in early September 2008, with air as the fluid. At that time, no leaks were detected. Three leak tests were subsequently performed, all with similar results.

4.2.3 Confining Pressure Application

One of the components of the triaxial is the GCTS HPCP-70 Pressure Control Panel (panel). The panel contains a reservoir, which supplies oil to the triaxial cell, and an air-operated pump, which is manually controlled and is used to apply confining pressure (see Figs. 4.5 and 4.6). Late in the fall of 2008, the air-operated pump stopped working. The pump was taken out and examined. It appeared that small bits (shavings) of metal were getting jammed in the pump's piston. The pump was completely taken apart, cleaned, and reassembled. A few days later, the pump stopped working again. It was taken apart again and the same metal shavings were observed. At this point, it was thought that the parts within the pump were not going to stand up to long-term use.

Another issue with the air-operated pump was the fact that it operates in a cyclical manner, hence it did not maintain a truly constant confining pressure. During sample consolidation and subsequent testing, the confining pressure would fluctuate by up to 2 MPa, which would cause the pore pressures to fluctuate as well. This magnitude of fluctuation in confining pressure was deemed unacceptable, and a decision was made to try applying confining pressure with a syringe pump to see if it would be more stable. The syringe pump was able to maintain reasonably stable confining pressure, and was used to apply confining pressure for the remainder of the experimental program. The panel is now used solely to store the oil in between experiments (within the reservoir) and to fill and drain the oil from the triaxial cell.

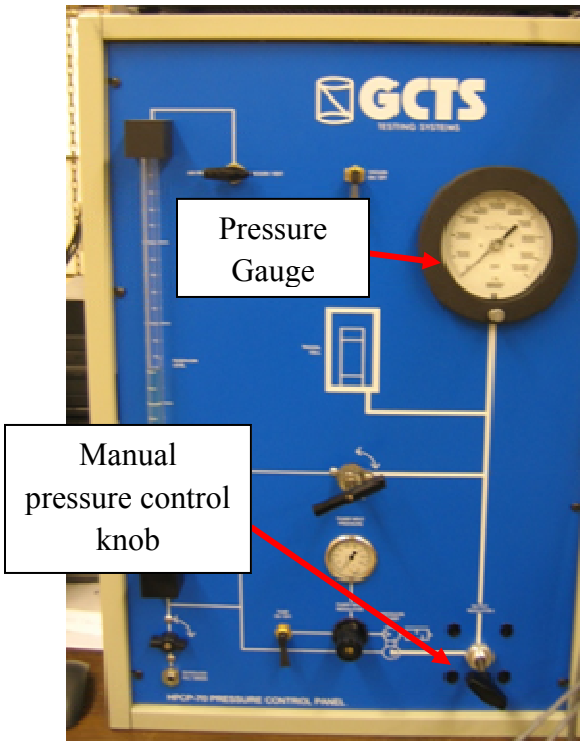

Fig. 4.5. HPCP-70 Pressure Control Panel.

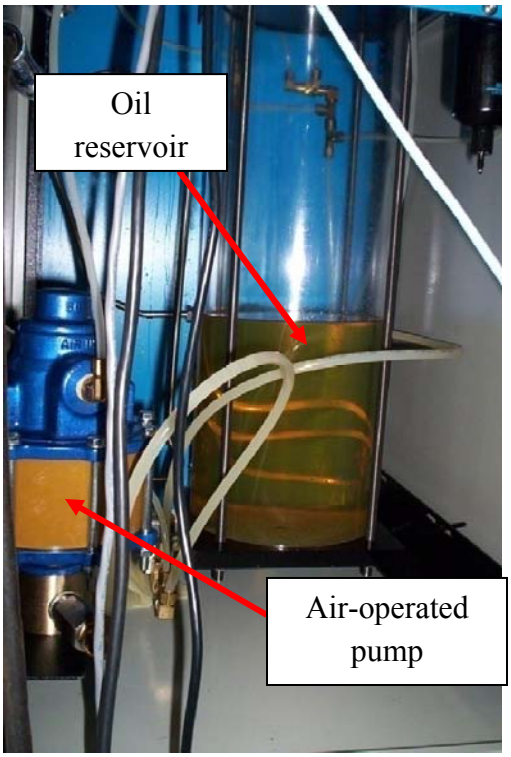

Fig. 4.6. Air-operated pump and oil reservoir.

4.2.4 Initial Experimental Work: Troubleshooting

A sample was cut and prepared for testing (see Appendix A for detailed procedures on sample preparation). Initial "practice" tests were done on samples from the Colorado shale, due to the limited amount of Lea Park shale samples available for this project.

The first sample was loaded into the triaxial, which was subsequently filled with oil, and a small axial stress of approximately 0.1 MPa was applied. (See Appendix A for a detailed description of experimental procedures.) A confining pressure of approximately 0.1 MPa was then applied. Next, the sample was loaded to approximately 13 MPa, the representative in situ stress that was to be used during testing (see Section 4.3.4 for in situ stress state determination). The sample was completely crushed during this loading.

A similar situation occurred with the next sample as well. For the third attempt, smaller incremental axial loads and confining pressures were applied, but this sample was completely crushed as well.

The fourth sample was loaded using very small increments of approximately 0.1 MPa for the confining and axial pressures. Simultaneous application of axial load increments and confining pressure increments was attempted, although perfect synchronization was not possible since the confining pressure was applied manually. This sample also broke at an axial and confining pressure of approximately 7 MPa. However, this sample was not completely broken; it stayed intact within the SkinFlex III sleeve, unlike the other broken samples which were completely crushed.

The data suggested that the samples kept breaking because of the differences in the axial and confining pressures, since they could not be applied simultaneously. Also, the samples were being loaded too quickly; i.e., they were not being given time to consolidate, and the pore pressures were not being allowed to stabilize. It was determined that applying hydrostatic pressure increments to the sample and allowing the pore pressures to stabilize at each increment might alleviate these problems and ultimately lead to a procedure that would result in a sample being successfully loaded to in situ pressures.

Hydrostatically loading the sample proved to be successful and several practice tests were run using this method, which is described in Appendix A. A downside of this approach is the fact that it fails to replicate the in-situ stress state, which is believed to be anisotropic. A significant upside of this approach, in general, is its ease of implementation. Further, in this specific case, it is suggested that the in-situ stress state is not highly anisotropic (see Section 4.3.4).

Another problem that was encountered during the initial experimental work was that the syringe pumps were not able to apply constant pressure over the long-term duration of these tests without leaking. The pump that was being used to supply brine for the permeability testing was developing salt deposits on its piston, due to precipitation of salts from the simulated pore fluid present in the pump. Technical support staff at Teledyne-Isco indicated that these syringe pumps are not meant to supply pressure over longer time periods and that leaks should be expected. A seal was replaced in the hope that this would stop the leak. It appeared to help somewhat but salt deposits continued to develop. However, this leak was deemed to be acceptable, at least for this experimental

procedure, because the syringe pump which contains the brine is used to apply a pressure pulse and can then be shut off, after which a high-pressure valve is used to hold the pressurized brine within the tubing.

Another outcome from the conversation with the Teledyne-Isco technical support was that the syringe pumps are not capable of providing a leak-free supply of pressurized gas. As a result, it was determined that the CO_2 breakthrough pressure testing would have to be conducted with liquid CO_2. CO_2 becomes liquid at approximately 6.2 MPa and 25°C (the temperature at which most of the experiments in this research were conducted). Thus, to facilitate the experimental work, pore pressures had to be maintained at a minimum of 6.2 MPa throughout the experiments. This was well-aligned with the Lea Park testing program, as in-situ pore pressures were estimated to be roughly 5.8 MPa (see Section 4.3.4). As such, it was possible to maintain CO_2 in the liquid state at all times, while only marginally exceeding in-situ pressure.

4.2.5 Permeability and CO_2 Breakthrough Pressure Testing

Using the new method of applying hydrostatic pressure to the samples, two samples of Colorado shale, CS1 and CS2, were successfully tested and their permeabilities and CO_2 breakthrough pressures were determined. Following this, a sample of Lea Park shale, LP1, was also tested.

During consolidation of sample LP1, the uninterruptable power supply (UPS) quit working and the consolidation data was lost. However, once the UPS was fixed, testing continued. Two permeability tests and a CO_2 breakthrough pressure test were completed on sample LP1.

4.2.6 Leak Tests – Brine

In June of 2009, after having completed tests on CS1, CS2, and LP1, in light of difficulties encountered while attempting to test an additional Lea Park shale sample, it was decided that doing another leak test would be a good idea, this time using brine (i.e., pore fluid) rather than air in the upstream and downstream reservoirs. For this leak test, an aluminum plug was loaded into the triaxial, and several tests were run following the

procedures detailed in Appendix A. Initially, it appeared that there was a leak; however, it was not known if the leak was located within the section of tubing that is critical during testing (i.e., within one of the sections that constitutes a "reservoir"), or if it was outside of the critical testing region (i.e., between valves 1 and 2). As a result, additional leak tests were performed, in which different sections of tubing (and associated fittings) were isolated and tested.

During this leak test, it appeared that the fluctuating ambient temperature in the Rock Mechanics Lab was contributing to pore pressure fluctuations within the tubing; i.e., there may not have been a leak at all but rather a pore pressure response to changes in temperature. For example, when the room temperature dropped, the pore pressures did as well, but not at the same time, and it took much longer for the pore pressures to increase once the room temperature had increased. Several attempts were made to monitor the temperature to determine if the drops in pore pressure were due to temperature fluctuations or not.

During this time, the UPS once again stopped working. Once the UPS was replaced, the GCTS SCON 2000, the control box that allows communication between the triaxial and the PC, no longer worked. The GCTS SCON 2000 did not recognize that the PC was connected to it. Without this critical communication, no testing could be done because all experimental monitoring and data acquisition is implemented through the PC.

Approximately three weeks of communication with technical support at GCTS resulted in the eventual solution to the problem. The ribbon cable that connected the port on the back of the GCTS SCON 2000 to the computer inside the GCTS SCON 2000 was not working. The PC was subsequently plugged directly into the computer inside the GCTS SCON 2000 and, after this, there was once again communication between the GCTS SCON 2000 and the PC.

Once the PC and the triaxial could communicate again, the search for the source of the leak continued. The stainless steel tubing was wrapped in foam insulation and the entire apparatus was surrounded with heavy plastic curtains. A small electric heater connected

to a temperature controller was set to maintain a temperature of approximately 25°C within the curtains, and a small fan was used to circulate the air.

Another leak test was performed with this temperature control system in place. The pressure differential across the aluminum plug was approximately 7 MPa (1000 psi). It was thought that this was likely too high and was putting too much stress on the system so it was reduced to approximately 0.7 MPa (100 psi); i.e., a pressure drop closer in magnitude to the values actually used during permeability testing. Under both of these situations, the pore pressures dropped; i.e., there was a leak somewhere in the system. On closer examination, salt deposits could be seen at some of the fittings (where the tubing entered a valve or a T-section, etc.), so these were replaced, and another leak test was performed with a pressure differential of 1 MPa (145 psi). After approximately 24 hours, the pore pressures were approximately stable and the problem of the leak was solved; i.e., it appears that some of the fittings had developed leaks over the course of time (presumably after the completion of tests on CS1, CS2, and LP1, as there had been no indications of leakage during those tests).

4.2.7 Sample Preparation

Both the Colorado shale and Lea Park shale samples are extremely fragile, which makes them both difficult and challenging to work with. Cutting them with a traditional rock saw (see Fig. 4.7) did not work because the saw damaged the cut surface of the sample, rendering it useless for the purposes of these experiments (see Fig. 4.8). Instead, an automatic rock saw was used, which took approximately 30 minutes to cut through the samples used for this testing program (see Fig. 4.9).

The sample was placed into the holding apparatus and "secured" in place by tightening a screw against a board that is flush with the side of the sample (see Fig. 4.10). However, it could not be secured too tightly because the sample might break; therefore, the screw was tightened just enough to prevent the sample from moving while being cut, but not so much that the sample would break. The saw then was then moved very slowly through the sample. Water was used throughout the cutting process to keep the blade cool. This also prevented drying out of the exposed sample surface. The cutting process had to be

monitored to ensure that the saw did not cut all the way through the wax around the sample. If this happened, the cut sample would fall away from the remaining core, which could damage the fragile sample, and the water would erode the cut surface of the sample. Therefore, the cut sample was left attached to the remaining length of core, and the final, intact thickness of wax was subsequently cut through with a knife.

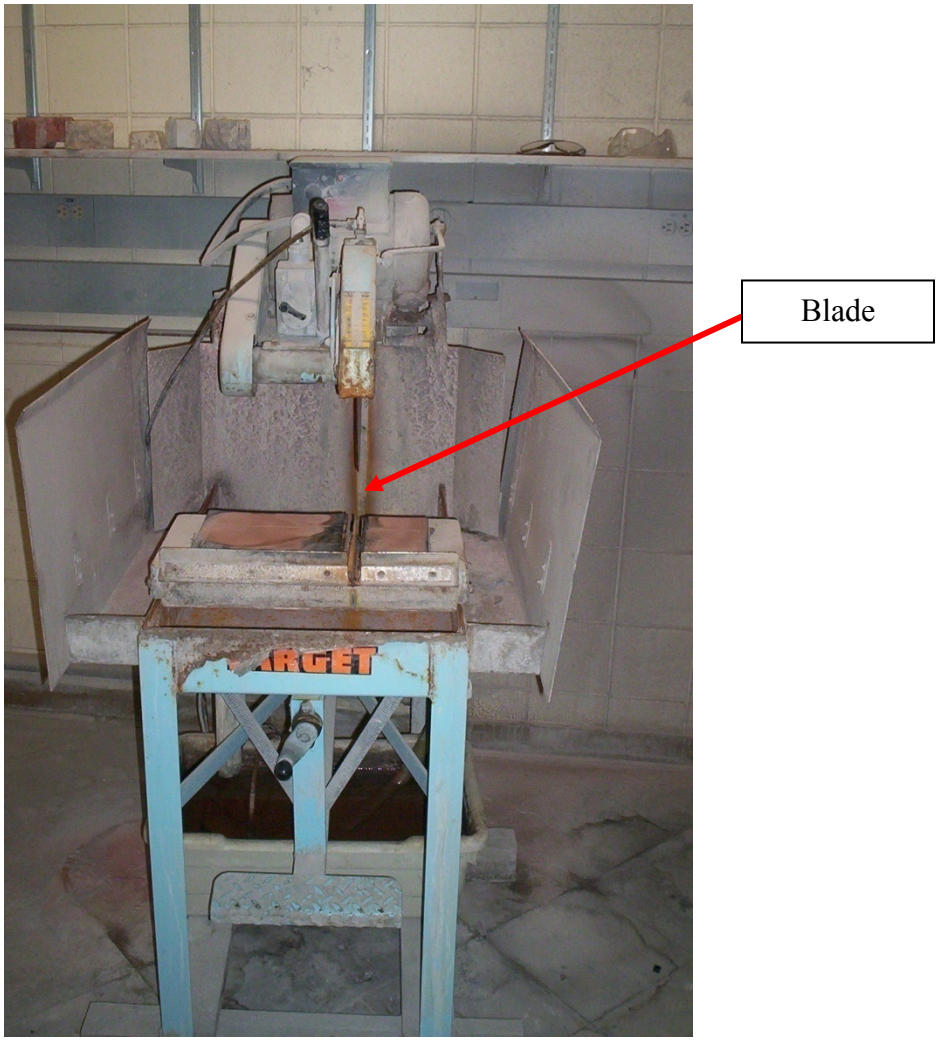

Fig. 4.7. Traditional rock saw.

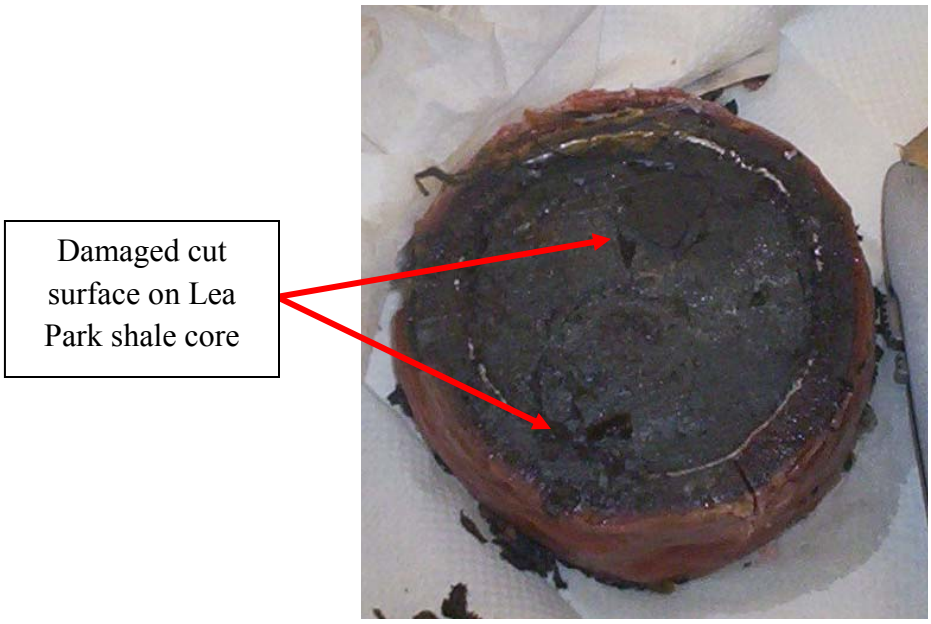

Fig. 4.8. Lea Park shale core showing the damaged cut surface.

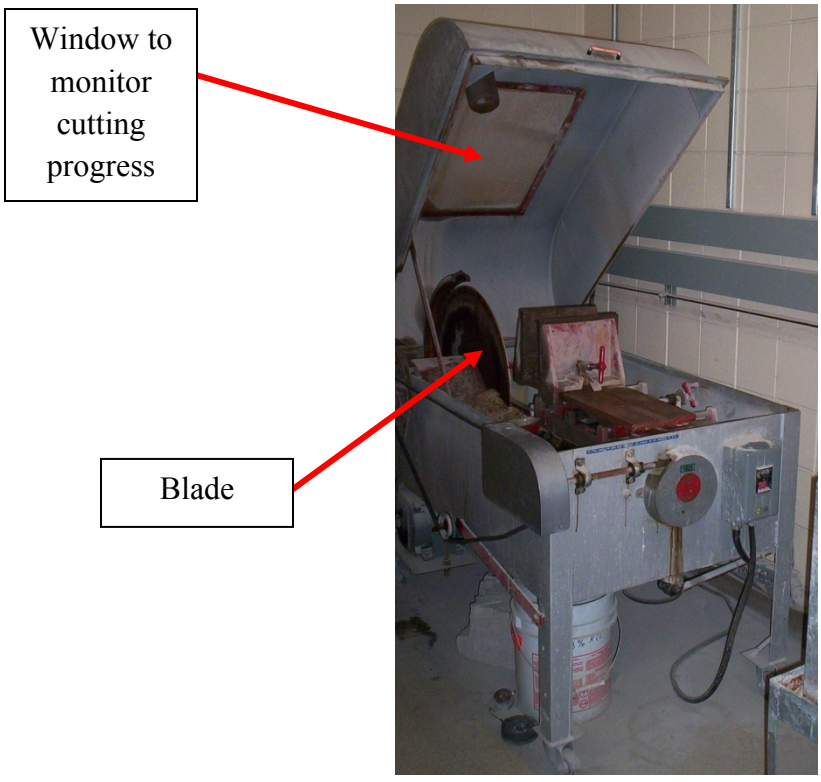

Fig. 4.9. Automatic rock saw.

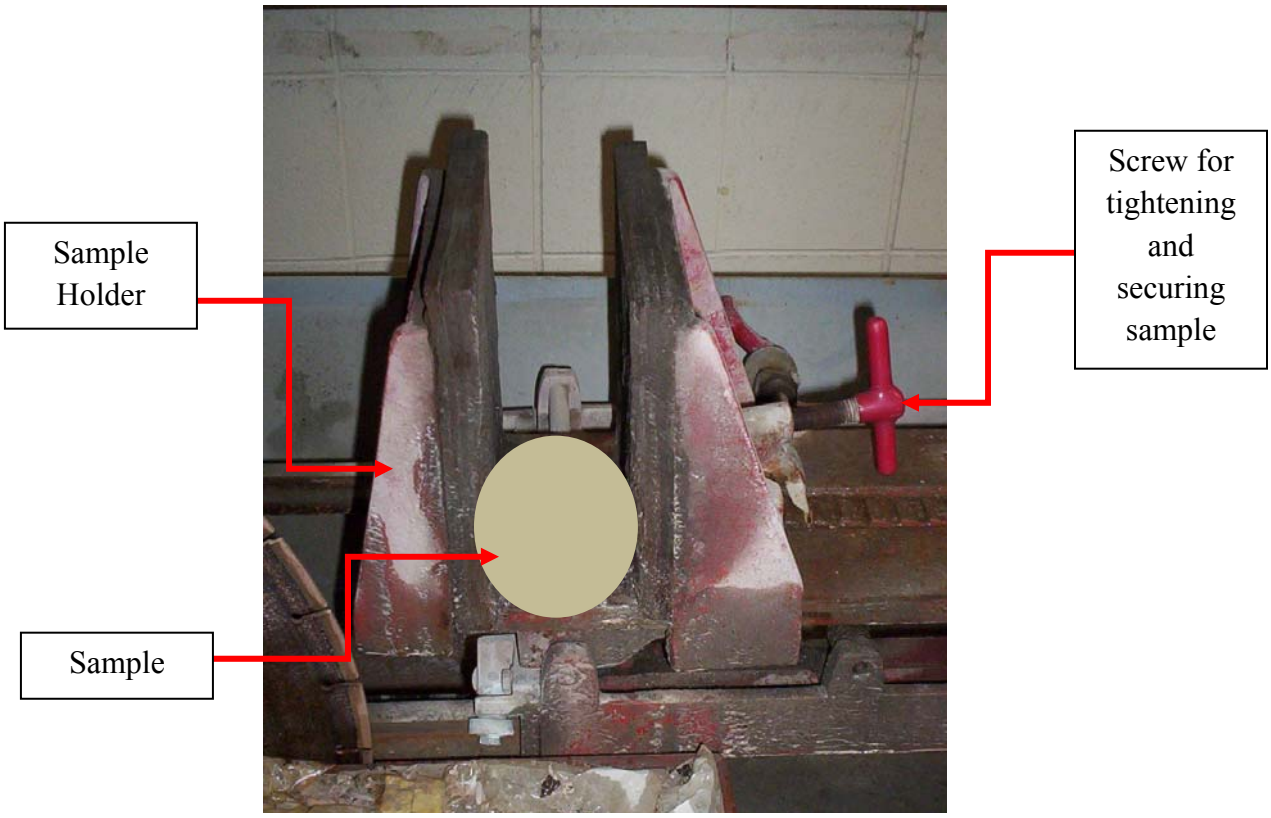

Fig. 4.10. Sample holder in the automatic rock saw.

Once the sample had been successfully cut from the longer length of core, the wax, aluminum foil, and plastic wrap had to be removed. This also had to be done with great caution, or else the sample would fall apart once the wrapping was removed. First, the wax was carefully sliced lengthwise down the side of the sample, using caution to ensure that the sample itself was not cut. Once the wax was cut, it was slowly peeled away from the sample, again using extreme caution. The aluminum foil and plastic wrap could then be removed very slowly and with caution. Once these wrappings were completely removed from the sample, an assessment was made as to its suitability for testing purposes. In some cases, a potential sample had intact, smooth ends but the middle section was broken up and crumbly, or that the sample simply fell apart (see Fig. 4.11).

The final Lea Park shale sample used for permeability and CO_2 breakthrough pressure testing (Sample LP2) took over two days to obtain. Several attempts were made to cut a

sample from the middle section of core, which came from a depth between 604.40 m and 604.75 m. Each piece that was cut either crumbled while still in the wax or fell apart once the wax was removed (see Fig. 4.11). The entire section of core was unusable. The sample was finally cut from the bottom section of the preserved core, which came from a depth between 610.90 m and 611.20 m. This sample, LP2, was successfully unwrapped and sealed in SkinFlex III, and was placed into the triaxial.

Fig. 4.11. Broken piece of Lea Park shale core sample.

4.3 Experimental Procedures

4.3.1 Apparatus

The testing system configuration that was ultimately used is shown in Fig. 4.2. Some notes of relevance with respect to the system components are as follows:

- Pressure transducers 6692 and 6693 have maximum values of 10.3 MPa (1500 psi)
- Valves 1 and 2 are high-pressure HiP valves rated for pressures of 103 MPa (15,000 psi)
- Upstream reservoir consists of porous disk, platen, tubing, pressure transducer 6693, and valve 1.
- Downstream reservoir consists of porous disk, platen, tubing, pressure transducer 6692, and valve 2.

4.3.2 Pore Fluid

As previously mentioned, a pore fluid sample was collected from a sample of Colorado shale (see Table 3.13). However, the pore fluid analysis results were not obtained until testing had already begun. As such, the pore fluid composition previously obtained for the Lea Park shale by Ting-Kai Chan (see Section 3.2.7.3, Table 3.8) was used as the basis for a synthetic pore fluid used for all tests conducted during this research. Staff in the Environmental Lab at the University of Saskatchewan recreated this solution, and its composition is presented in Table 4.1.

Table 4.1. Composition of synthetic pore fluid used for experimental program.

Compound	**$CaCl_2$**	**NaCl**	**Na_2SO_4**	**$NaHCO_3$**	**KCl**	**$MgSO_4$**
(mg/L)	122.2	2,870.7	3,849.1	216.7	16.8	31.0

4.3.3 Measurement of Reservoir Compressive Storage

In order to determine permeability using equation 2.1, the compressive storage of the upstream and downstream reservoirs must be determined. Conceptually, compressive storage is a term that describes how a reservoir's pressure changes in relation to an influx (or withdrawal) of a given volume of fluid (though, strictly speaking, this parameter is parameterized as the reciprocal of this relationship; i.e., $\Delta V/\Delta P$).

For the compressive storage testing done in this research, an impermeable sample (i.e., an aluminum plug) was sealed in SkinFlex III and placed into the triaxial. Valves 4, 6, and 7 remained closed throughout compressive storage testing, and all lines were saturated with synthetic pore water. To determine the compressive storage of the upstream reservoir, valve 2 was closed and valves 1, 3, and 5 were opened. Pressure was increased using the pore fluid syringe pump, while monitoring the change in volume in the pump. This was completed over a pressure range of 2 MPa to 5 MPa. Subsequently, valve 1 was closed and the same process repeated. This was done to isolate the upstream reservoir, since it was not possible to directly determine its compressive storage. In other words, the compressive storage of the entire section from the porous disk to the pore fluid syringe pump was first determined. Then, the compressive storage of the section from valve 1 to the pore fluid syringe pump was determined. The difference between these two compressive storages was then taken as the compressive storage of the upstream reservoir.

The same procedure was followed to determine the compressive storage of the downstream reservoir, except that valve 1 remained closed and valve 2 was used. The results for the upstream reservoir are presented in Fig. 4.13. The results for the downstream reservoir are presented in Fig. 4.14.

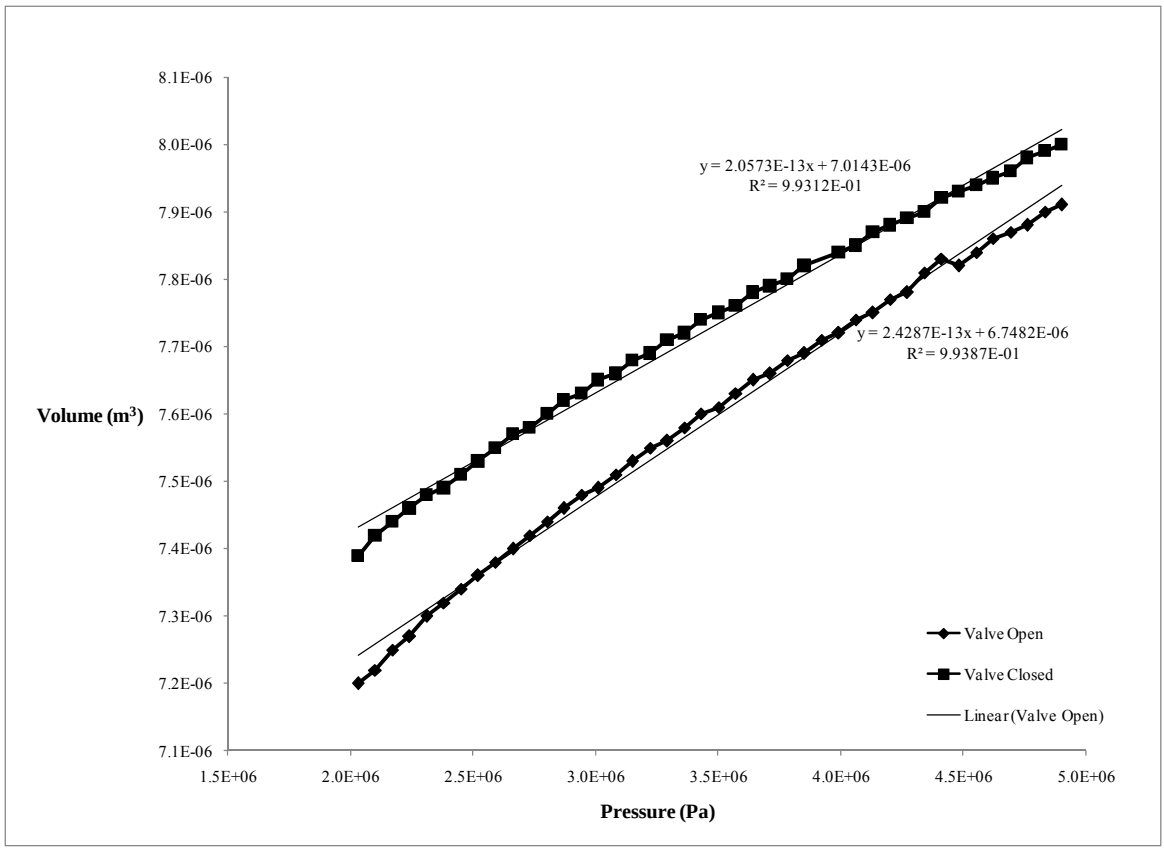

Fig. 4.13. Compressive storage results for the upstream reservoir.

The compressive storage of each reservoir was determined by taking the difference between the slopes shown in Figs. 4.13 and 4.14. The results indicate that the compressive storage of the upstream reservoir, S_u, and the downstream reservoir, S_d, were $1.0 \cdot 10^{-13}$ $m^3 \cdot Pa^{-1}$ and $4 \cdot 10^{-14}$ $m^3 \cdot Pa^{-1}$, respectively.

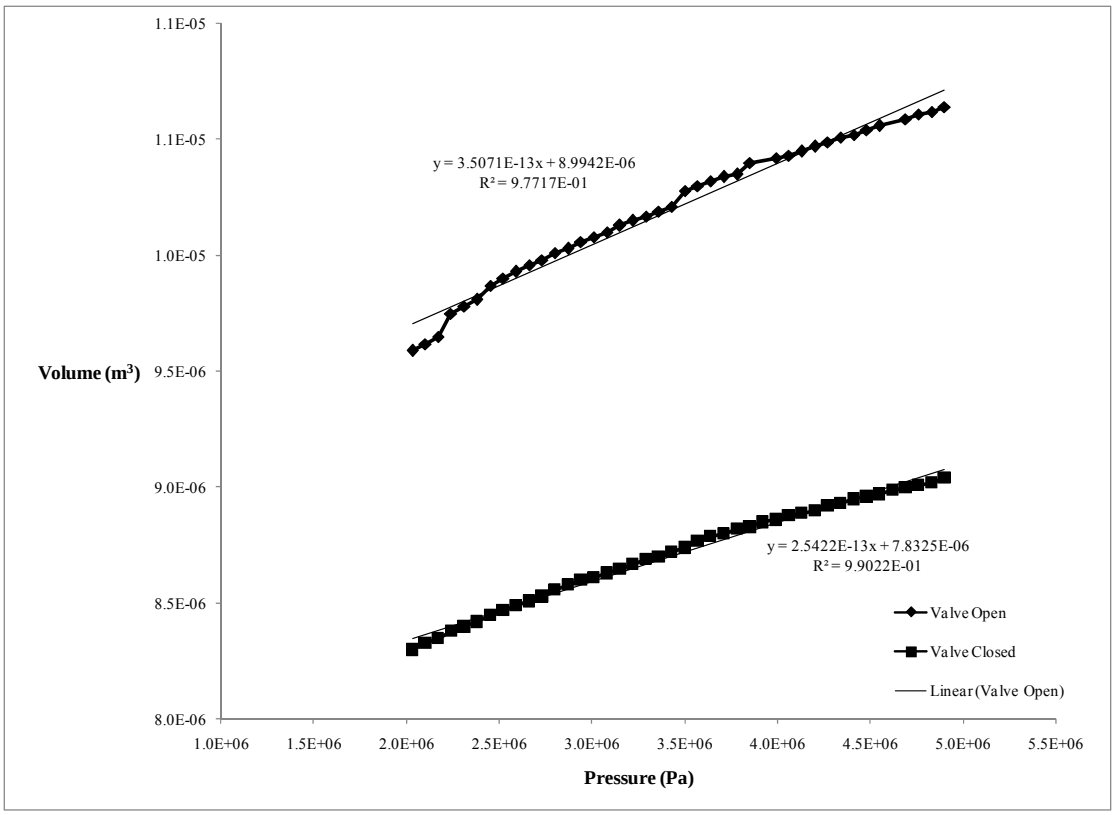

Fig. 4.14. Compressive storage results for the downstream reservoir.

4.3.4 In-Situ Stress State

The vertical stress, σ_v, in the Lea Park shale in the Weyburn area is determined from the following

$$\sigma_v = z \cdot \rho_b \cdot g \qquad [4.1]$$

where z is depth [m], ρ_b is the average bulk density of overlying strata [kg·m^{-3}], and g is gravitational acceleration [m·s^{-2}].

The parameters for this equation are:

z: 600 m

ρ_b: 2200 kg·m^{-3} (determined from geophysical logs)

g: 9.81 m·s^{-2}

From this, the vertical stress was calculated as follows:

$$\sigma_v = 600m \cdot 2200\frac{kg}{m^3} \cdot 9.81\frac{m}{s^2}$$

giving a vertical stress of:

$$\sigma_v = 13 \cdot 10^6 Pa = 13\ MPa$$

An assessment of average horizontal stress magnitude was made using data from a well near Regina, SK, as reported by Bell et al. (1994). These data, which are summarized in Table 4.2, indicate that the ratio between the average horizontal and vertical stresses is approximately 0.8. Given that these measurements were made at the base of the Williston Basin's sedimentary succession, further to the Cretaceous-age clastics that overlie the Lea Park shale, the overlying strata included lower Mesozoic clastics and carbonates and Paleozoic carbonates. As a consequence, the average density of the overlying strata (hence the magnitude of the vertical stress gradient) was nearly 15% higher at the Regina well. In spite of this higher vertical stress gradient, it was assumed for this research that the horizontal:vertical stress ratio of 0.8 was also a reasonable estimate for the Lea Park shale at the Weyburn field, for lack of data suggesting otherwise.

If it had proven possible to apply a triaxial stress state on the Lea Park shale test samples, an axial stress of 13 MPa and a lateral (confining) stress of 10.4 MPa (0.8·13) would have been used. However, given that it ultimately proved necessary to conduct these tests under hydrostatic confinement, a confining pressure equivalent to the vertical stress (13 MPa) was used. Though from a different site and different depths, the same 13 MPa confining pressure was used for the Colorado shale samples in order to enable direct comparison of test results for these two different stratigraphic units.

No direct measurements of pore pressure are available for the Lea Park shale in the Weyburn Field. In a Weyburn well drilled in 1955 (unique well identifier 01/02-28-006-13W2/0) a drill-stem test was conducted in the Viking Formation, which is an aquifer located at the base of the Colorado Aquitard. In-situ pore pressure (estimated from the final shut-in pressure) was 8.205 MPa, at a test interval from 846.4 to 855.0 m depth.

Assuming a fresh-water density of 1000 kg/m^3, this corresponds to a hydraulic head of 836.4 m. Compared against the test-interval's mid-point depth of 850.7 m, this suggests a piezometric surface that is 14.3 m below ground level. Assuming that the same density and piezometric surface are appropriate for the Lea Park shale, pore pressure (P) in this shale at a depth of 600 m was calculated as follows:

$$P = (600 - 14.3)m \cdot 1000\frac{kg}{m^3} \cdot 9.81\frac{m}{s^2}$$

giving a pore pressure of:

$$P = 5.8 \cdot 10^6 Pa = 5.8\ MPa$$

Rounding this figure off to 6 MPa, the resulting pressure differential between the approximated, average in-situ stress (13 MPa) and the in-situ pore pressure is therefore 7 MPa. Since it was experimentally desirable to conduct the CO_2 breakthrough pressure with liquid CO_2, as explained in Section 4.2.4, it was necessary to maintain pore pressures at a minimum of 6.2 MPa. To ensure that the CO_2 stayed in liquid form, pore pressures were maintained at roughly 7.5 MPa; confining pressures were maintained at levels roughly 7 MPa greater than the pore fluid pressure (i.e., roughly 14.5 MPa).

Table 4.2. In-Situ Stresses reported by Bell et al. (1994) at depths ranging from 2065 m to 2213 m.

	Well Location: 3-8-12-12-W2			
	Vertical Stress (MPa)	Minimum Horizontal Stress (MPa)	Maximum Horizontal Stress (MPa)	Ratio of Average Horizontal Stress to Average Vertical Stress
	51.6	35.7	40.7	0.8
	54.2	40.1	55.3	
	55.3	41.1	52.8	
Average	54	44		

4.3.5 Vacuum Application

Once the sample had been loaded into the triaxial, a vacuum was applied to the system to remove any air from the tubing. This was done by opening valves 1, 2, 3, and 6, and closing valves 4, 5, and 7 (Fig. 4.2). The vacuum was applied for approximately 15 minutes, at which time valve 6 was closed. Valve 5 was then opened and brine injected into the system using the pore fluid syringe pump at a low initial pressure of approximately 0.5 MPa.

4.3.6 Consolidation

Prior to doing any kind of flow testing on the shale samples, they had to consolidate, while ultimately achieving the target pore pressure and confining pressure. This was done by increasing the confining pressure in 0.5 MPa increments. The pore pressures were allowed to stabilize over a period of approximately 24 hours before the next confining pressure increment was applied. This was done until the target confining pressure of 14.5 MPa was reached. Once the 14.5 MPa confining pressure was reached, the sample was left to consolidate until the pore pressures stabilized to approximately 7.5 MPa. The procedures required to achieve this 7.5 MPa target are described in the following paragraph.

During consolidation, valves 3, 4, 5, 6, and 7 were closed while valves 1 and 2 (see Fig. 4.2) initially remained open. Once pore pressures reached values in excess of the target value of 7.5 MPa, pore fluid was bled off to allow the sample to continue to consolidate. This was done by completely opening valve 7 and by slowly opening valve 3. Early on in the sequence of bleed-off cycles, the pore pressures were relatively high and would rebound quickly once the valve had been opened then closed again. During these early cycles, it was acceptable to fully open valve 3 (before closing again) during each bleed-off cycle. However, as consolidation progressed, the pore pressures took longer to rebound; hence valve 3 had to be opened with more caution. Turning it slowly and continuously allowed the user to feel the valve just begin to open. Once the pore pressures appeared to be stabilizing, valves 1 and 2 could be closed; however, this could not be done all at once as this created a mini-pressure pulse, after which additional time

was required for re-stabilization. Closing each valve one to two half-turns per day helped to eliminate this problem.

Figs. 4.15 and 4.16 present confining pressure and pore pressure consolidation data, respectively, for Sample LP2. This consolidation behavior is fairly typical of the consolidation of samples CS1, CS2, and LP1. From these figures, it can be seen that consolidation can take a month or more (in this case, over 35 days).

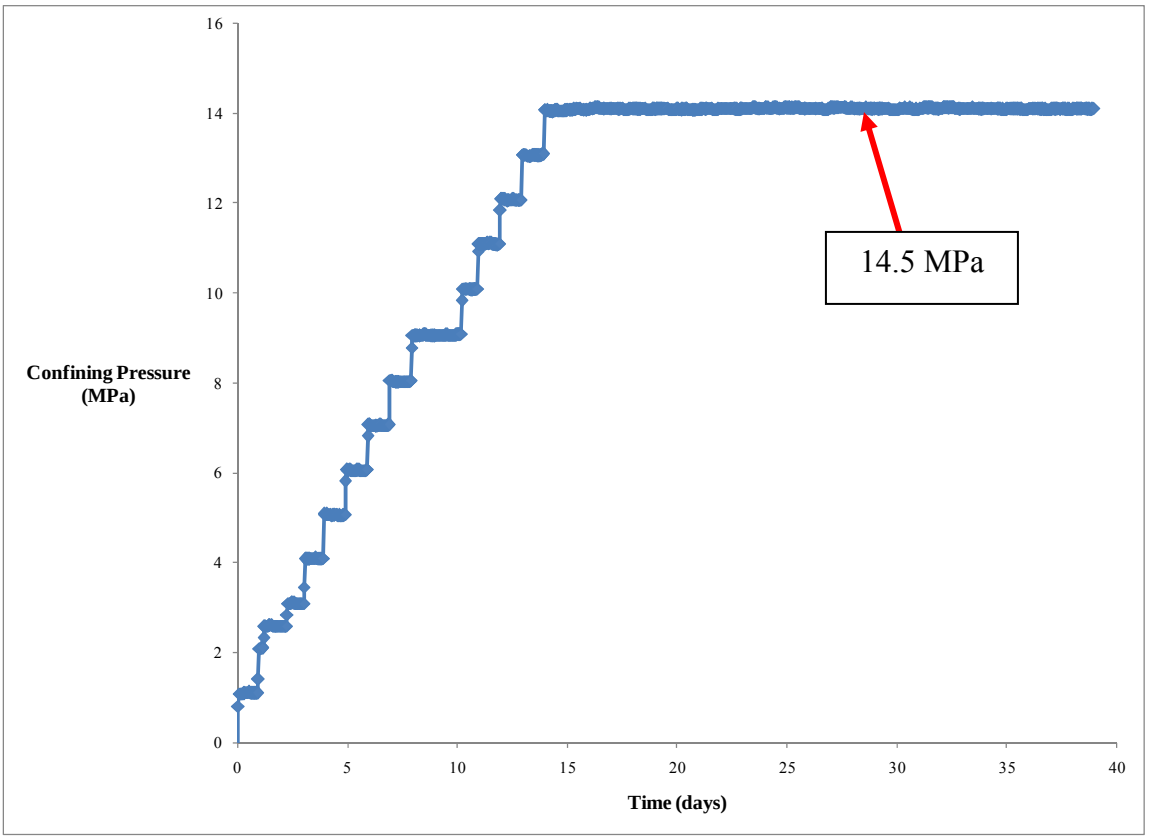

Fig. 4.15. Confining pressure during consolidation of Sample LP2.

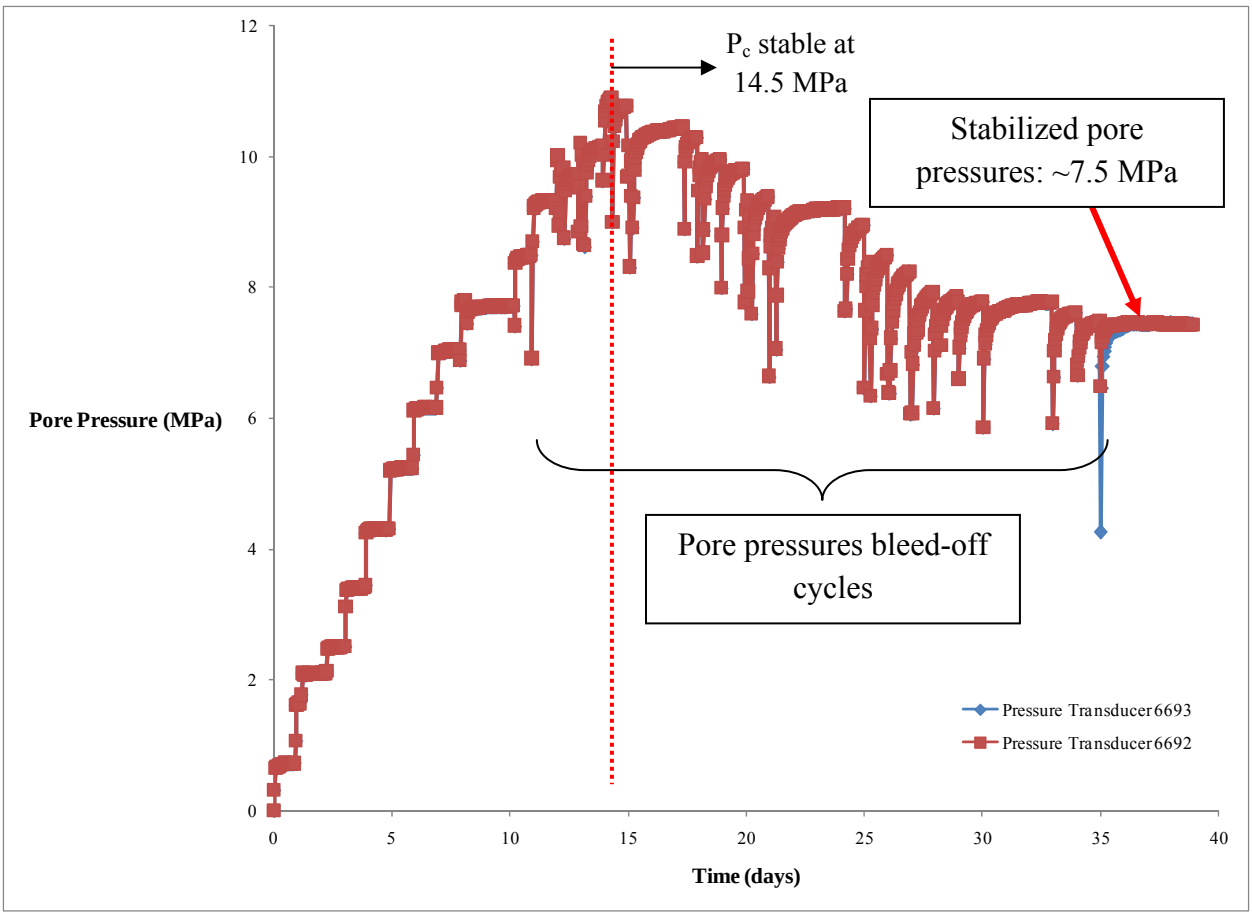

Fig. 4.16. Pore pressures during consolidation of Sample LP2.

4.3.7 Permeability Testing

Following consolidation, permeability testing was performed on each sample. A detailed description of test procedures can be found in Appendix A. Once the pore pressures in the upstream and downstream reservoirs had stabilized to approximately equal values, a pressure pulse was applied to the upstream end of the sample by opening valve 1, injecting a small volume of fluid using the pore fluid syringe pump, then reclosing valve 1. The pressure pulse was approximately 0.7 MPa (100 psi) greater than the downstream pore pressure. The pressure pulse was applied early in the morning and was monitored throughout the day, during which time a majority of the pressure difference would decay.

Over the course of the following days, the pore pressures were allowed to fully re-equilibrate, and additional tests were then performed.

4.3.8 CO_2 Breakthrough Pressure Testing

CO_2 breakthrough pressure testing was performed immediately after pressure re-equilibration following the final permeability test on a sample, using the same apparatus as the permeability testing. A detailed description of test procedures can be found in Appendix A.

Throughout (and at the conclusion of) permeability testing, the sample and all connected tubing were were believed to be saturated with brine. Prior to injecting CO_2 into the sample, the upstream reservoir had to be emptied of brine and filled with CO_2. This was done by bleeding off the pore pressure in the upstream reservoir, but maintaining the pore pressure in the downstream reservoir (i.e., leave valve 2 closed during this part). Once the pore pressure had been released from the upstream reservoir, a vacuum was applied to this section of tubing to remove any air and/or remaining brine from the tubing. CO_2 was then injected into the upstream reservoir at a pressure approximately equal to that in the downstream reservoir. The pressures should be approximately equal so that a pressure pulse is not inadvertently applied to the sample. Once the CO_2 had been injected, the system was left until it had re-stabilized. The system was considered to be stable once the pore pressures were approximately equal over a 24-hour period.

Using the CO_2-filled syringe pump, the pressure in the upstream end of the sample was increased by approximately 6 MPa for test number 1 (sample CS1), and by 0.5 MPa for all subsequent tests. These initial pressure increments were chosen in the hopes that they would not cause breakthrough. However, breakthrough did occur for all samples tested, hence implementation of the testing method of small incremental pressure increases (described in section 2.2.2.1) was not possible in this research. In all cases, then, the next step was to allow the test to run until the pressure in the downstream end of the sample increased and the two pressures stabilized.

Once the CO_2 breakthrough pressure testing was completed and the sample was removed from the triaxial cell and jacketing materials, the sample dimensions were taken and the

sample was weighed before and after oven-drying in order to determine the brine-saturated pore volume (hence enabling the calculation of porosity).

4.4 Sample Dimensions

Dimensions for the samples used for permeability and breakthrough pressure testing are presented in Table 4.3. Photos of each sample are presented in Fig. 4.17.

Table 4.3. Sample dimensions for Colorado shale and Lea Park shale samples, measured before permeability and breakthrough pressure testing.

Sample	Mass (g)	Length (m)	Diameter (m)	Area (m^2)
CS1	585.82	$6.4 \cdot 10^{-2}$	$7.6 \cdot 10^{-2}$	$4.5 \cdot 10^{-3}$
CS2	584.60	$5.8 \cdot 10^{-2}$	$7.7 \cdot 10^{-2}$	$4.6 \cdot 10^{-3}$
LP1	566.13	$5.8 \cdot 10^{-2}$	$7.6 \cdot 10^{-2}$	$4.6 \cdot 10^{-3}$
LP2	553.38	$5.5 \cdot 10^{-2}$	$7.6 \cdot 10^{-2}$	$4.6 \cdot 10^{-3}$

5. RESULTS

5.1 Permeability Testing

Results of the pressure pulse permeability testing are presented in Figs. 5.1 through 5.7.

When analyzing pressure pulse permeability test results, the easiest method of interpretation is to fit a straight line to the data when plotted in log(ΔP) versus time space (Brace et al. 1968). If the entire pressure decay history on such a plot, is not linear (the extent to which this holds is a function of testing system design), the selection of an appropriate time interval to use for the straight line fit requires an understanding of the flow processes occurring during the course of the test.

Brace et al.'s method (1968) assumes pseudo-steady-state conditions. However, initially, the volume of fluid flowing into any given section of rock may be significantly more than that flowing out. This can be seen by the initially steep, non-linear early-time section of a ln(ΔP) versus t plot. Brace's assumption is not met until the pressure drop is distributed evenly over the length of the sample, which is indicated by a linear ln(ΔP) versus t trend.

The initial non-linear character of the ln(ΔP) versus t plot may also be due, in part, to adiabatic compression; i.e., the sudden increase in pore pressure at the start of the test results in a slight temperature increase. Because the volumes of the reservoirs are so small, the temperature increase has a significant effect. A component of early-time pressure drop in the upstream results as the compression-induced temperature increase dissipates.

Pseudo-steady-state and isothermal conditions are generally met after a certain length of time, which depends on several factors including experimental set-up (i.e., reservoir volumes), ambient temperature, and the sample itself (e.g., properties, dimensions). In

Fig. 5.1, it can be seen that these conditions are met after approximately 2,800 s, or approximately 45 minutes.

It would be expected that the longer one waits, the more likely that pseudo-steady-state conditions will exist. However, as time progresses and the magnitude of the pressure difference across the sample (i.e., the "signal") becomes small, the component of pressure change caused by ambient temperature fluctuations (i.e., the "noise") can become problematic; i.e., the signal-to-noise-ratio becomes unfavourable. This makes analysis of the late-time data nearly impossible. For example, in Figure 5.1, it is apparent that noise becomes an issue possibly as early as 14,000 s (approximately hours) and without question from 25,000 s (approximately 7 hours) onwards. Therefore, the best option is to use the intermediate-time data which plot on a linear trend.

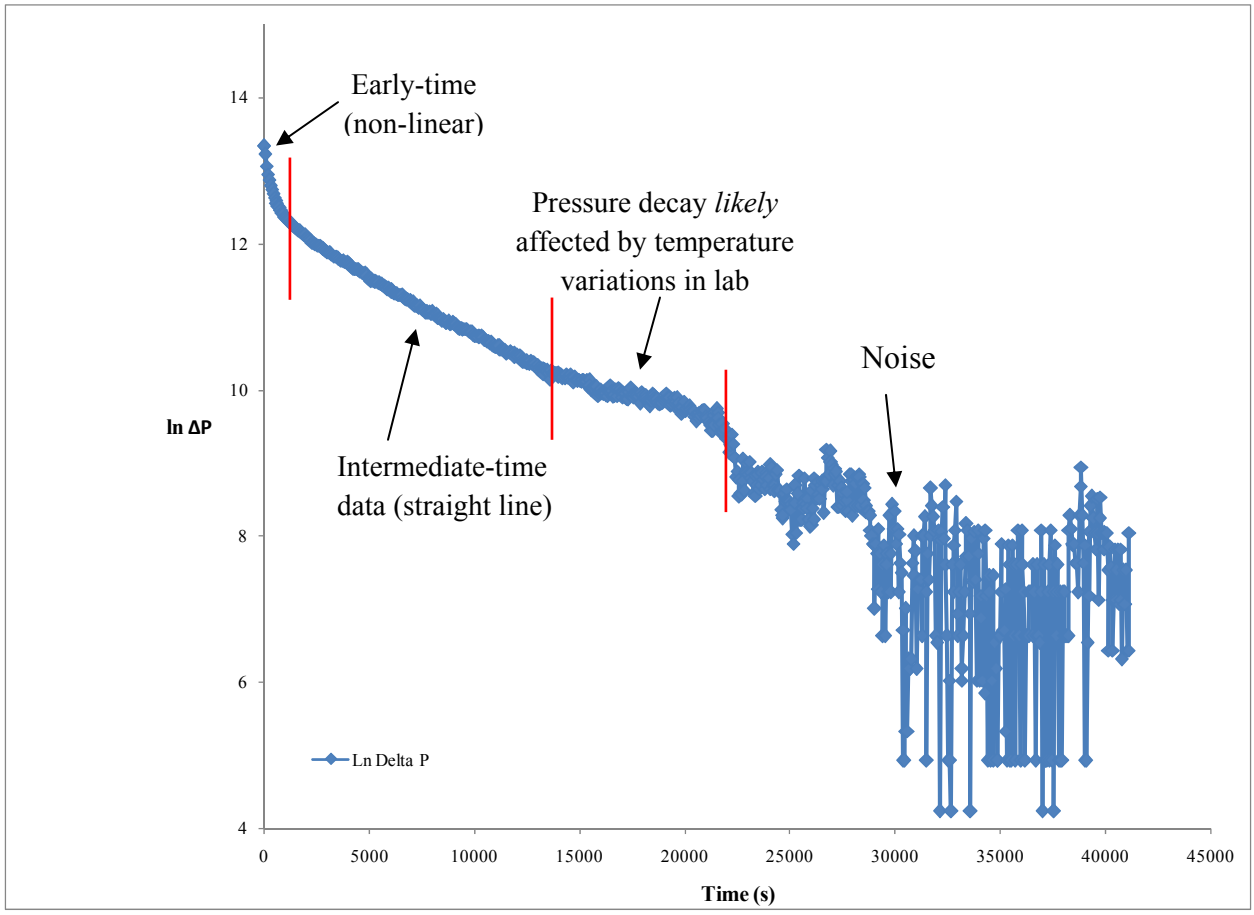

Fig. 5.1. Pressure pulse permeability results for Sample CS2 showing stages of test. Δ*P* in Pascals.

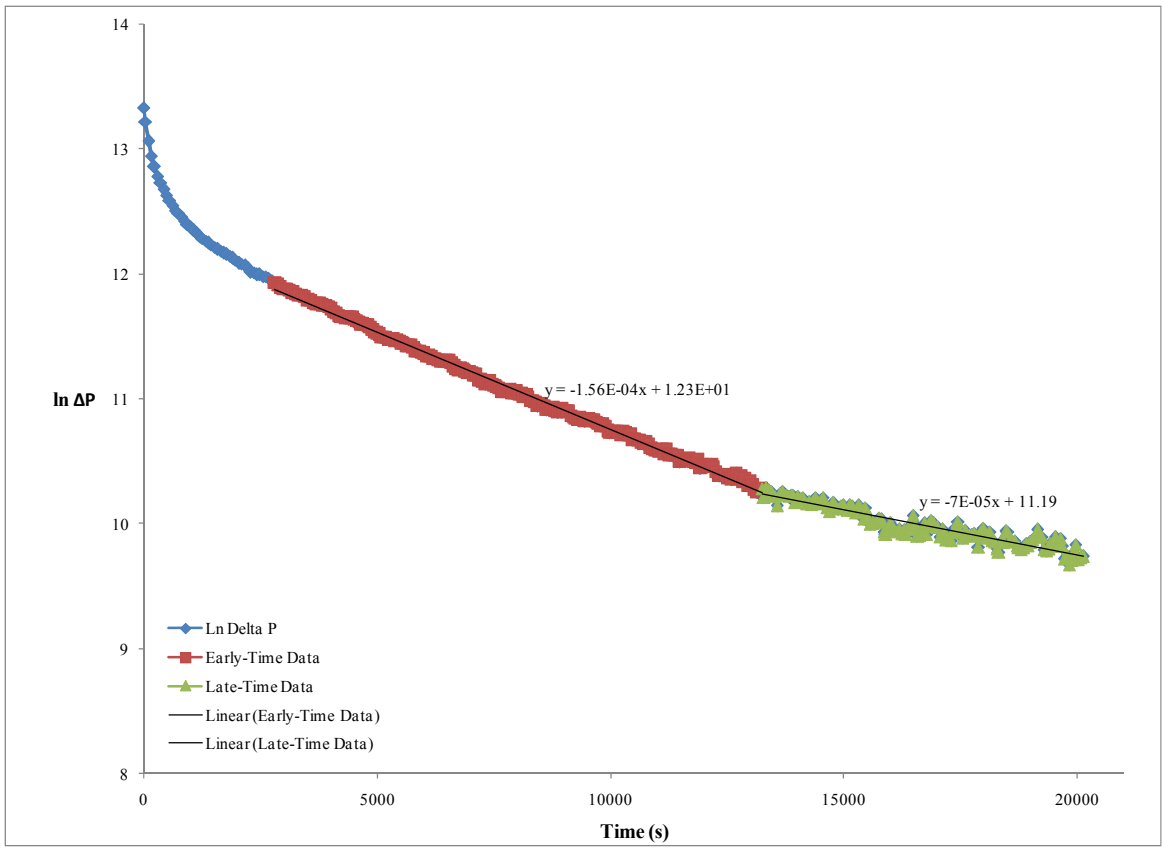

Fig. 5.2. Pressure pulse permeability results for Sample CS2 showing straight lines fitted to intermediate- and late-time data. Δ*P* in Pascals. Same data as presented in Fig. 5.1, truncated at 2,000s.

In some cases, the selection of an appropriate time-interval for linear trendline analysis may be somewhat ambiguous. Fig. 5.3 illustrates the most acute case of such an occurrence, for the data collected in this research; i.e., sample CS2. Analysis of Fig. 5.3 results in a 46 nanodarcy (nd) permeability for the intermediate-time data, and 20 nd for the late-time data. Given that permeability is often regarded as an "order of magnitude" parameter, this discrepancy is not considered significant. On the assumption that the intermediate-time data represents the best compromise between early-time non-linear flow phenomena and late-time signal-to-noise issues, the intermediate-time data was used for analysis of all pressure pulse permeability test results in this work.

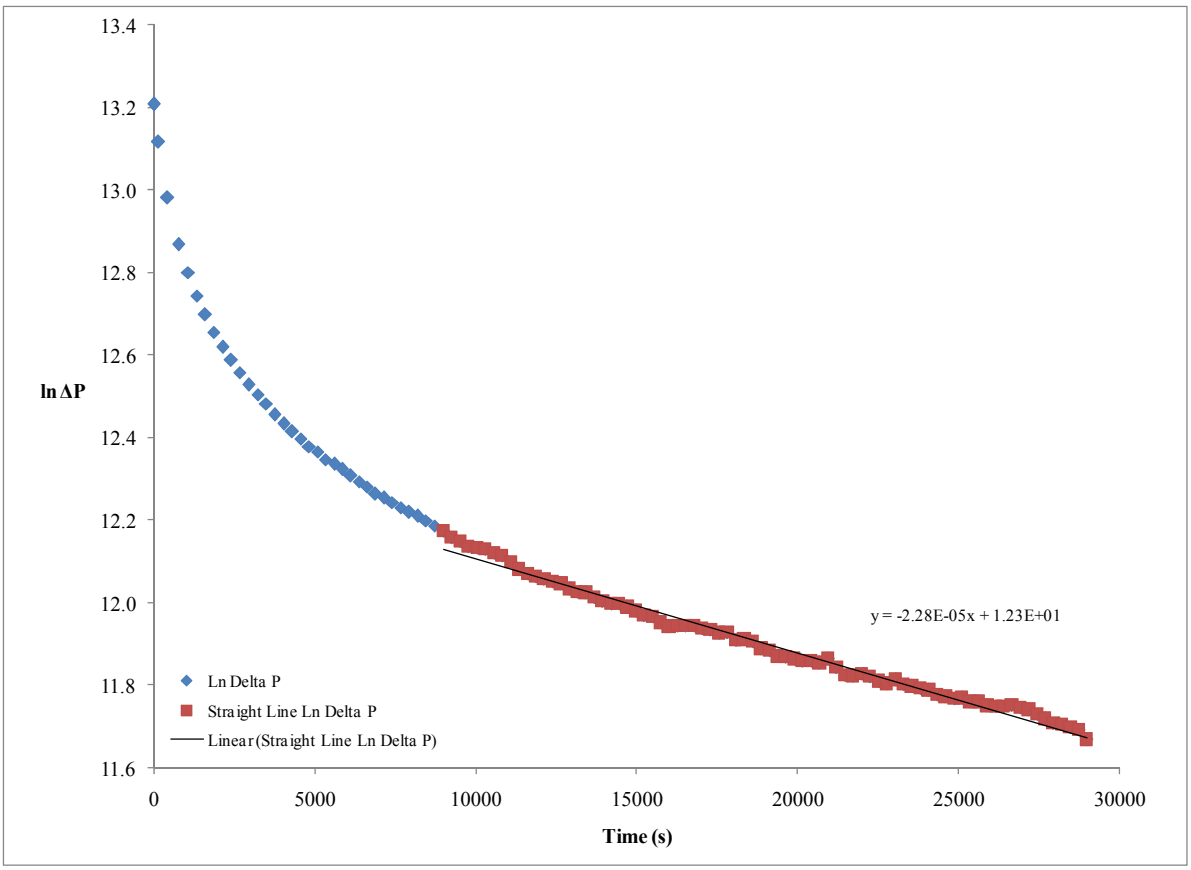

Fig. 5.3. Pressure pulse permeability results for Sample CS1. ΔP in Pascals.

Permeability is calculated using equation 2.1:

$$k = \frac{-a\mu L S_u S_d}{A(S_u + S_d)} \qquad [2.1]$$

Using sample CS1 as an example, the test parameters used for this calculation are:

a: $-2.28 \cdot 10^{-5}$ s^{-1} (slope from Fig. 5.4)

μ: $8.75 \cdot 10^{-4}$ Pa·s (Grimes et al. 1979)

L: 0.06355 m

S_u: $3.714 \cdot 10^{-14}$ $m^3 \cdot Pa^{-1}$

S_d: $9.649 \cdot 10^{-14}$ $m^3 \cdot Pa^{-1}$

A: $4.519 \cdot 10^{-3}$ m^2

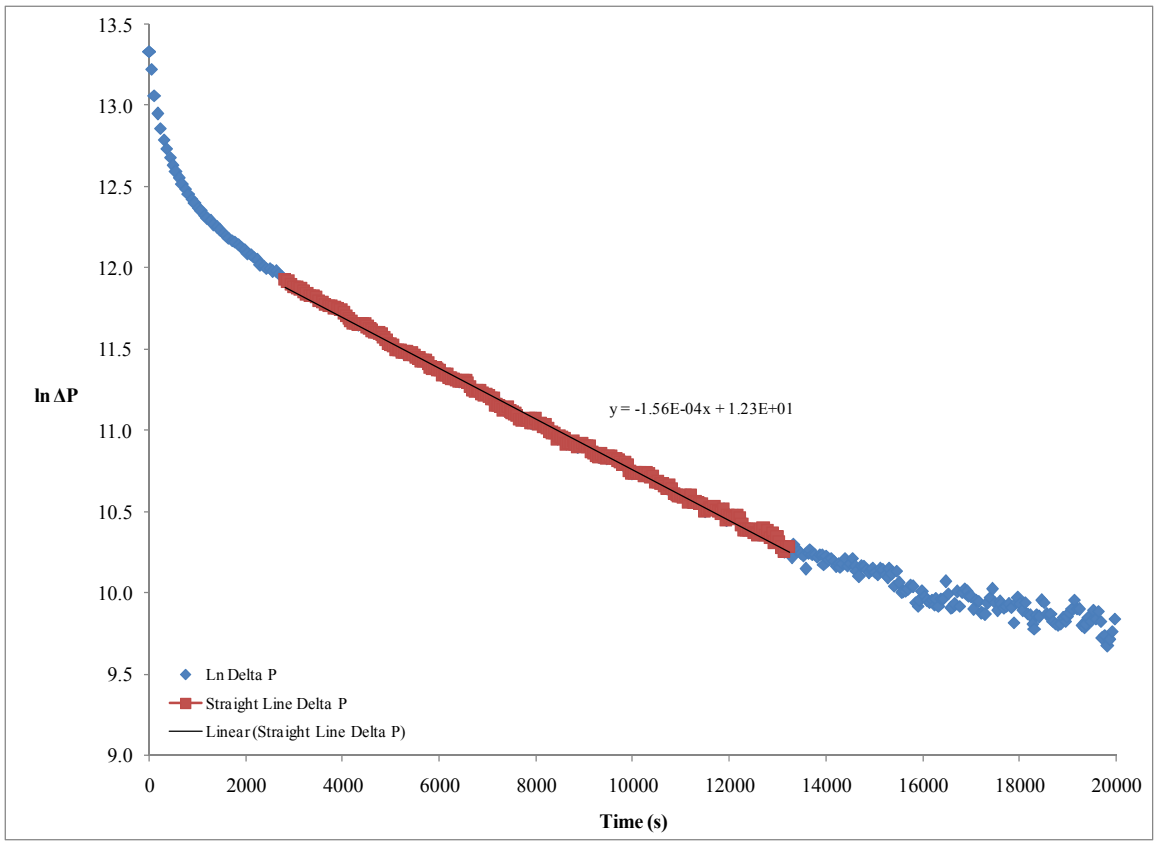

Fig. 5.4. Pressure pulse permeability results for Sample CS2. Δ*P* in Pascals.

From this, the permeability can be calculated as follows:

$$k = \frac{2.3 \cdot 10^{-5}\, s^{-1} * 8.75 \cdot 10^{-4} Pa \cdot s * 0.064m * 3.7 \cdot 10^{-14} m^3 \cdot Pa^{-1} * 9.6 \cdot 10^{-14} m^3 \cdot Pa^{-1}}{4.5 \cdot 10^{-3} m^2 (3.7 \cdot 10^{-14} m^3 \cdot Pa^{-1} + 9.6 \cdot 10^{-14} m^3 \cdot Pa^{-1})}$$

$$k = \frac{4.5 \cdot 10^{-36} m^4}{6.0 \cdot 10^{-16} m^2}$$

giving a permeability of:

$$k = 7.5 \cdot 10^{-21} m^2$$

or, converting to nd (10^{-21} m^2 ≅ 10^{-9} Darcy) and rounding off:

$$k \cong 8\, nd$$

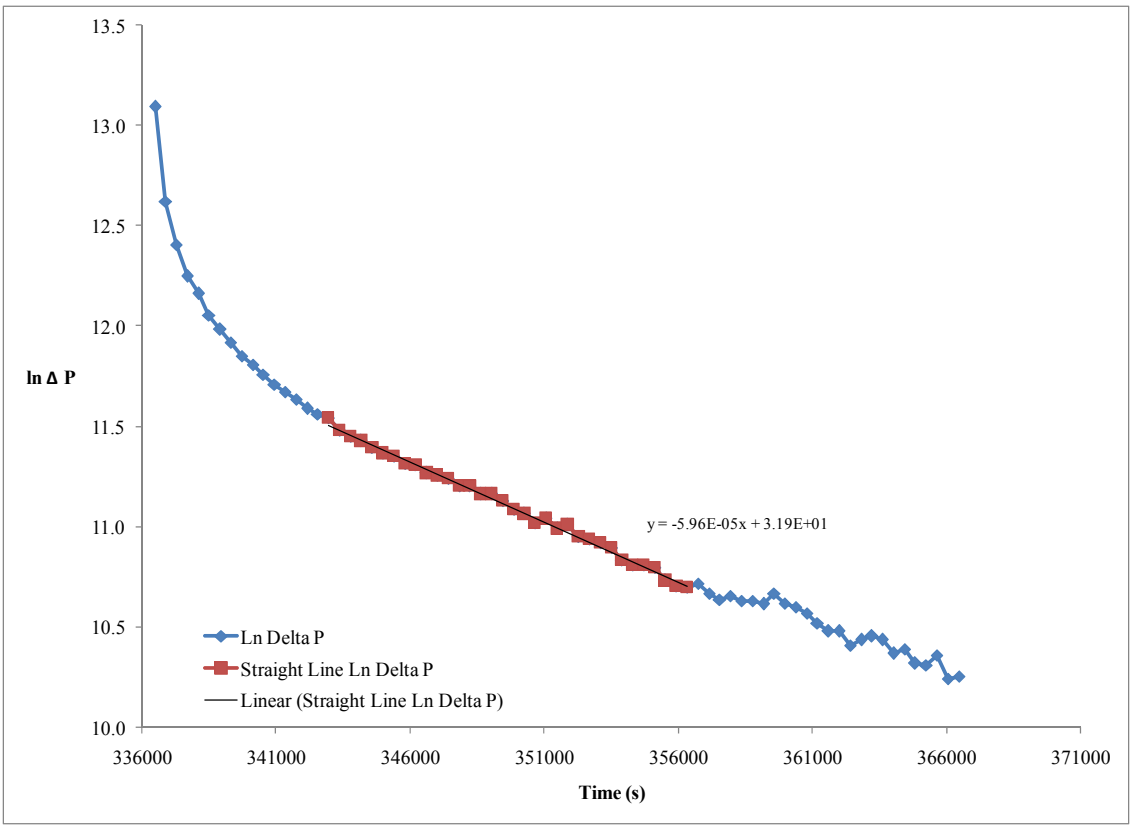

Fig. 5.5. Pressure pulse permeability results for Sample LP1. Δ*P* in Pascals.

As an alternate means of expressing the data, a permeability of 1 nd corresponds to a hydraulic conductivity of 10^{-14} m/s for a scenario in which the pore fluid is water.

Results of all of the permeability testing for samples from the Colorado shale and Lea Park shale are presented in Table 5.1.

5.1.1 Previous Permeability Testing Results

Permeability tests were previously conducted on samples of the Lea Park shale. These results were obtained with similar testing equipment as used in this research and using the pressure-pulse decay method described in Section 2.1. However, the samples were cut down to a 2-inch diameter using a knife and a consolidation ring.

The permeability of four samples was determined, with results ranging from 10^{-22} m^2 to 10^{-21} m^2 (i.e., 0.1 to 1 nd).

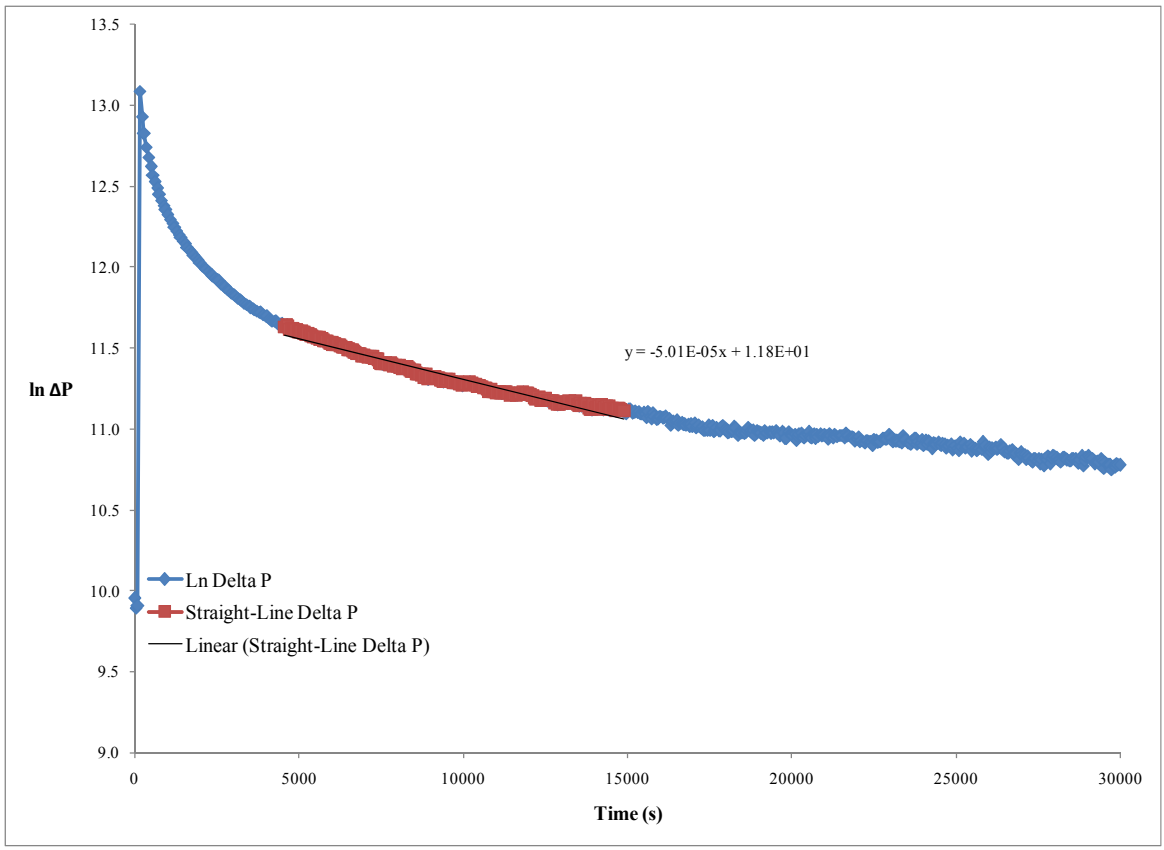

Fig. 5.6. Pressure pulse permeability results for sample LP2. Δ*P* in Pascals.

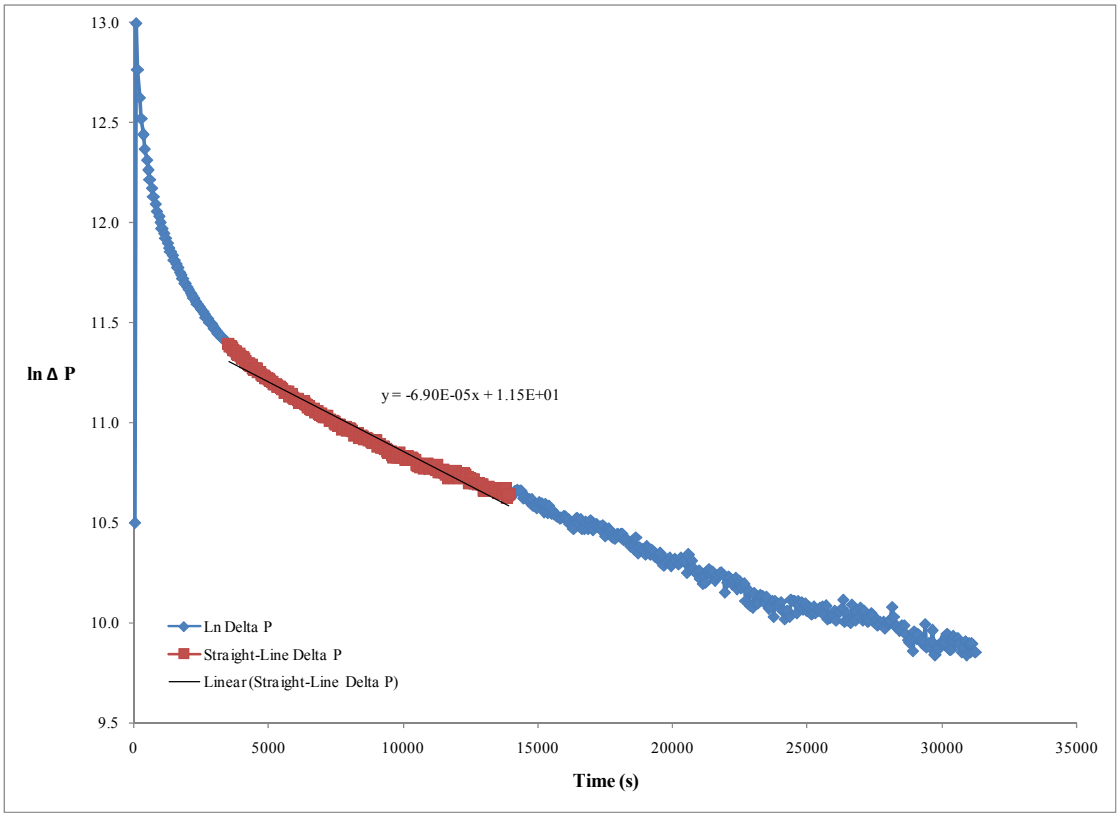

Fig. 5.7. Pressure pulse permeability results for sample LP2, by applying the pressure pulse to the downstream reservoir. ΔP in Pascals.

Table 5.1. Results of permeability testing for Colorado shale and Lea Park shale samples.

Sample	Depth (m)	Permeability (nd)
CS1	427.25 – 427.95[1]	8
CS2	428.50 – 429.25[1]	46
LP1	602.43 – 602.49	18, 35
LP2	610.30 – 610.35	14, 20[2], 28

Remarks:

1 Exact depth unknown; sub-sample (approx. 6 cm in length) was taken within the depth range indicated

2 This value was obtained by applying a pressure pulse to the downstream reservoir, whereas the others were obtained by applying a pressure pulse to the upstream reservoir.

5.2 CO_2 Breakthrough Pressure Results

Three out of the four samples used for permeability testing were subsequently subjected to breakthrough pressure tests which were successful. Breakthrough pressure testing on the fourth sample ultimately proved to be unsuccessful. Results for the successful and unsuccessful tests are given separately.

5.2.1 Samples CS1, CS2 and LP1

All samples were tested using the instantaneously high pressure increment as described in Sections 2.2.1.2 and 4.3. The results of these experiments are presented in Figs. 5.8 through 5.10. [Note: The small, incremental pressure increase method described in sections 2.2.1.1 and 4.3 was attempted on all samples except CS1; however, the first "small" increment selected in all cases was too large, and resulted in breakthrough. This is a symptom of the fact that the breakthrough pressures measured were smaller than initially expected.]

Results of the CO_2 breakthrough pressure testing are summarized in Table 5.2.

5.2.2 Sample LP2

A CO_2 breakthrough pressure was not obtained for Sample LP2. During sample preparation, the SkinFlex III jacket initially emplaced was not thick enough along one section of the sample. This was due to a slight bulge in the sample. As a result, a second SkinFlex III jacket was poured over the first. Prior to pouring the second jacket, the original SkinFlex III jacket was cleaned to remove the vacuum grease that was on it. This was a necessary step to ensure that the second jacket would seal to the first.

Once the second jacket was poured, Sample LP2 was loaded into the triaxial and testing proceeded as usual: the permeability testing was initially performed, followed by the CO_2 breakthrough pressure testing. It became clear early on in the CO_2 breakthrough pressure testing that something unusual was happening. Previously, the breakthrough pressure tests lasted approximately two to five days (see Figs. 5.8 through 5.10). With Sample LP2, the test went on for several weeks, with no usable results (e.g., erratic, inexplicable pressure variations occurred in both the upstream and downstream reservoir).

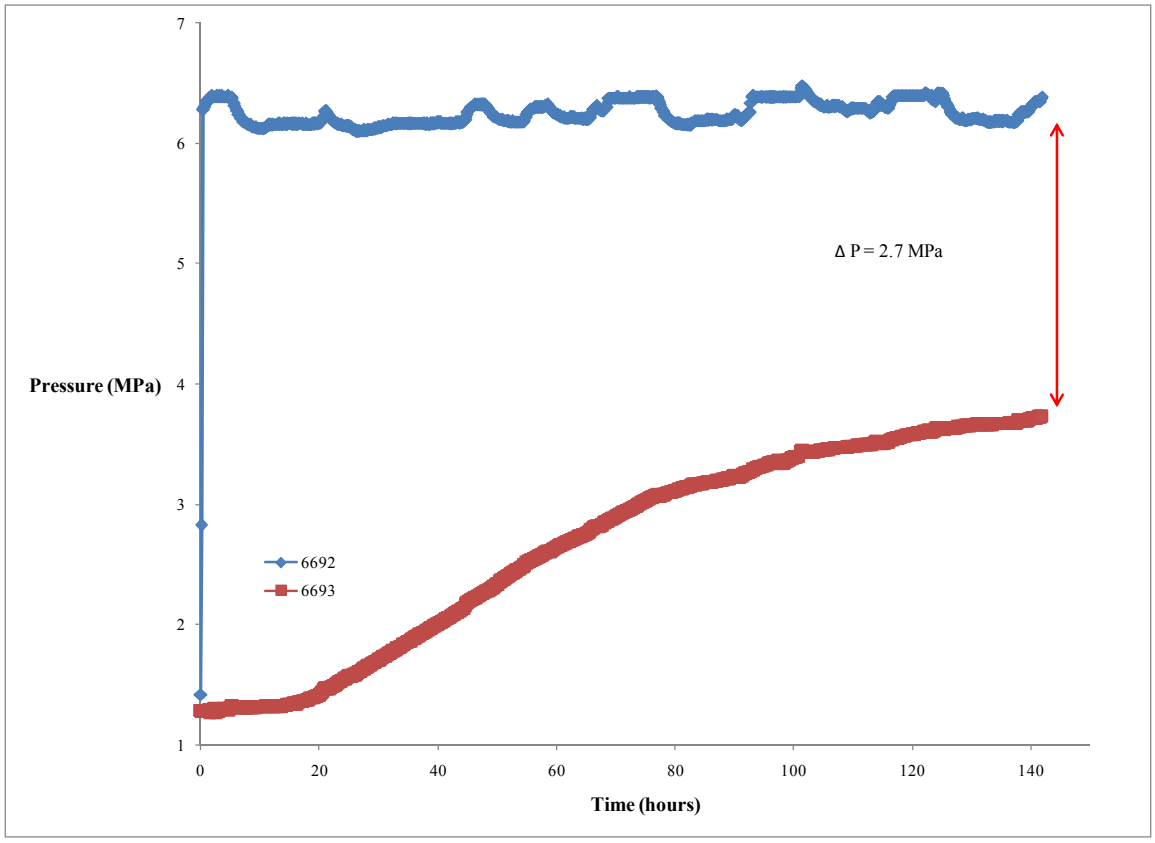

Fig. 5.8. CO_2 breakthrough pressure results for Sample CS1. Confining pressure during the test was 14.5 MPa.

After approximately two months, it was decided that something was fundamentally wrong and the test was ended.

When the sample was removed from the triaxial cell, it could be seen that there was some separation between the original SkinFlex III jacket and the second one. As shown in Figs. 5.11 and 5.12, some type of alteration of the Skinflex III had occurred. It is believed that the vacuum grease that was on the original SkinFlex III jacket had not been entirely cleaned off, and that this had enabled the separation of the two layers. Further, the grease may very likely have participated in a chemical reaction with the CO_2 and the Skinflex III.

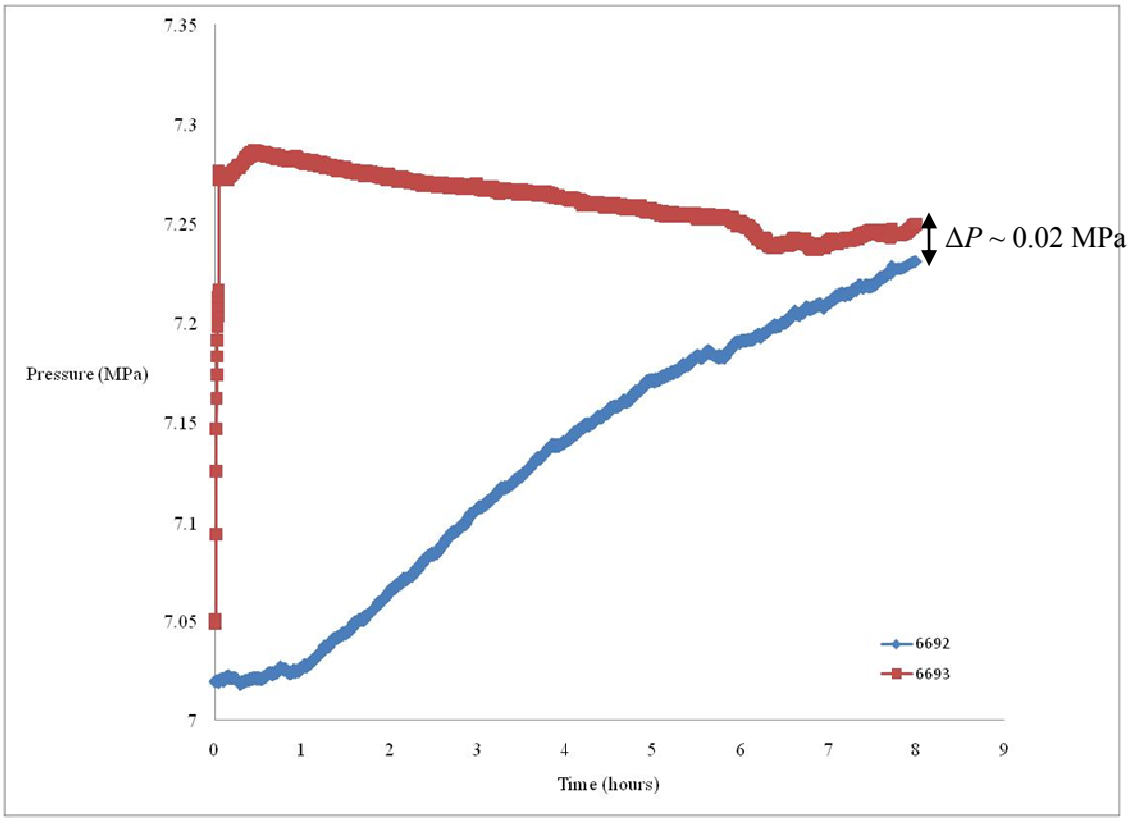

Fig. 5.9. CO_2 breakthrough pressure results for Sample CS2. Confining pressure during the test was 14.5 MPa.

5.2.3 Previous Breakthrough Pressure Results

CO_2 breakthrough pressure tests were previously conducted on samples of the Lea Park shale. These results were obtained with testing equipment similar to that used in this research, following using the method described in Section 2.2.1.2. However, the samples were cut down to a 2-inch diameter using a knife and a consolidation ring.

The CO_2 breakthrough pressures for two samples were determined to be 0.12 MPa and approximately 0.3 MPa, respectively.

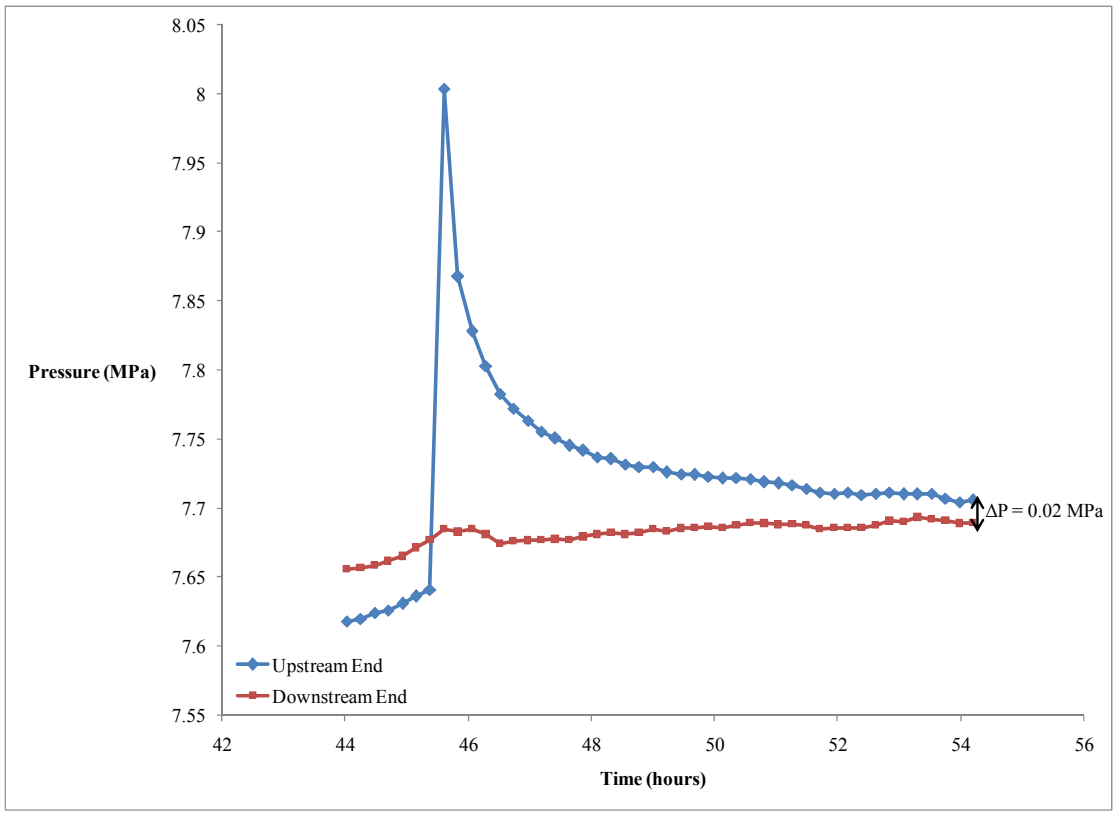

Fig. 5.10. CO_2 breakthrough pressure results for sample LP1. Confining pressure during the test was 14.5 MPa.

Table 5.2. Results of CO_2 breakthrough pressure testing for Colorado shale and Lea Park shale samples.

Sample	Depth (m)	Instantaneously Large ΔP (MPa)	Small, Incremental ΔP (MPa)
CS1	427.25 – 427.95[1]	2.7	N/A
CS2	428.50 – 429.25[1]	0.02	N/A
LP1	602.43 – 602.49	0.02	N/A
LP2	610.30 – 610.35	N/A	N/A

Remarks:

1 Exact depth unknown; sub-sample (approx. 6 cm in length) was taken within the depth range indicated

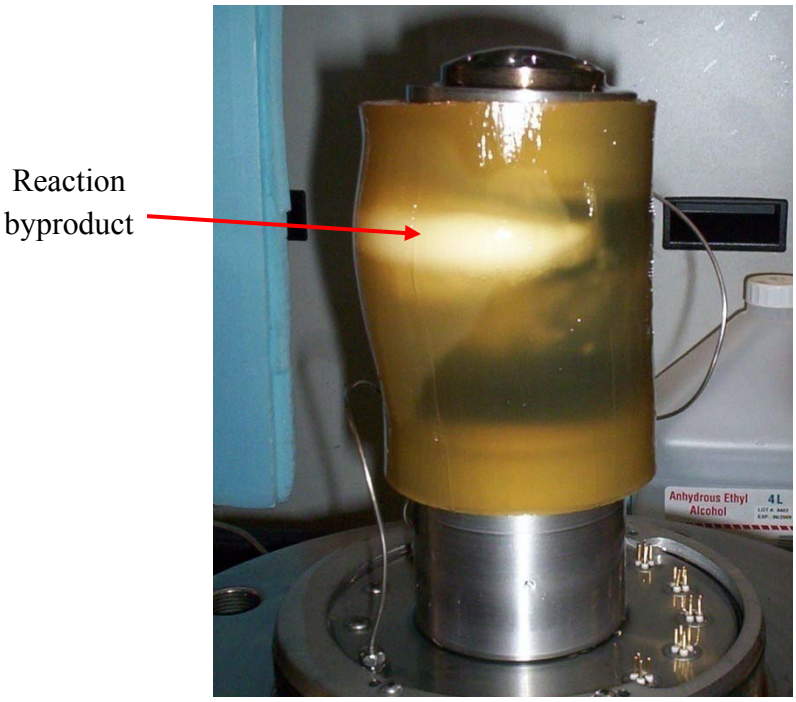

Fig. 5.11. Sample LP2 in the triaxial cell, showing reaction byproduct between the CO_2, SkinFlexIII, and vacuum grease.

Fig. 5.12. Two layers of SkinFlex III with the reaction byproduct.

5.3 Skempton's Coefficient, *B*

The undrained loading response of one of the Lea Park shale samples was analyzed in order to gain insights into the saturation state of the sample. Skempton's pore water pressure parameters, *A* and *B*, describe the change in total stresses on a sample during undrained loading (Day 1999). In general, the relationship can be described as follows:

$$\Delta P = B[\Delta\sigma_3 + A(\Delta\sigma_1 - \Delta\sigma_3)] \tag{5.1}$$

where ΔP is the change in pore water pressure during undrained shear loading [Pa], $\Delta\sigma_3$ is the change in total minor principal stress during an undrained loading event [Pa], $\Delta\sigma_1$ is the change in total major principal stress during an undrained loading event [Pa], and *A* and *B* are the Skempton pore water pressure coefficients [dimensionless]. During consolidation of the Colorado and Lea Park shale samples, the confining pressure was hydrostatic, so $\Delta\sigma_1 = \Delta\sigma_3$. Therefore, Skempton's *B* coefficient can be calculated as follows:

$$B = \frac{\Delta P}{\Delta\sigma_3} \tag{5.2}$$

where $\Delta\sigma_3$ is equal to the change in confining pressure. Based on this equation, *B* is a representation of how the pore pressure changes with respect to a change in confining pressure. For soils, in which the bulk compressibility of the sample is typically much less than the compressibility of water, a *B* value of approximately 1.0 is expected under saturated conditions. Conversely, a *B* value less than 1.0 is generally an indication that a sample is not fully saturated (Day 1999).

Fig. 5.14 presents two different time steps during consolidation of Sample LP2. Skempton's *B* coefficients were only calculated for Sample LP2. The early time data resulted in a Skempton's *B* coefficient of 0.9 and the late time data resulted in a Skempton's *B* coefficient of 0.7. [Note: Skempton's *B* coefficients were not calculated for Samples CS1 and CS2 due to a lack of usable data, nor for Sample LP1 because the consolidation data was lost due to a power outage.]

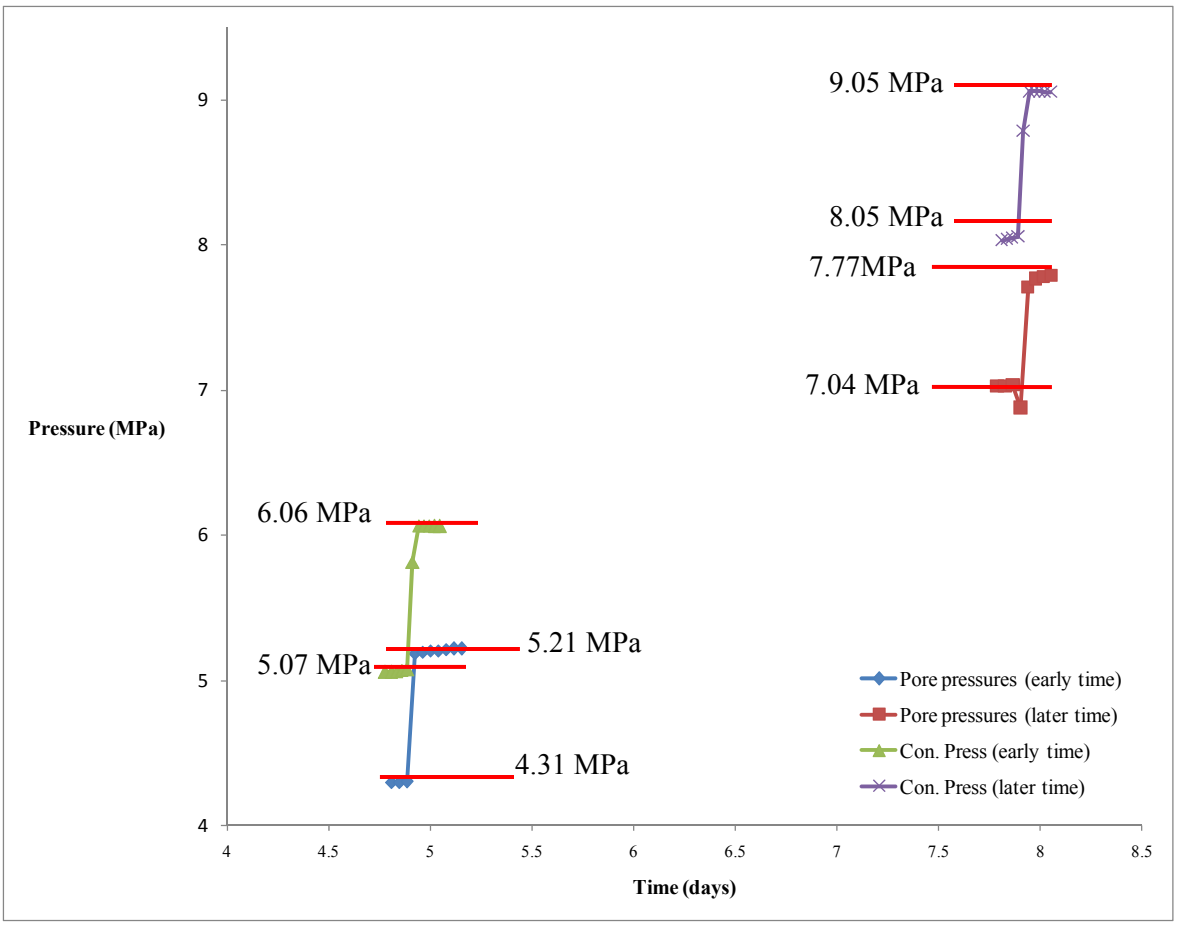

Fig. 5.14. Selected time steps during consolidation of Sample LP2.

It is also possible to calculate Skempton's *B* coefficient based on the properties of the porous medium and its pore fluid, as follows (e.g., Craig 2004):

$$B = \frac{1}{1+n\left(C_{fl}/C_b\right)} \tag{5.3}$$

where n is porosity [dimensionless], C_w is the pore fluid compressibility [Pa^{-1}], and C_b is the bulk compressibility of the rock [Pa^{-1}]. Table 5.4 presents the values that were used to determine *B* for sample LP2 using equation 5.3.

Table 5.4. Values used in the calculation of Skempton's B coefficient.

n	0.2
C_{fl}[1]	$4.4 \cdot 10^{-10}$ Pa^{-1}
υ_d[2]	0.27
E_d[2]	$4.5 \cdot 10^{9}$ Pa
E_s[3]	$3.1 \cdot 10^{9}$ Pa
K[4]	$2.2 \cdot 10^{9}$ Pa
C_b[5]	$4.5 \cdot 10^{-10}$ Pa^{-1}

Remarks:

1: Compressibility of water; from Dake (1978)

2: Dynamic elastic properties (υ_d and E_d) taken from ultrasonic velocity measurements presented in section 3.2.6.

Static Poisson's ratio (υ_s) assumed equal in magnitude to dynamic value (υ_d).

3: E_s is static Young's modulus

$E_s = 0.68E_d$ (empirical correlation, from Yale and Jamieson 1994)

4: $K = \frac{E_s}{3(1-2\upsilon_s)}$

5: $C_b = \frac{1}{K}$

Based on the values presented in Table 5.4, Skempton's *B* coefficient for sample LP2 was thus calculated as follows:

$$B = \frac{1}{1+n\left(C_{fl}/C_b\right)} \tag{5.3}$$

$$B = \frac{1}{1 + 0.2\left(\frac{4.4 \cdot 10^{-10}\ \mathrm{Pa}^{-1}}{4.5 \cdot 10^{-10}\ \mathrm{Pa}^{-1}}\right)}$$

$$B = 0.84$$

Typical values of Skempton's *B* coefficient for mudstone and clay are 0.83 and 0.99, respectively (Palciauskas and Domenico, 1989; Kumpel, 1991; as referenced in Reeves 2003).

The calculated value of 0.84 falls roughly half-way between the experimental values of 0.9 (early time data) and 0.7 (late time data), and is also consistent with values reported in the literature.

As previously mentioned, a *B* value that is less than 1.0 can indicate that a sample is not fully saturated in the case of soils or very soft sedimentary rocks. However, as the tests in this experimental program progressed, it is deemed unlikely that the cause of *B*-value decrease was a decrease in saturation because the samples were in contact with pressurized water – and no air – during the course of consolidation. Therefore, some other aspect of the system must have been changing. It is thought that, with increasing confining pressure and consolidation, the samples became stiffer; i.e., less compressible. From Equation 5.3, it can be seen that, for decreasing values of C_b, a smaller value of *B* would result. Thus, it seems reasonable to conclude that the samples were saturated during the course of testing.

6. DISCUSSION

6.1 Permeability Testing

6.1.1 Comparison to Literature Results

Results of the permeability tests done on both the Lea Park shale and the Colorado shale samples indicate that these rock units have very low permeabilities; i.e., of the order of tens of nanodarcies. These results fall within the range of shale permeabilities published previously by various authors (see Table 6.1).

6.1.2 The Pierre shale

The Pierre Formation (referred to as Pierre shale in this thesis) is found within central North America (Neuzil 1993), and is relevant to this research because it is stratigraphically equivalent to the Lea Park shale. The Pierre shale can be found at the southern edge of the Williston Basin in central South Dakota where it has been extensively studied (Neuzil et al. 1984; Nichols et al. 1986; Neuzil 1993; Nichols et al. 1994). In this area, the Pierre shale is mainly composed of clays, generally has pores in the micron-size range (Neuzil 1993), and is approximately 100% saturated with water (Nichols et al. 1986; Neuzil 1993). The in situ stress state of the Pierre shale in this area is approximately lithostatic (Nichols et al. 1986).

Faults are known to exist in the Pierre shale in central South Dakota (Nichols et al. 1994). Both normal and reverse faults are present in this area, with dips ranging between 40° and 90°, and vertical displacements ranging from less than one metre to 37 m (Nichols et al. 1994). These authors further reasoned that fracture spacings of 100 m to 1000 m could be expected in the Pierre shale in this area. Their boreholes, in general, did not intercept transmissive fractures, which suggested that such features, if present, were not closely spaced. This is supported by the fact that the fractures that were intercepted did not discharge any water, even over long observation periods.

Table 6.1. Permeability values for similar rock types.

Author and Year	Rock Type	Test Type	Location	Permeability (nd)
Katsube et al. 1996	Shale	Lab	Beaufort-Mackenzie Basin	0.2 to 19
Katsube et al. 1998	Shale	Lab	Scotian Shelf	0.9 to 23.9
			Beaufort-Mackenzie Basin	0.2 to 14.8
			Western Canada Sedimentary Basin	0.82 to 3.1
Horsrud et al. 1998	Shale	Lab	North Sea	3 to 317
Katsube et al. 1991	Shale	Lab	Scotian Shelf	0.1 to 16
Bredehoeft et al. 1983	Pierre shale	Lab	Local	500
Bredehoeft et al. 1983	Pierre shale	Field	Regional	6,000
Neuzil et al. 1984	Pierre shale	Lab	Local (pulse testing)	30 to 300
Neuzil et al. 1984	Pierre shale	Field	Regional (in situ testing)	300 to 3000
Chan 2005 (unpublished)	Lea Park shale	Lab	Weyburn, SK	0.1 to 1
This research	Colorado shale	Lab	Rocanville, SK	8 to 46
	Lea Park shale		Weyburn, SK	14 to 35

6.1.3 Scale-Dependence of Permeability

Large rock mass volumes in which the matrix is comprised of low-permeability rocks can have variable, scale-dependent permeabilities. If a small portion of that low-permeability rock is being tested, its permeability might be very small; i.e., at the nanodarcy scale. If a larger region is tested, its permeability might be noticeably larger owing to the potential

presence of fractures, faults, or joints. However, for rocks that have very low permeabilities, it is not practical to test them on a large scale as these tests would require unfeasibly long execution times. In-situ tests using boreholes are influenced by a small area immediately adjacent to the borehole but this area is most subject to disturbance from drilling the borehole. This could lead to increases in permeability due to mechanical disturbance, or decreases in permeability due to pore clogging or smearing in soft formations (Neuzil 1986). Laboratory determinations of small (i.e., core) scale permeability provide estimates at the low end of the permeability range for rock masses, assuming they have not been damaged extensively during coring. In any case, the only direct, practical approach to estimate matrix permeability is to conduct laboratory tests on samples that have no visible signs of damage. If the performance of a given rock's matrix as a seal is deemed acceptable based on laboratory measurements conducted on samples which have been damaged to some extent during coring, its performance should be even better in situ.

Bredehoeft et al. (1983) reported regional permeability values for the Pierre shale of 6 md, but a local value of 0.5 md. Neuzil (1986) reported that fractures may dominate the regional flow through the Pierre shale but that individual blocks are dominated by slow-responding transient flow conditions.

Neuzil et al.'s (1984) test results indicated that groundwater flow through the shale is scale-dependent, since the largest hydraulic conductivities were obtained from the largest samples. Transient pulse tests, conducted in a laboratory, resulted in hydraulic conductivities ranging between $3 \cdot 10^{-13}$ m s^{-1} and $3 \cdot 10^{-12}$ m s^{-1}, or 30 nd and 300 nd, respectively (see Table 6.1); these values are similar to those obtained in this work. Slug tests conducted in the field resulted in hydraulic conductivities ranging between $3 \cdot 10^{-12}$ m$\cdot s^{-1}$ and $3 \cdot 10^{-11}$ m s^{-1}, or 300 nd and 3000 nd, respectively (see Table 6.1) (Neuzil et al. 1984).

While insufficient information currently exists on the scale-dependence of Lea Park shale permeabilities in the Weyburn area, it is worth making a few comments on this topic. Firstly, it is interesting to note that lower values (up to one order of magnitude less) were measured on the Lea Park shale by Ting-Kai Chan (unpublished 2005), on samples that

were smaller than those used in this work (i.e., 2-inch diameter compared to 3-inch). Though this may suggest a scale-dependence on intact-rock permeability for this shale, it is difficult to draw a definitive conclusion on this matter. Factors that may also account for differences between Chan's results and those presented here include: geological heterogeneity; use of different testing system components; system calibration errors; and (possibly) more complete consolidation of the smaller samples used by Chan. Regarding flow at the larger-scale, analysis of geophysical logs from the area for signs of fracturing (ongoing work by M.Eng. student Michael McAllister) and 2D seismic reflection data for evidence of faulting (ongoing work by Professor Zoltan Hajnal and Ph.D. candidate Sandor Sule in the Department of Geological Sciences) may ultimately provide evidence of structural features that might affect larger-scale permeability. Also, ongoing work by Professor Benjamin Rostron (University of Alberta), which involves analysis of the pressure regimes and pore fluid compositions of aquifers above and below key aquitards in the Weyburn area, will provide indirect evidence on the large-scale permeability of the Colorado Aquitard.

Further to scale, the anisotropy of shale permeabilities deserves mention. Consolidation tests conducted on the Pierre shale by Neuzil et al. (1984) indicated that the horizontal conductivity is two times greater than the vertical conductivity. [Note: Though the focus of the research presented in this thesis has been vertical permeability, which is most relevant for the assessment of CO_2 containment, the textural anisotropy observed in SEM images of Lea Park and Colorado shale samples suggests that permeability in these rocks should also be anisotropic, with higher values in the horizontal direction.]

6.1.4 Evaluation of Error Associated with Permeability Determination

As mentioned in Section 2.1, the error associated with determining permeability using Equation 2.1 is dependent on the ratio of the effective sample pore volume and the reservoir volume. The criterion established by Trimmer (1981) to obtain an error less than 10% is as follows:

$$\frac{AL}{(S_u+S_d)}\frac{1}{M} \leq 0.25 \tag{6.1}$$

where A is the cross-sectional area of the sample (m^2), L is the length of the sample (m), S_u and S_d are the compressive storages for the upstream and downstream reservoirs ($m^3 \cdot Pa^{-1}$), respectively, and M is a parameter related to the compressive storage of the sample, defined as follows:

$$M^{-1} = nC_{fl} + [\alpha(1+n) - n]C_b \tag{6.2}$$

where n is the porosity of the sample, C_{fl} is the compressibility of the pore fluid (Pa^{-1}), α is Biot's coefficient (~1 for soft rocks), and C_b is the bulk compressibility of the rock (Pa^{-1}).

Using rock and fluid properties reported in Table 5.4, the value for M^{-1} for Lea Park shale is approximately $5.3 \cdot 10^{-10}$ Pa^{-1}. Using the sample dimensions reported in Table 5.1, and assuming that the Lea Park M value is also a reasonable estimate for the Colorado shale, Trimmer's compressive storage ratio (equation 2.1) was calculated for each sample tested in this work – see Table 6.2.

For all samples, the ratios were close to 1, which is significantly greater than the recommended value (for maximum 10% error) of 0.25. Upon further review of Trimmer's (1981) work, it is evident that a compressive storage ratio of 1 results in an error of approximately 20%. All things considered, a 20% error for the permeabilities measured in this work is deemed acceptable by the author.

Table 6.2 Calculated values of Trimmer's ratio.

Sample	Ratio
CS1	1.11
CS2	1.02
LP1	1.01
LP2	0.96

6.2 CO_2 Breakthrough Pressure Results

6.2.1 Comparison to Literature Results

Li et al. (2006) report that the retention of hydrocarbons in a reservoir for geological periods of time is usually due to the high sealing capacity of the overlying seals. Schlomer and Krooss (1997) state that hydrocarbons are retained by overlying seals due to the capillary entry pressure of these rocks. They also state that hydrocarbon movement through the seal will be controlled by permeability once the capillary entry pressure has been exceeded.

Results of the CO_2 breakthrough pressure tests done on both the Lea Park shale and the Colorado shale samples indicate that these rock units have very low CO_2 breakthrough pressures (~0.02 MPa), with the exception of one Colorado shale sample which had a moderate breakthrough pressure of 2.7 MPa. This suggests a low capillary sealing capacity of these rocks with respect to CO_2. However, given the very low permeabilities of these rocks, even if CO_2 were to penetrate them, it would flow very slowly.

Published results of breakthrough pressure testing on other caprock and aquitard lithologies are presented in Table 6.3.

Table 6.3. Published CO_2 breakthrough pressure values for similar rock types.

Author and Year	Rock Type	Location	CO_2 Breakthrough Pressure (MPa)
Hildenbrand et al. 2004	Pelitic rocks	Not given	0.1 to 4.9
Li et al. 2005	Evaporite	Weyburn, SK	9.2 to 21.4
Chan 2005 (unpublished)	Lea Park shale	Weyburn, SK	~0.1 to ~0.3
This research	Colorado shale	Rocanville, SK	0.02 and 2.7
	Lea Park shale	Weyburn, SK	0.02

6.2.2 Capillary Properties of Brine-CO_2-Rock Systems

As previously discussed in Section 2.4, the ability of a caprock to provide an effective seal to CO_2 depends on the interactions occurring between the CO_2, the formation brine, and the formation itself.

At this point it in the discussion, it is useful to recall equation 2.2, which quantifies the effects of fluid and rock properties on the capillary pressure (P_{cap}) required for non-wetting fluid to enter a pore throat of radius r (or diameter d):

$$P_{cap} = \frac{2\sigma}{r} cos\theta = \frac{4\sigma}{d} cos\theta \tag{2.2}$$

where σ is the interfacial tension (IFT) between the non-wetting phase and the wetting phase [$N \cdot m^{-1}$], and θ is the contact angle (i.e., the angle between the fluid interface and the mineral grain surface, measured within the denser of the two fluid phases) (Fig. 2.7).

Chalbaud et al. (2009) obtained some experimental results for brine-CO_2-rock IFTs. Selected values, measured under similar to conditions in this thesis work, are presented in Table 6.4.

As noted by Chalbaud et al. 2009, interfacial tension and rock wettability (as parameterized by the contact angle) control the capillary-sealing ability of a given caprock or aquitard. Hence, it is important to know the values of these properties (and how they vary in the presence of CO_2) when evaluating the effectiveness of a rock as a capillary seal for a storage project.

Table 6.4. Selected IFT results for brine/CO_2/rock systems (from Chalbaud et al. 2009).

Temperature (°C)	Pressure (MPa)	Salinity (molality)	Brine Density ($kg \cdot m^{-3}$)	CO_2 Density ($kg \cdot m^{-3}$)	IFT ($N \cdot m^{-1}$)
27	8.2	0.085	1015.4	757.05	$2.75 \cdot 10^{-2}$
27	9.5	0.87	1042.8	790.73	$2.91 \cdot 10^{-2}$
27	8.2	0.87	1042.2	757.01	$2.88 \cdot 10^{-2}$
27	9.5	1.79	1071.4	785.20	$2.82 \cdot 10^{-2}$

Chiquet et al. (2007) conducted experiments to determine contact angles for mineral/brine/CO_2 systems, using quartz (to represent behaviour in sandstone reservoirs) and muscovite mica (as a proxy for illite, to represent behaviour clay-rich caprocks). If a caprock or aquitard were to lose its water-wettability, its sealing capacity with respect to CO_2 would decrease, or even vanish completely. Chiquet et al. (2007) observed a significant variation in the wetting behavior with pressure, especially in the system with mica. At low pressures, water-wet behavior was observed, with the contact angle ranging between 10° and 30°. At higher pressures, the contact angle was approximately 60° at 11 MPa for the mica. At 11 MPa, the contact angle for quartz was approximately 35°.

Chiquet et al. (2007) report that the contact angle variation observed with CO_2 is mostly due to changes in brine pH. When the CO_2 pressure is approximately zero, the brine pH is essentially neutral. However, as the CO_2 pressure is increased above 8 MPa, the brine pH drops to approximately 3. This lower pH decreases the effectiveness of repulsive electrostatic interactions at the mineral/brine and brine/CO_2 interfaces. These repulsive interactions would normally act to stabilize the brine film on the mineral grains, which would then tend to favour water-wettability. However, when these interactions are de-stabilized by a lower pH, water-wettability is no longer dominant and a continuous water-wet phase may no longer exist, resulting in the observed increase in contact angles. The overall implications of the reduction in interfacial tension and water-wettability means that the capillary sealing capacity of a given caprock or aquitard is significantly reduced (Chiquet et al. 2007).

Table 6.5. Selected interfacial tension results for brine/CO_2/rock systems from Bennion and Bachu (2006).

Formation	Rock Type	Pressure (MPa)	Temperature (°C)	Salinity (ppm)	IFT ($N \cdot m^{-1}$)
Calmar	Shale	12.25	43	129,688	$2.76 \cdot 10^{-2}$
Nisku	Carbonate	17.40	56	136,817	$3.46 \cdot 10^{-2}$
Cooking Lake	Carbonate	15.50	55	233,417	$3.57 \cdot 10^{-2}$

Bennion and Bachu (2006) also performed experiments to determine the interfacial tension of carbonate and shale samples. Their results are presented in Table 6.5.

From these results, it can be seen that the interfacial tension is slightly higher in the presence of carbonates than for clastic silicates, at least for this data set. This means that, all other things being equal, the breakthrough pressures for carbonates can be expected to be slightly higher than for shales. This is consistent with the results obtained in this research: Sample CS1, which is roughly 90% calcite, had the highest breakthrough pressure at 2.7 MPa, as compared with Sample LP1, which had a breakthrough pressure of 0.02 MPa and a calcite content of roughly 3%.

6.2.3 Contact Angle Calculations

Performing CO_2 breakthrough pressure tests on shales can be very challenging. Mercury porosimetry is a standard test that is easier to perform and provides information on pore dimensions that should be suitable to calculate estimates of breakthrough pressures for other non-wetting fluids, provided that the interfacial tension and contact angle are known.

Using the breakthrough pressures obtained during this testing program, along with the pore diameters obtained from the mercury porosimetry results, contact angles for the brine-CO_2-shale systems tested in this work can be calculated by rearranging equation 2.2 as follows:

$$\theta = cos^{-1}\left(\frac{rP_{cap}}{2\sigma}\right) = cos^{-1}\left(\frac{dP_{cap}}{4\sigma}\right) \tag{6.3}$$

where d is the critical diameter of the pore throat [m], P_{cap} is the experimentally-determined CO_2 breakthrough pressure [Pa], and σ is the interfacial tension [$N \cdot m^{-1}$].

Using Sample LP1 as an example, the test parameters for this calculation are:

$d = 3 \cdot 10^{-8}$ m (estimated based on results for samples CHRS-005 and 006)

$P_{cap} = 2.0 \cdot 10^{4}$ Pa = 0.020 MPa

σ = 2.8 · 10^{-2} N·m^{-1} (assumed value, based on Chun and Wilkinson 1995 and Chalbaud et al. 2009)

$$\theta = cos^{-1}\left(\frac{3\cdot10^{-8}m\cdot2.0\cdot10^{4}Pa}{4\cdot2.8\cdot10^{-2}\frac{N}{m}}\right) = 89.7°$$

Calculation results for all of the samples tested in this work are summarized in Table 6.6. It is significant to note that the contact angles of approximately 90° (hence $\cos\theta \sim 0$) indicate intermediate wettability to CO_2, and low capillary pressures.

Using the contact angles given above, breakthrough pressures can be estimated using mercury porosimetry results for rocks with similar lithologies to the Lea Park shale and the Colorado shale. Mercury porosimetry tests are much quicker than breakthrough pressure tests in terms of sample preparation and test time, though it remains to be seen if the effects of sample desiccation (which is required for mercury porosimetry testing) are significant and/or if they can be accounted for in some fashion.

Table 6.6. Results of contact angle calculations.

Sample	BTP[1] (MPa)	Pore Diameter (μm)	θ (°)
CS1	2.7	0.1	N/A[2]
CS2	0.02	0.1	89.0
LP1	0.02	0.03	89.7
LP2	N/A	0.03	N/A[3]

Remarks:

1. BTP denotes CO_2 breakthrough pressure
2. $BTP > \frac{4\sigma}{d}$; since the maximum value of $\cos\theta$ is 1, this indicates that the σ value assumed for these calculations was not appropriate for sample CS1, or that d was overestimated by the mercury porosimetry analysis (e.g., due to desiccation effects)
3. Test failed, hence BTP was not measured

6.3 Practical Implications of Results Obtained in This Work

6.3.1 Hydraulic Diffusion of CO_2

Once the permeability and CO_2 breakthrough pressures have been measured, it is desirable to know the practical relevance of those values. A key question, for example, is: How long could it take for CO_2 to potentially pass through a representative cross-sectional area of the Lea Park shale? A convenient means of accomplishing this is to use published solutions of transient diffusion problems. In particular, Fig. 6.1 shows a relevant solution for 1-dimensional diffusion across a laterally infinite sheet with uniform thickness denoted l. In the context of this research, the "sheet" may be regarded as the Lea Park shale, and a relevant "diffusion" process is hydraulic flow from the base of the Lea Park to the top, driven by a pressure increment (denoted C_1) at its base (and assuming negligible capillary resistance to flow (i.e., BTP ~ 0). Fig. 6.1 shows the cumulative volume of flow (Q_l) through the top of the Lea Park shale, normalized by the factor $l \cdot C_1$ (though the details of this normalization are not significant here, as we are only concerned with the time required reach certain milestones), as a function of dimensionless time ($D \cdot t/l^2$, where D is the diffusion coefficient and t is time).

From Fig. 6.1, it can be seen that flow will start to appear at the top of the Lea Park shale (i.e., the "outlet" face of the "sheet") at a dimensionless time of approximately 0.09. Re-arranging, this leads to the relation:

$$t_{outlet} = 0.09 \frac{l^2}{D_h} \tag{6.4}$$

where t_{outlet} is the time it takes for transient flow of CO_2 to reach the top of the Lea Park shale, l is a representative thickness of the Lea Park shale and D_h is the hydraulic diffusion coefficient, which is calculated as follows:

$$D_h = \frac{k}{\mu}\left(\frac{1}{nC_{fl}+C_b}\right) \tag{6.5}$$

where k is permeability (m^2), μ is fluid (CO_2) viscosity (Pa·s), n is porosity, C_{fl} is the fluid (CO_2) compressibility (Pa^{-1}), and C_b is the bulk compressibility of the rock (Pa^{-1}).

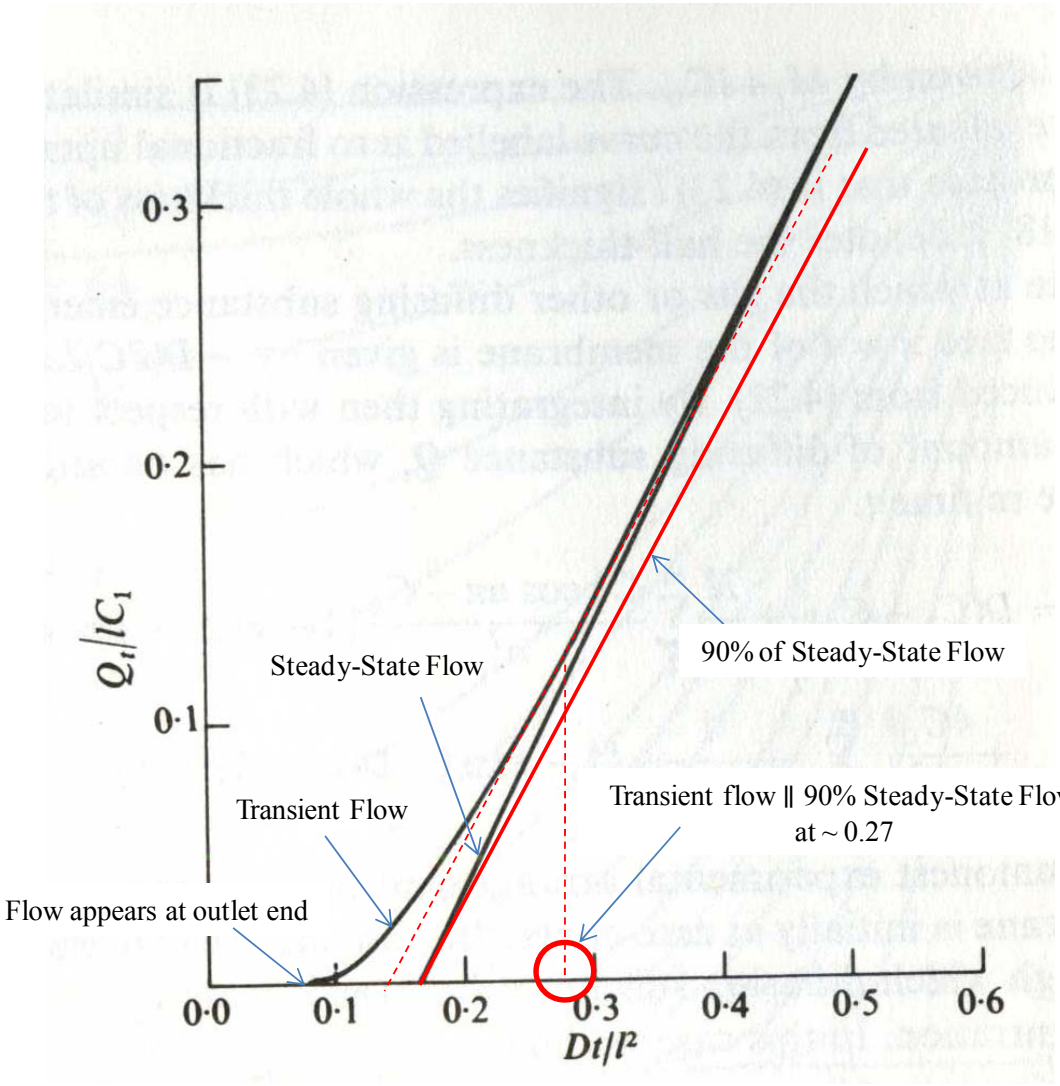

Fig. 6.1. Cumulative, dimensionless flow through the top of a sheet of thickness *l*, as a function of dimensionless time (after Crank 1975). The solid black curve shows the cumulative flow. The solid black line shows the slope of the cumulative flow curve once steady-state conditions have been achieved. The solid red line (denoted "90% of Steady-State Flow") shows the slope of the cumulative flow curve once the transient flow rate is 90% of the steady-state flow rate. The dashed red line shows the point at which the tangent to the transient flow curve is parallel to the 90% of Steady-State Flow line.

In the following, a representative permeability of 10 nd (or 10^{-20} m^2) was assumed based on test results obtained in this research. Other test parameters used for this calculation are as follows:

$\mu = 6.14 \cdot 10^{-5}$ Pa·s (Diller and Ball 1985)

$n = 0.2$ (representative value obtained for Lea Park shale samples in this research)

$C_{fl} = 3.3 \cdot 10^{-7}$ Pa^{-1} (Supercritical Fluid Technologies, 2010)

$C_b = 4.5 \cdot 10^{-10} Pa^{-1}$ (see Table 5.4)

The hydraulic diffusion coefficient was thus calculated as follows:

$$D_h = \frac{10^{-21} m^2}{6.14 \cdot 10^{-5} Pa \cdot s}\left[\frac{1}{(0.2)3.3 \cdot 10^{-7} Pa^{-1} + 4.5 \cdot 10^{-10} Pa^{-1}}\right]$$

$$D_h = 2.45 \cdot 10^{-9} \frac{m^2}{s}$$

Considering a representative thickness, l, of the Lea Park shale of 100 m, t_{outlet} is

$$t_{outlet} = 0.09\left(\frac{(100\ m)^2}{2.45 \cdot 10^{-9} \frac{m^2}{s}}\right)$$

$$t_{outlet} = 3.7 \cdot 10^{11} s\ or\ 1.2 \cdot 10^{5} years$$

This means that it would take over ten thousand years for CO_2 to reach the top of the Lea Park shale (in the event that it were accumulate beneath this formation and generate an overpressure).

From Fig. 6.1, it can also be seen that transient flow will approach steady-state flow, within 10%, at a dimensionless time of approximately 0.027. This time, denoted t_{90}, is calculated as follows:

$$t_{90} = 0.27 \frac{l^2}{D_h} \tag{6.6}$$

$$t_{90} = 0.27\left(\frac{(100\,m)^2}{2.45 \cdot 10^{-9}\frac{m^2}{s}}\right)$$

$$t_{90} = 1.1 \cdot 10^{12} s \; or \; 3.5 \cdot 10^{5} years$$

6.3.2 Chemical Diffusion of CO_2

As mentioned in Section 2.4.2, chemical diffusion of CO_2 can occur through an aquitard if the CO_2 dissolves into the aquitard's saturated pore spaces (Busch et al. 2008). Further to the hydraulic diffusion described in the previous section, this represents another mechanism of CO_2 transport through the Lea Park shale, should CO_2 accumulate beneath it.

Fig. 6.1 can be used to assess CO_2 transport for chemical diffusion in the same manner as described on the previous section, the key difference being that the chemical diffusion coefficient is used rather than the hydraulic diffusion coefficient. Since no diffusion experiments were performed in this research, values for D as reported in Busch et al. (2008) were used. These reported values were determined experimentally on the Muderong Shale. They reported two D values: $3.08 \cdot 10^{-11}$ m^2/s and $4.81 \cdot 10^{-11}$ m^2/s.

Using $D = 3.08 \cdot 10^{-11}$ m^2/s, t_{outlet} and t_{90} work out to $9.3 \cdot 10^5$ years and $2.8 \cdot 10^6$ years, respectively. Using $D = 4.81 \cdot 10^{-11}$ m^2/s, t_{outlet} and t_{90} work out to $5.9 \cdot 10^5$ years and $1.6 \cdot 10^6$ years, respectively. For these diffusion coefficients, it can be seen that chemically-driven diffusion will take over five times longer than hydraulically-driven diffusion.

A comparison of times obtained for hydraulically-driven and chemically-driven diffusion is presented in Table 6.7.

Table 6.7. Comparison of times for hydraulically-driven and chemically-driven diffusion.

Hydraulic Diffusion		Chemical Diffusion			
D_h (m^2/s)	$2.45 \cdot 10^{-9}$	D (m^2/s)	$3.08 \cdot 10^{-11}$	D (m^2/s)	$4.81 \cdot 10^{-11}$
t_{outlet} (years)	$1.2 \cdot 10^{5}$	t_{outlet} (years)	$9.3 \cdot 10^{5}$	t_{outlet} (years)	$5.9 \cdot 10^{5}$
t_{90} (years)	$3.5 \cdot 10^{5}$	t_{90} (years)	$2.8 \cdot 10^{6}$	t_{90} (years)	$1.6 \cdot 10^{6}$

6.3.3 Steady-State Flow

As demonstrated in Section 6.3.1, it would take of the order of 10^5 years for CO_2 to flow through a 100 m thickness of Lea Park shale and to begin to approach steady state conditions. Although it is likely that any CO2 beneath the Lea Park shale would have dissipated by other means over such an extended period of time (e.g., dissolution into formation brine of underlying aquifer(s)), this section presents a calculation of steady-state flow rate in order to assess a worst-case scenario in which the driving force for leakage is still in place after tens of thousands of years. In such a case, the steady-state flow rate can be calculated as follows:

$$Q = \Delta P \cdot \frac{k}{\mu} \cdot \frac{A}{X} \tag{6.7}$$

where Q is the flow rate of CO_2 through the Lea Park shale [m^3/s], ΔP is the incremental pressure at the base of the Lea Park shale [Pa], k is the effective permeability to CO_2 [m^2], μ is the CO_2 viscosity [Pa·s], A is the cross-sectional area being considered [m^2], and l is the thickness of the Lea Park shale [m].

Using Sample LP1 as an example, the test parameters for this calculation are as follows:

ΔP = 3.5 MPa = $3.5 \cdot 10^6$ Pa (an approximate upper limit on pressure increase, beyond wich a hydraulic fracture would be induced)

k = 10 nd = 10^{-20} m^2 (based on the conservative assumption that the effective permeability to CO_2 in a two-phase saturation condition is equivalent to the instrinsic permeability measured in laboratory tests conducted using brine as the sole pore fluid)

μ = $6.14 \cdot 10^{-5}$ Pa·s (Diller and Ball 1985)

A = $1.7 \cdot 10^{8}$ m^2 (a conservative estimate, based on the assumption that CO_2 would accumulate beneath the Lea Park shale throughout the entire field)

l = 100 m (an appropriate, representative thickness for the Lea Park shale in the Weyburn field, but a conservative assumption considering that the entire thickness of the Colorado Aquitard is several hundred metres)

$$Q = 3.5 \cdot 10^{6}\ Pa \cdot \frac{2 \cdot 10^{-20} m^2}{6.14 \cdot 10^{-5} Pa \cdot s} \cdot \frac{1.7 \cdot 10^{8} m^2}{100 m}$$

$$Q = 9.6 \cdot 10^{-4} \frac{m^3}{s}$$

or converting to Mt $year^{-1}$, using a representative in-situ density of CO_2 of 200 kg m^{-3}:

$$Q = 1.4 \cdot 10^{-4} \frac{m^3}{s} \cdot 200 \frac{kg}{m^3} \cdot 10^{-9} \frac{Mt}{kg} \cdot 3.16 \cdot 10^{7} \frac{s}{y}$$

$$Q = 0.0009 \frac{Mt}{y}$$

The IEA GHG Programme projects that the Weyburn site will be able to store 30 Mt over the approximately 25 year lifespan of the project (Preston et al. 2005). Comparing this with steady-state flow, a leakage rate of approximately 0.0009 Mt/year represents a loss of approximately 0.003% per year (or 3% over 1000 years) of the stored CO_2. This is a noteworthy number, though it must be recalled that it was calculated based on a number of conservative assumptions; not the least of which is steady-state flow.

7. CONCLUSIONS AND RECOMMENDATIONS

7.1 Conclusions

Shale samples from the Lea Park Formation were studied to assess this formation's effectiveness as a secondary containment barrier to CO_2 in the vicinity of the Weyburn Field, southeast Saskatchewan. Shales from the Colorado Group, obtained from a site near Rocanville Saskatchewan, were also analyzed. The latter samples were relevant to this research because the Lea Park Formation and Colorado Group are both members of the same regional aquitard, referred to as the Colorado Aquitard. The following conclusions can be made:

- The permeabilities of the Lea Park and Colorado shale samples measured in this research ranged from 14 to 45 nd.
- The CO_2 breakthrough pressure of one Lea Park shale sample was determined to be 0.02 MPa. Breakthrough pressures of 0.02 and 2.7 MPa were measured on Colorado shale samples, the latter (higher) value being measured on a sample with a high calcite content.
- The CO_2 breakthrough pressures that were determined during this thesis work are small. However, the permeabilities are also extremely small. Therefore, the permeability is going to play a more significant role in controlling the amount of CO_2 that will potentially leak through the Lea Park Shale.
- Calculations suggest that it would take tens of thousands of years for CO_2 to migrate upwards through a 100 m thickness of Lea Park shale matrix.
- Data currently available for the Lea Park Formation provides no evidence of pervasive natural fracturing in the vicinity of the Weyburn Field.

- The testing system developed in this research provides a suitable means of measuring permeabilities and breakthrough pressures of tight rocks, such as shale; however, the system is extremely sensitive to small leaks and temperature fluctuations, and sample preparation is extremely difficult for weak, fissile materials like shale.

7.2 Recommendations

The following recommendations are made:

- Further study into the effects of sample desiccation from mercury porosimetry testing should be conducted prior to using this method to determine CO_2 breakthrough pressures.
- When conducting pressure-pulse decay permeability tests and CO_2 breakthrough pressure tests, every effort should be made to control the ambient temperature and to reduce temperature fluctuations.
- A jacketing material that does not interact with CO_2 should be used when conducting long-term CO_2 breakthrough pressure experiments. Prior to running experiments, tests should be conducted on various jacketing materials to see if any interactions occur.
- Ideally, syringe pumps with tighter seals and more sensitive control of pressure and flow rates should be used to control the pressure pulses and CO_2 injection.

REFERENCES

AL-Bazali, T.M., Zhang, J., Chenevert, M.E., Sharma, M.M. 2005. Measurement of the sealing capacity of shale caprocks. SPE Paper 96100: 1-13.

ASTM D4404-84, 2004. Standard Test Method for Determination of Pore Volume and Pore Volume Distribution of Soil and Rock by Mercury Injection Porosimetry.

Bachu, S., Stewart, S. 2002. Geological sequestration of anthropogenic carbon dioxide in the western Canada sedimentary basin: suitability analysis. Journal of Canadian Petroleum Technology, **41(2):** 32-40.

Bear, J. 1972. Dynamics of Fluids in Porous Media. Dover Publications, New York.

Bell, J.S., Price, P.R., McLellan, P.J. 1994. In-situ stress in the Western Canada Sedimentary Basin. In Geological Atlas of the Western Canada Sedimentary Basin, comp. G.D. Mossop and I. Shetsen, Canadian Society of Petroleum Geologists and Alberta Research Council, Calgary, Canada, 439-446.

Bennion, D.B., Bachu, S. 2007. Permeability and relative permeability measurements at reservoir conditions for CO_2-water systems in ultra-low permeability confining caprocks. SPE Paper 106995: 1-9.

Benson, S., Cook, P. 2005. Carbon Dioxide Capture and Storage. Cambridge University Press, Cambridge, UK.

Bossie-Coudreanu, D. 2008. The CO_2 – EOR sequestration equation: Recovery, dynamic monitoring, and co-optimization. First Break, **26(1):** 73-83.

Brace, W.F., Walsh, J.B., Frangos, W.T. 1968. Permeability of granite under high pressure. Journal of Geophysical Research, **73(6):** 2225-2236.

Bredehoeft, J.D., Neuzil, C.E., Milly, P.C.D. 1983. Regional Flow in the Dakota Aquifer: A study of the role of confining layers. US Geological Survey Water Supply Paper 2237, pp. 1-45.

Busch, A., Alles, S., Gensterblum, Y., Prinz, D., Dewhurst, D.N., Raven, M., Stanjek, H., Krooss, B.M. 2008. Carbon dioxide storage potential of shales. International Journal of Greenhouse Gas Control, **2:** 297-308.

Chalbaud, C., Robin, M., Lombard, J-M, Martin, F., Egermann, P., Bertin, H. 2009. Interfacial tension measurements and wettability evaluation for geological CO_2 storage. Advances in Water Resources, **32:** 98-109.

Chan, T.K. (2005). Unpublished data. University of Saskatchewan.

Chan, T.K., Hawkes, C.D. 2005. Petrophysical and geotechnical properties of Lea Park Formation shale from Weyburn, Saskatchewan. Proceedings of the 58th Canadian Geotechnical Conference & 6th Joint CGS & IAH-CNC Groundwater Specialty Conference, Saskatoon, Canada, September 18-23, 2005, 8 p.

Christopher, J.E., Yurkowski, M. 2003. A major late Cretaceous (Campanian) unconformity, Southeastern Saskatchewan. Saskatchewan Geological Survey Summary of Investigations, **1:** 1-7.

Chiquet, P., Broseta, D., Thibeau, S. 2007. Wettability alteration of caprock minerals by carbon dioxide. Geofluids, **7:** 112-122.

Chiquet, P., Daridon, J.L., Broseta, D., Thibeau, S. 2007. CO_2/water interfacial tensions under pressure and temperature conditions of CO_2 geological storage. Energy Conversion Management, **48:** 736-744.

Chun, B.S., Wilkinson, G.T. 1995. Interfacial tension in high-pressure carbon dioxide mixtures. Industrial Engineering Chemistry Resources, **34:** 4371-4377.

Craig, R.F. (7^{th} ed.) 2004. Craig's Soil Mechanics. Spoon Press, New York.

Crank, J. 1975. The Mathematics of Diffusion. Clarendon Press, Oxford.

Day, R.W. 1999. Geotechnical and Foundation Engineering: Design and Construction. McGraw-Hill, New York, New York.

Dicker, A.I., Smits, R.M. 1988. A practical approach for determining permeability from laboratory pressure-pulse decay measurements. SPE Paper 17578: 285-292.

Diller, D.E., Ball, M.J. 1985. Shear viscosity coefficients of compressed gaseous and liquid carbon dioxide at temperatures between 220 and 320 K and at pressures to 30 MPa. International Journal of Thermophysics, **6(6):** 619-629.

Dones, R., Bauer, C., Heck, T., Mayer-Spohn, O., Blesl, M. 2008. Life cycle assessment of future fossil technologies with and without carbon capture and storage. Material Research Society Symposium, **1014:** 147-158.

Ennis-King, J., Paterson, L. 2002. Engineering aspects of geological sequestration of carbon dioxide. SPE Paper 77809: 1-13.

Espie, A.A. 2005. CO_2 capture and storage: contributing to sustainable world growth. International Petroleum Technology Conference Paper 10936: 1-7.

Fetter, C.W. 1994. Applied Hydrogeology. 3rd Edition. Prentice Hall, NJ.

Fine, R.A., Millero, F.J. 1973. Compressibility of water as a function of temperature and pressure. The Journal of Chemical Physics, **59(10):** 5529-5536.

Flin, D. 2004. Can sequestration help industry beat pollution? IEE Power Engineer, October/November, 25-28.

GR Petrology Consultants Inc. 2009. Petrographic and Reservoir Quality Assessment Colorado Shale and Lea Park Shale Two Core Samples. GR Report 14056 09.

Grimes, C.E., Kestin, J., Khalifa, H.E. 1979. Viscosity of aqueous KCl solutions in the temperature range 25 – 150 °C and the pressure range 0 – 30 MPa. Journal of Chemical and Engineering Data, **24(2):** 121-126.

Gunter, W.D., Bachu, S., Benson, S. 2004. The role of hydrogeological and geochemical trapping in sedimentary basins for secure geological storage of carbon dioxide. From Geological

Storage of Carbon Dioxide. Geological Society, London, Special Publications, 233: 129-145. Editors: Baines, S.J., Worden, R.H.

Haskett, S.E., Narahara, G.M., Holditch, S.A. 1988. A method for simultaneous determination of permeability and porosity in low-permeability cores. SPE Formation Evaluation September 1988, 651-658.

Hepple, R.P., Benson, S.M. 2005. Geologic storage of carbon dioxide as a climate change mitigation strategy: performance requirements and the implications of surface seepage. Environmental Geology, **47:** 576-585.

Hildenbrand, A., Schlomer, S., Krooss, B.M. 2002. Gas breakthrough experiments on fine-grained sedimentary rocks. Geofluids, **2:** 3-23.

Hildenbrand, A., Schlomer, S., Krooss, B.M., Little, R. 2004. Gas breakthrough experiments on pelitic rocks: comparative study with N_2, CO_2, and CH_4. Geofluids, **4:** 61-80.

Holloway, S. 2001. Storage of fossil fuel-derived carbon dioxide beneath the surface of the Earth. Annual Review of Energy and the Environment, **26:** 145-166.

Horsrud, P., Snsteb O, E.F., Be, R. 1998. Mechanical and petrophysical properties of North Sea shales. International Journal of Rock Mechanics and Mining Sciences, **35(8):** 1009-1020.

Jones, S.C. 1997. A technique for faster pulse-decay permeability measurements in tight rocks. SPE Formation Evaluation March 1997, 19-25.

Katsube, T.J., Mudford, B.S., Best, M.E. 1991. Petrophysical characteristics of shales from the Scotian shelf. Geophysics, **56(10):** 1681-1689.

Katsube, T.J., Issler, D.R., Cox, W.C. 1998. Shale permeability and its relation to pore-size distribution. From Current Research 1998-D, Geological Survey of Canada, 51-57.

Katsube, T.J., Issler, D.R., Coyner, K. 1996. Petrophysical characteristics of shale from the Beaufort-Mackenzie Basin, northern Canada: permeability, formation factor, and porosity versus pressure. From Current Research 1996-B, Geological Survey of Canada, 45-50.

Kumpel, H.J. 1991. Poroelasticity: parameters reviewed. Geophysical Journal International, **105(3):** 783-799.

Li, S., Dong, M., Li, Z., Huang, S., Qing, H., Nickel, E. 2005a. Gas breakthrough pressure for hydrocarbon reservoir seal rocks: implications for the security of long-term CO_2 storage in the Weyburn field. Geofluids, **5:** 326-334.

Li, Z., Dong, M., Li, S., Huang, S. 2005b. CO_2 sequestration in depleted oil and gas reservoirs – caprock characterization and storage capacity. Energy Conversion and Management, **47:** 1372-1382.

Meijer Drees, N.C., Myhr, D.W. 1981. The Upper Cretaceous Milk River and Lea Park Formations in Southeastern Alberta. Bulletin of Canadian Petroleum Geology, **29(1):** 42-74.

Neuzil, C.E. 1980. Measurement of in-situ hydraulic conductivity in the Cretaceous Pierre Shale. 3rd Invitational Well-Testing Symposium: Well-Testing in Low Permeability Environments, March 26-28, 96-102.

Neuzil, C.E., Bredehoeft, J.D., Wolff, R.G. 1984. Leakage and fracture permeability in Cretaceous shales confining the Dakota aquifer in South Dakota. From Proceedings of the First C.V. Theis Conference on Geohydrogeology, pp. 113-120.

Nichols Jr, T.C., Collins, D.S., Jones-Cecil, M., Swolfs, H.S. 1994. Faults and structure in the Pierre shale, central South Dakota. Perspectives on the eastern margin of the Cretaceous Western Interior Basin, p. 211-235.

Ostrowski, L., Ulker, B. 2008. Minimizing risk of gas escape in gas storage by in-situ measurement of gas threshold pressure and optimized completion solutions. SPE Paper 113509.

Palciauskas, V.V., Domenico, P.A. 1989. Fluid pressures in deforming porous rocks. Water Resources Research, **25(2):** 203-213.

Pipkin, B.W., Trent, D.D. (2nd ed.) 1997. Geology and the Environment. Wadsworth Publishing Company, Belmont, California.

Preston, C., Monea, M., Jazrawi, W., Brown, K., Whittaker, S., White, D., Law, D., Chalaturnyk, R., Rostron, B. 2005. IEA GHG Weyburn CO_2 monitoring and storage project. Fuel Processing Technology, **86:** 1547-1568.

Reeves, M. 2003. GeoE 475 Advanced Hydrogeology Class Notes.

Ren, Q.Y., Chen, G.J., Yan, W., Guo, T.M. 2000. Interfacial tension of (CO_2 + CH_4) + water from 298 K to 373 K and pressures up to 30 MPa. Journal of Chemical Engineering Data, **45**: 610-612.

Shipton, Z.K., Evans, J.P., Kirschner, D., Kolesar, P.T., Williams, A.P., Heath, J.E. 2004. Analysis of CO_2 leakage through "low-permeability" faults from natural reservoirs in the

Colorado Plateau, east-central Utah. Geological Society of London, Special Publications, **233**: 43-58.

Soltanzadeh, H., Hawkes, C.D. 2008. Semi-analytical models for stress change and fault reactivation induced by reservoir production and injection, Journal of Petroleum Science and Engineering, **60(2)**: 71-85.

Supercritical Fluid Technologies. 2010. TN-32 - Compression and Condensation of CO_2, http://www.supercriticalfluids.com/publications/TN-32%20-%20Compression%20and %20Condensation%20of%20CO2.pdf, Accessed December 2010.

Thibeau, S., Nghiem, L.X., Ohkuma, H. 2007. A modeling study of the role of selected minerals in enhancing CO_2 mineralization during CO_2 aquifer storage. SPE Paper 109739: 1-17.

Thompson, A.H., Katz, A.J., Krohn, C.E. 1987. The microgeometry and transport properties of sedimentary rock. Advances in Physics, **36:** 625-694.

Trimmer, D.A. 1981. Design criteria for laboratory measurements of low permeability rocks. Geophysical Research Letters, **8(9):** 973-975.

Wells, A.W., Diehl, J.R., Bromhal, G., Strazisara, B.R., Wilson, T.H., White, C.M. 2007. The use of tracers to assess leakage from the sequestration of CO_2 in a depleted oil reservoir, New Mexico, USA, Applied Geochemistry, **22(5)**: 996-1016.

White, D.J., Burrowes, G., Davis, T., Hajnal, Z., Hirsche, K., Hutcheon, I., Majer, E., Rostron, B., Whittaker, S. 2004. Greenhouse gas sequestration in abandoned oil reservoirs: The International Energy Agency Weyburn pilot project. GSA Today, **14(7):** 4-10.

Wilson, M., Monea, M. 2004. IEA GHG Weyburn CO_2 Monitoring and Storage Project Summary Report 2000-2004. Proceedings of the 7th International Conference on Greenhouse Gas Control Technologies, p. 28.

www. http://www.supercriticalfluids.com/publications/TN-32%20- %20Compression%20and%20Condensation%20of%20CO2.pdf. Accessed 10 December 2010.

Yale, D.P., Jamieson, W.H. 1994. Static and dynamic rock mechanical properties in the Hugoton and Panoma Fields, Kansas. SPE Paper 27939.

Zweigel, P., Lindeberg, E., Moen, A., Wessel-Berg, D. 2005. Towards a methodology for top seal efficacy assessment for underground CO_2 storage. Greenhouse Gas Control Technologies, **2:** 1323-1328.

APPENDIX A

TEST PROCEDURES

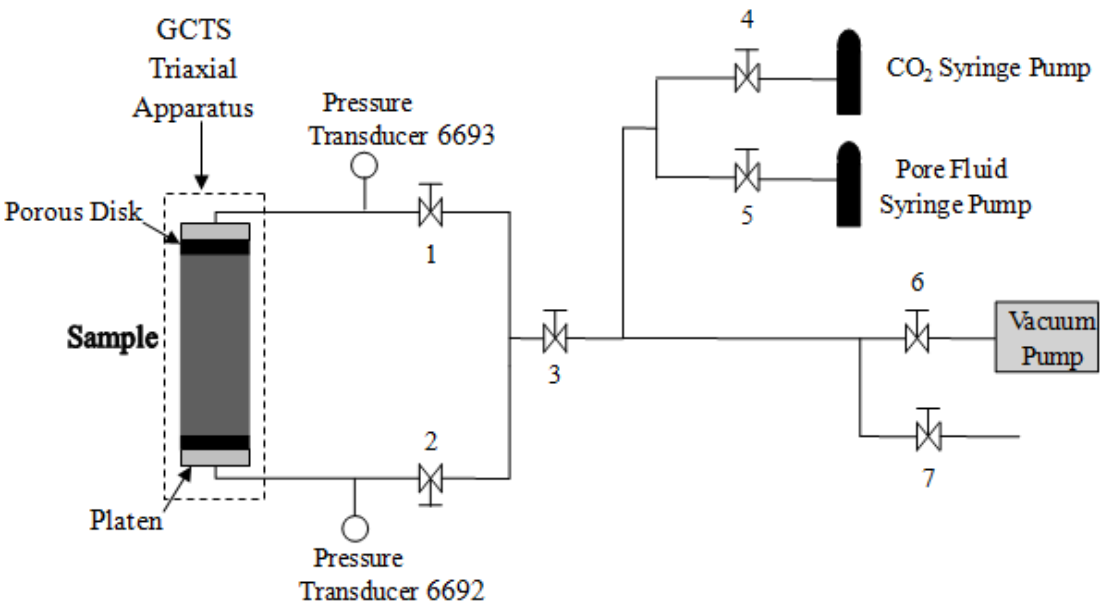

Preliminary Steps

1. Prepare the mold by spreading vacuum grease on the insides. Make sure that grease is as even as possible (do not leave clumps as this can lead to holes or thin spots in the Skin Flex).
2. Cut sample. Measure the length and diameter. Weigh sample.
3. Place sample between platens and porous plates.
4. Carefully secure mold around sample ensuring that no vacuum grease gets on the sample. If this happens, the Skin Flex will not stick to the sample.
5. Prepare the Skin Flex:
    a. Measure one part of Skin Flex A to two parts of Skin Flex B.
    b. Mix well for several minutes. Inadequate mixing will not allow the Skin Flex to set properly.
    c. Place the mixed Skin Flex in a vacuum chamber to remove air bubbles.
    d. Pour into the mold.
    e. Let set overnight or for approximately 24 hours.
6. Place the sample into the triaxial.
7. Lower the cell cover and fill the cell with oil.
8. Using the GCTS pressure cabinet, apply a small confining pressure to bring the piston into contact with the axial load piston.

9. Once a small confining pressure has been applied, open valves 1, 2, and 3. Close valves 4, 5, and 7. Open valve 6 and turn on the vacuum pump. Apply a vacuum to the system for approximately 15 minutes in order to remove any air bubbles that may be in the tubing. Close valve 6 and turn off the vacuum pump.
10. Once hydrostatic pressure has been established, use the syringe pump to continue applying confining pressure. Apply the confining pressure in reasonably small increments so that the sample does not break. Continue this until the desired confining pressure is reached.
11. Prior to doing any testing, the sample must consolidate and the pore pressures must be in equilibrium. (It may be necessary to initially inject some synthetic pore fluid at a low pressure into the tubing after the vacuum has been applied.)
    a. During initial consolidation, valves 1 and 2 can be open but valve 3 must be closed. The other valves can either be open or closed.
    b. Once the consolidation is slowing down, valves 1 and 2 should be closed. This will create a small pressure pulse on whichever side is closed first (try to close the valves at the same time if possible). It will also cause the pressures to increase. Valves 1 and 2 can be slowly closed over several days to reduce this pressure increase.
    c. Bleed off excess pore pressure as required using valve 7.

Permeability Testing

1. Initially, valves 1 and 2 are closed. Close valves 4, 6, and 7, and open valves 3 and 5.
2. Apply a pressure pulse using the pore fluid syringe pump. Open valve 1 long enough to allow the pressure pulse to pass by pressure transducer 6693, then close valve 1 (it should only be open for a few seconds).
3. Valves 1 and 2 remain closed throughout the test.
4. Monitor the pressure responses in both pressure transducers using the digital outputs in the GCTS CATS software.
5. Allow the pressures to re-equilibrate prior to running additional tests, and repeat steps 1 through 4.

CO_2 Breakthrough Pressure Testing

1. Prior to starting the CO_2 breakthrough pressure (BTP) testing, the contents of the tubing between valve 4 and the end of the sample must be emptied.
    a. Keep valve 2 closed. Open valve 1 and valve 7 and allow the contents to drain.
    b. Close valve 7 and apply the vacuum pump to the tubing, keeping valve 2 closed.
2. Inject some CO_2 into the tubing at a pressure similar to that on the downstream end of the sample.
3. Wait until the pressure transducers are giving somewhat similar readings.
4. Valves 1 and 4 are still open at this point.
5. CO_2 BTP Testing using Small Incremental Pressure Increases
    a. Apply a small pressure increase to the upstream end of the sample (through valve 1) using the CO_2 syringe pump set to Constant Pressure Mode. Valves 1 and 4 remain open.
    b. Once it is clear that breakthrough has not occurred, apply another small pressure increment.
    c. Continue to apply these small pressure increments until the CO_2 syringe pump can no longer maintain a constant pressure. This indicates that breakthrough has occurred.
6. CO_2 BTP Testing using Instantaneously High Pressure Gradient
    a. Apply an instantaneously high pressure pulse using the CO_2 syringe pump. Valves 1 and 4 remain open.
    b. Monitor the pressure changes in both the upstream and downstream ends of the sample.